STUDIES ON VARIOUS MORPHOLOGIES OF ZINC OXIDE NANOSTRUCTURES GROWN VIA PULSED LASER DEPOSITION

by

POULAMI GHOSH

Department of Physics

Indian Institute of Technology Guwahati

Guwahati-781039, India

July 2014

STUDIES ON VARIOUS MORPHOLOGIES OF ZINC OXIDE NANOSTRUCTURES GROWN VIA PULSED LASER DEPOSITION

A Thesis submitted in partial fulfillment of the requirements for the award of the degree of

DOCTOR OF PHILOSOPHY

by

POULAMI GHOSH

DEPARTMENT OF PHYSICS

INDIAN INSTITUTE OF TECHNOLOGY GUWAHATI

GUWAHATI-781039, INDIA

JULY 2014

In memory of my Grandmother

Dedicated to my Parents

Poulami Ghosh
Roll No. 09612110
Department of Physics
Indian Institute of Technology Guwahati
Guwahati-781039, Assam, India

STATEMENT

I hereby declare that the matter embodied in this thesis is the result of investigations carried out by me at the Department of Physics, Indian Institute of Technology Guwahati, Guwahati, India, under the supervision of **Dr. Ashwini Kumar Sharma**. This thesis has not been submitted to any university/institute or elsewhere for the award of any degree, diploma or associate ship.

Date: Poulami Ghosh

Dr. Ashwini Kumar Sharma
Assistant Professor
Department of Physics
Indian Institute of Technology Guwahati
Guwahati-781039, Assam, India
Tel – 0361 2582724, Fax – 0361 2582749

CERTIFICATE

This is to certify that work contained in the thesis entitled '**Studies on various morphologies of zinc oxide nanostructures grown via pulsed laser deposition**', by **Poulami Ghosh** (Roll no. 09612110), a student of Department of Physics, Indian Institute of Technology Guwahati, Guwahati, India, for the award of degree of Doctor of Philosophy, has been carried out under my supervision and that the same has not been submitted elsewhere for a degree.

Date: Ashwini Kumar Sharma

Acknowledgements

It gives me immense pleasure to acknowledge the persons without whose help it would not been possible for me to wind up the thesis in presentable form.

First and foremost, I wish to thank my thesis supervisor Dr. Ashwini Kumar Sharma for his guidance, help and suggestions. I thank him for motivating me and spending time for useful discussions. His sincere efforts are also appreciated. He gave me full freedom to do work in my way. It's a nice experience for me to work with him. I have learnt a lot from him.

I am also thankful to Prof. Saurabh Basu for his sincere help, suggestions, support and raising my confidence during my stay in IIT Guwahati. Whenever I felt depressed, he had managed time from his busy schedule to motivate and encourage me. His friendly behavior made me feel free to discuss my problems with him.

I am thankful to my Doctoral committee members Prof. Alika Khare, Prof. Saurabh Basu, Dr. G. Krishnamoorthy, and Dr. Dipak Kumar Goswami for reviewing of my work time to time. Their useful suggestions helped me to improve the work.

I am thankful to my CSIR review committee members, Prof. S. Ravi, Prof. S. Basu and Prof. Anurup Gohain Barua for their valuable suggestions.

I am thankful to CSIR, New Delhi for providing me financial assistance.

I wish to thank all the faculty members and staffs in the department for their help whenever I needed. Also, I wish to thank CIF, IIT Guwahati for providing Raman, FE-SEM and AFM facilities. I am thankful to Mr. Kaustabh Acharya and Miss. Pranjoli Das for their help in XRD measurements in Centre for Nanotechnology.

My thank goes to the present and past research group of my lab for their help.

I am thankful to my friends as well as hostelmates Debarchana, Barnali, Manirupa di, Deepanjali, shyni, Deepanwita, Trivedi and Chandani for sharing both my joy and sorrow with them.

My sincere thank extends to my batchmates, seniors and juniors, specially Abu da, Partha, Swarnadeep, Ramesh, Tapas, Mahesh, Biswajit Pathak for their help.

Some of the persons are not related directly to thesis, but their help, suggestions and encouragements were valuable for me. I wish to thank Debashis Bhattacharyaa Sir, Dr. Sanjoy Mukherjee, and Dr. Partha Mitra for their suggestions and motivating words.

I am thankful to my sister Tanaya and brother in law Tapas for their love and support. I am also thankful to my niece Tanvi whose smiling face was a relaxation for me.

I am very much thankful to my grandmother, parents for their love, care, support and faith on me.

Abstract

In this thesis, zinc oxide nanostructures with various morphologies namely, diamond-shaped, nanorods/wires, combination of nanorods and nanowires, flower-shaped, pores surrounded by craters grown by pulsed laser deposition are reported. These structures were grown by varying three deposition parameters: substrate temperature, oxygen pressure and deposition time. The structural, morphological and optical properties of the nanostructures were studied by x-ray diffraction, field-emission scanning electron microscopy, atomic force microscopy, photoluminescence and Micro-Raman spectroscopy. Prominent diamond-shaped structures were observed at a substrate temperature of 450^0C, deposition time of 20 minutes and oxygen pressure of 0.1 mbar. The formation is discussed in the light of growth rates of various planes of the zinc oxide. Attempt is also made to look at the formation in terms of crystal growth habit models. These structures showed intense photoluminescence due to multiple reflection of light from the end facets. Nanorods/wires and the combination of nanorods and nanowires were obtained by changing the deposition time to 60 minutes. The growth of these combinations is attributed to the formation of different size of background particles. Keeping deposition time fixed at 60 minutes and changing oxygen gas pressure to 0.05 mbar resulted in the formation of flower-shaped nanostructures. The formation is due to the agglomeration of the particles. To see the effect of gas pressure, substrate temperature was fixed at 600^0C and deposition was carried out at three different oxygen pressures of 0.01, 0.03 and 0.05 mbar for 45 minutes deposition time. In this range morphological evolution from pores surrounded by craters to particles was observed. In order to understand the pores formation, oxygen pressure was fixed at 0.03 mbar and depositions were carried out for 5, 15, 30, 45 and 60 minutes. The mechanism is proposed in the light of Stranski-Krastanov growth model. Some of these nanostructures had less defects and stress and strain. Two-photon induced photoluminescence studies were carried out on some of these nanostructures by using continuous wave He-Ne laser at 632 nm as the excitation source. Two-photon induced photoluminescence emissions were observed with modulations. These modulations are quantified as the laser emission attributed to the formation of whispering gallery modes.

Contents

List of Figures

List of Tables

Abbreviations

AFM	Atomic Force Microscope
arb. units	Arbitrary Unit
ASPL	Anti-Stoke's Photoluminescence
ATCC	Automated Target Control carrousel
CW	Continuous wave
FE-SEM	Field Emission Scanning Electron Microscope
FP	Fabry-Perot
FWHM	Full Width at Half Maximum
GaN	Gallium Nitride
He-Ne	Helium Neon
HF	Hydroflouric Acid
IB	Inverse-Bremsstrahlung
Nd:YAG	Neodymium Yttrium Aluminum Garnet
PI	Photoionization
PLD	Pulsed Laser Deposition
PL	Photoluminescence
RMS	Root Mean Square
RT	Room Temperature
TPA	Two Photon Absorption
TS-TPA	Two-step Two Photon Absorption
UV	Ultra Violet
WGM	Whispering Gallery Mode
XRD	X-ray Diffraction

List of Symbols

a	Lattice parameter of ZnO
c	Lattice parameter of ZnO
C_v	Specific heat
d	Interplaner/lattice spacing of ZnO nanostructures
d_0	Lattice spacing of bulk ZnO
D	Grain size
D_{th}	Thermal diffusivity
e	Charge of electron
E_p	Photon energy
E_{gap}	Band-gap energy
h	Planck constant
I	Intensity of laser
K	Thermal conductivity
K_B	Boltzman constant
l	Mean free path
L	Cavity length
L_{th}	Thermal diffusion length
m_e	Mass of electron
n	Number of photons
n_c	Critical density of plasma
n_i	Density of ionized species
n_n	Density of neutral species
N_n	Number density
P_o	Oxygen pressure
P	Excitation power of laser
Q	Q-factor

R	Reflectivity
T, T_e	Plasma temperature
U_n	Ionization energy of plasma
X	Dimension perpendicular to target surface
$\overline{Z}$	Average charge
(hkl)	Miller indices
α	Absorption coefficient
β	FWHM of XRD peak
θ	Angle of reflection of X-ray
η	Refractive index
ρ	Target density
τ	Laser pulse duration
υ_L	Frequency of laser light
λ_x	Wavelength of x-ray
λ	Laser wavelength
ω	Laser frequency
ΔH_v	Vaporization energy
$\delta\lambda$	Mode spacing

Chapter 1

Introduction

Zinc oxide (ZnO) is a semiconducting material that has gained tremendous interest because of its applications in cosmetics and industries. As reported by Klingshirn, production of ZnO is 100,000 tons per year and large amount of it is used as an important ingredient in rubber and cement industries [1]. ZnO is applicable in these industries because of its properties like heat conductivity and chemical activity. In rubber factory, one of the applications is making tyres using ZnO as an additive. Mixing ZnO with rubber improves its durability and increase the heat dissipation from the rubber when rolling on the street. In cement factory, addition of ZnO increases the processing time and also improves the long term strength gain [1, 2]. It is also an important ingredient in medicines and cosmetics and is useful as UV-blocker in sunscreen lotion and as additive in food etc [1, 3]. It acts as a food additive as it is an important ingredient for nutrition and useful as antibiotic [3].

ZnO is not a new material as research on ZnO has been carried out from year 1935 or even earlier. Studies on lattice constants of ZnO were reported in the literature by Bunn in 1935 [4], Heller et al. in 1950 [5], infrared reflectivity for the determination of effective charge per ion site, carrier mass, effective mass by Collins et al. in 1959 [6], lattice vibrations from Raman effect by Damen et al in 1966 [7], exciton spectrum of ZnO by Thomas in 1960 [8] etc.

As a semiconductor it has gained importance because of its properties like wide band-gap (~ 3.37 eV at room temperature (RT)) and high excitonic binding energy (~ 60 meV at RT) [9]. GaN is also a wide band gap semiconductor and it has applications in

optoelectronics but ZnO has some advantages over GaN. Excitonic binding energy of ZnO is around 60 meV whereas it is 25 meV for GaN [10], much higher which ensures efficient excitonic emission at RT. ZnO has high radiation damage threshold and available in large area substrates as compared to GaN [11]. By distorting the central symmetry of tetrahedral ZnO, piezoelectricity and pyroelectricity can be introduced in the lattice structures. Because of the combination of several functional properties including semiconducting, piezoelectric, optical, mechanical and optoelectronic properties, ZnO has wide range of applications such as in sensors [12 - 14], lasers [15 - 18], luminescent devices in UV and visible region [18, 19] light emitting diodes [20], field effect transistors [21], piezoelectric sensors and actuators [22], Schottky UV photodetectors [23], nonlinear absorption based devices [24] etc.

Nanostructured materials have gained huge attention as compared to bulk materials due to both the surface and quantum effects. Surface effect arises due to the adsorption on the surface which causes depletion region and band bending near surfaces and this affects the photoluminescence (PL) property [25]. Quantum effect arises when the size of the material is of the order of few nm. This results in the blue shifting in PL emission [26]. These factors affect various properties such as optical, chemical, mechanical, magnetic etc. The essence is to miniaturization the devices so that they can be used in harsh environments and remote locations.

Surface property of ZnO nanostructure controls the sensitivity as large surface area and high electron mobility allows ZnO nanostructures to adsorb gas or water molecules resulting in change in conductivity [13, 14]. Over the years, interest has grown on the emission in violet region. ZnO powder, nanostructured ZnO acts as scatterer for the formation of laser cavity. Lasing in ZnO has been shown to occur due to formation of whispering gallery mode cavity, random cavity, Fabry-Perot (FP) cavity [15, 17, 18]. Because of wide band gap and the defects due to interstitials, vacancies, antisites and

substantial impurities in the band gap of ZnO gives the photoluminescence in UV-blue and visible region [19]. By doping ZnO with *n*- and *p*-type impurities and making heterostructures, ZnO has been used as LEDs and transistors [20, 21]. By using the piezoelectric property of ZnO, it has been used as piezoelectric sensors and actuators [22, 27]. The production of electron-hole pair occurs in ZnO after illumination of light that results in the change in conductivity. This gives rise to photoconductivity and by using metal schottky contacts, ZnO can be used as photodetector [23, 28]. Because of the presence of second- and third-order nonlinear optical behavior, it is used as nonlinear device [24, 27]. ZnO itself is a *n*-type material. Doping in ZnO by both the acceptor and donor impurity has been done to control the band gap. Doped ZnO based application like LED has also been reported [20, 27, 29-32].

In general, ZnO crystallizes in three phases, cubic zincblende, cubic rocksalt and hexagonl wurtzite. Among these three forms, ZnO is thermodynamically stable in wurtzite form at atmospheric pressure. The wurtzite structure of ZnO is shown in figure 1.1. It has hexagonal lattice that consists of two interplaner hexagonal closed packed structures of zinc (Zn) and oxygen (O) atoms. Zn and O atoms are connected tetrahedrally and forms alternate planes in ZnO stacked along *c*-axis. Being a non-centrosymmetric crystal, the tetrahedral coordination of Zn and O atoms shows piezoelectricity and pyroelectricity [33, 34]. If one atom in a tetrahedron unit can be displaced by inducing some external force, it causes lattice distortion and induces local dipole moment. The local dipole moment from all the units results in macroscopic dipole moment over the crystal giving rise to piezopotential [35].

Another important characteristic of ZnO is its polar surface. The oppositely faced basal planes (0001) and $(000\bar{1})$ are polar surfaces. Though polar surfaces need surface reconstruction, but for ZnO, two polar facets are stable, flat and do not need any reconstruction [36, 37]. Other two facets $(11\bar{2}0)$ and $(10\bar{1}0)$ are non polar and less stable.

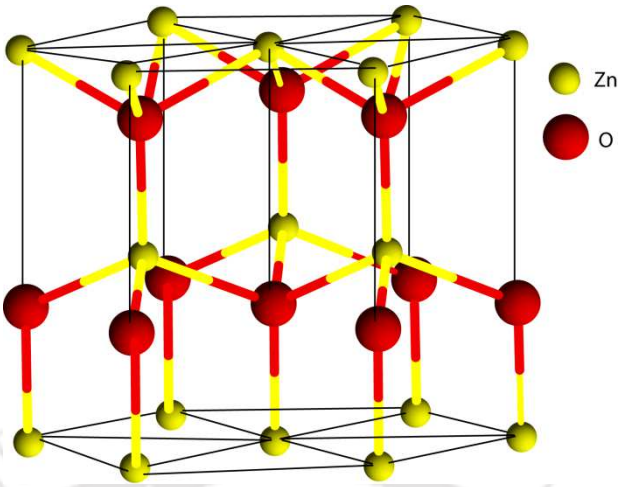

Figure 1.1: Hexagonal wurtzite structure of ZnO.

Being a wurtzite structure, ZnO has lattice parameters (a = 3.2475 to 3.2501 A^0 and c = 5.2042 to 5.2075 A^0) [38] at 300 K. It has a melting point of 2248 K and density 5.606 g/cm^3 [10]. It is a semiconductor of II-VI group having wide band gap of (3.441 ± 0.003 eV) at 0 K and (3.365 ± 0.005 eV) at 300 K [9]. The values of heat conductivity, pyroelectric co-efficient, nonlinear refractive index co-efficient, second- and third-order susceptibilities of ZnO [33] are listed in table 1.1.

ZnO is a very promising optical material because of its wide band gap as well as the high excitonic binding energy [19, 39, 40]. High excitonic binding energy ensures efficient excitonic emissions at RT whereas its wide band gap results luminescence in a wide range (from UV to visible region). The emission in UV and the visible region is due to band-to-band transition and the transitions from defect-related states. Near band-edge emission is reported in the range of 373 – 397 nm [40, 41]. It is also reported that emission in the UV range arises due to the excitonic recombination corresponding to near band-edge emission [42, 43]. Emission in the visible range (405 - 640 nm [40], 400 - 750 nm [44]), called deep level emission arises due to the native defects present in ZnO. These defects are intrinsic

defects in the crystal structure such as interstitial zinc (Zn_i), interstitial oxygen (O_i), zinc vacancy (V_{Zn}), oxygen vacancy (V_O), antisite oxygen (O_{Zn}) [40, 44, 45] etc. The origin of PL peak emissions is discussed in detail by several groups [40, 41, 44 - 46].

Table 1.1: Values of physical parameters of ZnO.

Physical parameters of ZnO	**Values**
Thermal conductivity	0.46 to 1.47 W Cm^{-1} K^{-1}
Pyroelectric coefficient	-9.4 to -10.5 μC m^{-1} K^{-1}
Nonlinear refractive index coefficient	(-0.9 to 0.54)×10^{-14} cm^2 W^{-1}
Second order susceptibility	-14.77 to 4.0 pm V^{-1}
Third order susceptibility	(-0.9 to 22.0)×10^{-12} esu

The electrical [47, 48] and mechanical properties [37, 49] of ZnO have been studied by several researchers. Electrical properties by Hall effect technique [47, 48], mechanical properties by estimating the fracture strain and Young's modulus have been studied and thereby using ZnO as a sensor and actuator [49].

In order to deposit nanostructures, several deposition techniques have been reported. ZnO nanostructures have been grown by different deposition techniques. These are metal organic chemical vapour deposition [50], chemical vapor deposition [51], wet-chemical method [52], solution method [53], hydrothermal method [54], sol-gel method [55], pulsed laser deposition (PLD) [56 - 58] etc. Among all the deposition techniques, PLD is relatively easy and versatile technique. The laser source that creates laser plasma is independent of deposition chamber and hence it offers flexibility in the orientation with respect to the chamber.

PLD is based on the mechanism of laser ablation from solid surface. Laser ablation is a simple and versatile technique [59, 60] in which a wide range of materials can be ablated by focusing a high power laser onto the solid surface. In this process, laser beam interacts with the solid surface, depending on the laser wavelength and the refractive index of the material at that laser wavelength, forms plasma plume that contains electrons, ions, atoms, molecules, particulates and molten globules of that material. The plasma plume interacts with the surroundings and condenses onto the substrate surface which depending upon the experimental conditions forms various types of structures (micro- or nano-) in nature.

PLD has been proposed after the invention of high power ruby laser in 1960's. The first report on laser deposition is by Smith and Turner in 1965 where they used ruby laser to deposit thin films on semiconductors, dielectrics, chalcogenides and organometallic materials [59]. Due to some restrictions on the use of ruby laser, laser deposited thin films were grown by CO_2 laser, Nd:Glass lasers etc. Large number of materials was deposited with the help of PLD at the time [59, 61]. Later on, Q-switched lasers having more peak power came into existence and were then used for PLD for the stochiometric thin film deposition of high temperature superconductors. Since then, PLD has become a useful technique for thin film deposition [59].

Despite several disadvantages like the formation of particulates, molten globules, non-uniform deposition in large surface area, PLD has several advantages for the growth of nanostructures. The main advantage is that it preserves the stoichiometry of the material. High temperature superconductors can also be deposited by PLD whereas thermal evaporation, sputtering techniques fails to maintain the stoichometry of films. The target heating is minimal and local target heating occurs. Also, targets used in this technique are very small. The plasma temperature (i.e. the high energy of the depositing species) is very high (~ 0.1 to 100 eV) depending on the laser fluence and it affects the intrinsic property of

the film. In order to provide extra energy to the substrate surface, external heating arrangement is provided. The deposition of nanostructures can be controlled by various parameters like laser fluence, laser wavelength, target-substrate distance, substrate type, substrate temperature, background gas, background gas pressure etc. Another major advantage is that the same as well as multiple targets can be used for a longer period of time since rastering as well as rotational motion of the target is possible and can be easily controlled. In experimental setup of PLD used in the present work, automated target carrousel controller (ATCC) is used for rastering and rotational motion of the target. The speed of these mechanisms can also be controlled to deposit desired configuration. This therefore adds on to the additional parameters for optimization. Thus, various morphologies or multi-layered structures can be grown without breaking vacuum in the chamber and without changing the target material. Not only the speed of target but the number of laser shots can also be controlled by ATCC thus allowing control over the thickness of the deposited structures. Therefore various parameters associated with PLD are all contained in the single setup and can be used in a single run, something that may not be possible in some of the other available deposition techniques.

Variety of morphologies have been reported by various deposition techniques that includes nanorods [62], microrods [63] nanowires [64], mesostructured micropyramids [65], flower-like structures [54], comb-like structures [66], nanobelts [67], nanorings and disks [68], nanowall-network [69], porous spheres like [70], nanowall network with honeycomb structure [58] etc. Different morphologies of ZnO and their applications are discussed in the literatures such as nanosaws [71], nanowire [72], microrods [15], microtubes [18] in lasing, nanocombs in optical properties and solar cell applications [73, 74], pyramidal structures with enhanced photocatalytic properties [65], nanobelts as field effect transistors [36], porous spheres as gas sensors [70], nanorods as gas sensors [12] etc. ZnO nanoparticles have

tremendous biomedical applications for destruction of tumor cells and for drug delivery applications [75].

Different morphologies of ZnO have been grown by PLD technique. There are several reports on the growth of thin films [76, 77], nanorods [78, 79, 80] and nanowires [56, 72, 81] by PLD. Among other morphologies, pyramidal nanostructures of ZnO by PLD have been reported [82]. In a recent work ZnO nanowall-network with honey-comb structure has also been reported by PLD [58].

ZnO nanostructures have been grown at different laser wavelengths such as ArF excimer laser of 193 nm [78], KrF excimer laser of 248 nm [58, 83], XeCl excimer laser of 308 nm [57], Q-switched Nd:YAG laser of 355 nm [47], 532 nm [84], and 1064 nm [83, 84]. ZnO nanostructures have been grown on various substrates like silicon [79], sapphire [72, 83], GaN [83], Glass [84], FTO [74] etc. ZnO nanostructures have been grown in presence of oxygen [58, 78, 83], argon [72, 81], nitrogen [72] etc. ZnO nanostructures are also reported at a wide range of laser fluence such as 4 J/cm^2 [81], 10 J/cm^2 [78], 0.4 J/cm^2 [84], 8 J/mm^2 [58] etc. Nanostructures grown from RT to very high substrate temperatures in the range of 870 to 1470 K are also reported [72, 78]. ZnO nanostructures are deposited in wide range of target – substrate distance of 1.2 cm to almost 9 cm [58, 78, 81]. ZnO nanostructures have been deposited in a wide range of ambient pressures like 0.003-0.007 mbar [79], 8-17 mTorr [85], 50, 200, 300 and 500 mTorr [47], 150-500 mTorr [56], 5-20 Torr [86], 0.001-10 Torr [76] etc. ZnO nanostructures are also reported at different deposition time durations of 15, 30, 45 minutes [78], 5, 10, 30 and 45 minutes [58] etc. These reported works shows that several deposition parameters can be controlled in a wide range for the growth of nanostructures by PLD technique.

The deposition parameters play an important role on the properties of grown nanostructures. Here, only the effect of substrate temperature, deposition time and oxygen

pressure are discussed briefly. The size of the nanostructures and the morphology get affected by changing the laser wavelength [87]. The morphology of the nanostructures changes completely with the change in substrate and also the size of the nanostructures become different on different substrate surface [88]. As reported in [81], the density of the nanostructures changes with the change in target-substrate distance and laser energy.

The kinetics of atomic arrangement is controlled by the background gas pressures. Kotlyarchuk et al. [76] reported that the mean free path of the particles ablated from plasma plume is related to the oxygen pressure by $l = \frac{10^{-4}}{P}$ m, P is in Torr. So, with the increase in oxygen pressure, mean free path of the ablated particles decreases. If the l value is greater than target-substrate distance, deposition rate is more, if it is less than target-substrate distance, deposition rate is less. Also, with the increase in oxygen pressure, collisions between the ablated particles and the background gas atoms reduce significantly the kinetic energy of the particles. Because of this, low surface mobility of the deposited atoms on the substrate surface leads to the growth of many nuclei. These nuclei coalesce together to form large size grains. Because of the long mean free path of the particles at low pressure, large size particles have the possibility to reach on the substrate surface to make surface rough [89]. The presence of oxygen pressure is necessary to maintain the stochiometry and crystallinity of the thin films. Oxygen pressure has an important role in changing the surface morphology i.e., from micro crystal (hexagonal pyramid-top) to nanorods [76], thin films to nanorods [79], thin film to highly aligned nanowires [56] etc. Ajimsha et al. [79] reported that at 0.003 mbar O_2 pressure small crystallites are formed, at 0.004 mbar, nanorods formation takes place and again at 0.005 mbar, large crystallites are formed. So, a small change in pressure changes morphology a lot. Okada et al. [80] reported that at 0.1 Torr, pyramidal-top microcrystals are formed, at 1 and 5 Torr, nanorods formation occurs and at 10 Torr, nanorods merge together to form flat surfaces. Tien et al. [56] reported that, at 150 mTorr,

smooth thin films are formed, at 300 mTorr, microcrystals with hexagonal facets are formed and at 500 mTorr, highly aligned nanowires are formed.

Substrate temperature plays an important role to maintain the crystallinity and orientation of the nanostructures. Increase in substrate temperature provides an extra energy to the substrate surface that allows the deposited atoms to migrate at the thermodynamically favourable or low energy sites, resulting in the enhancement of crystallinty [56, 79, 85, 75, 90]. Also, at very high substrate temperature, surface of the nanostructures and the crystallinity degrades because the deposited atoms get decomposed and re-evaporates from the substrate surface [90]. It is also reported that the higher substrate temperature may provides energy to neutral zinc which reacts with oxygen and forms ZnO, thereby the ratio of Zn and O becomes 1, forming crystalline film [79]. Liu [90] et al. and Kotlyarchuk [76] et al. reported that the nanostructures grown at room temperature are amorphous whereas with the increase in substrate temperature, nanostructures became crystalline. Tien et al. [56] reported that the diameter of the nanowires decreased from a value of 500 to 100 nm with the increase in substrate temperature from 550^0C to 800^0C. The reduction in diameter of the nanowires was explained in terms of the surface mobility. Zhan et al. [85] has reported that beyond a certain optimum temperature, surface gets random because of secondary nucleation and recrystallization.

The effect of deposition time also plays an important role in changing the surface morphology. Sun et al. [78] reported that at low deposition time, well aligned and uniform nanorods are formed. With the increase in deposition time, nanorods get elongated and forms needle-like morphology. Zein et al. [58] reported the complete structural change of nanostructures with the increase in deposition time. They showed that the nanowall networks with honeycomb-like structures are formed from ZnO nanoparticles with the increase in deposition time.

ZnO nanostructures as well as bulk ZnO gives rise to random lasing due to the formation of Fabry- Perot (FP) cavity [91] or whispering gallery modes (WGM) cavity [15, 92]. Lasing from ZnO nanocombs excited by Q-switched Nd:YAG laser operated at 266 nm [91], nanodiscs excited by Ti:sapphire laser operated at 324 nm [92], nanorods pumped with nitrogen laser radiation at 337.1 nm [93], microtubes excited by femtosecond pulsed laser operated at 800 nm [18], thin films excited by Nd:YAG laser operated at 355 nm [94], nanoneedles excited by Nd:YAG laser operated at 355 nm [95] and bulk ZnO pumped by Q-switched Nd:YAG laser operated at 355 nm [17, 96] has been observed. The shape and size, morphology of ZnO nanostructures play an important role in deciding the lasing threshold [97, 98]. Lasing due to the multi-photon induced absorption has been reported in ZnO nanostructures [18]. Multiphoton induced absorption occurs when the energy corresponding to excitation laser wavelength is less than the half of energy band gap. The PL emission wavelength depends on the excitation wavelength. The number of photons involved in the upconversion mechanism is derived from a simple plot of the slope of the straight line of log (integrated intensity) versus log (peak power) [99]. It is reported that if the excitation laser with photon energy be less than the half the band gap value, emission occurs at 3.15 eV and is due to bound excitons whereas the incident laser energy is greater than the half of band gap, emission occurs due to free excitons at 3.30 eV [100]. Two-photon induced PL is also reported in ZnO with incident laser wavelength in the range of 720-770 nm [101]. Studies have shown that single photon absorption occurs at excitation wavelength of 500 nm, two-photon absorption occurs at excitation wavelength of 730 nm, and three-photon absorption occurs at excitation wavelength of 820 nm, respectively. Absorption due to both one- and two-photon is reported at excitation wavelength of 530 nm, and two- and three-photon absorption at excitation wavelength of 800 nm [102]. PL spectra recorded by N_2 laser at 220 K temperature showing lasing without narrowing of the linewidth above lasing threshold is

reported in the literature [103]. Upconversion of photoluminescence via two-photon absorption by continuous wave (CW) laser is reported in the literature [104]. Effieciency of up-conversion process is higher if the intermediate states involved in two-photon process become real states (i.e. impurity states) rather than virtual states [104]. Anti-stokes PL of ZnO microcrystals by low power CW laser with 532 nm wavelength is also reported [105]. Anti-stokes PL occurs when the photon energy of incident radiation is less than the energy corresponding to emission wavelength. This PL is attributed to two-step two photon absorption (TS-TPA or TPA) and Auger process [105]. As this process requires higher excitation powers, so these PL emissions are considered as nonlinear processes. Two-photon induced PL is reported in ZnO excited by Ti:sapphire laser operated in the range from 714 – 850 nm [106]. The excitation power for PL emission has been as low as 2.3 mW in case of 720.70 nm wavelength [106] and 20 mW excited by nanosecond laser operated at 527 nm [107].

Present work

The present thesis deals with the growth and characterization of pulsed-laser deposited ZnO nanostructures grown in various morphologies: (a) diamond-shaped (refers to the appearance of these structures and not to be confused with the diamond-structure as such which is cubic), (b) combination of nanorods and nanowires on a single substrate, (c) flower-shaped, and (d) pores surrounded by craters. The objective behind the study of each of these structures is to understand the role of deposition parameters viz. substrate temperature, deposition time, and ambient gas pressure. The characterization of optical properties to look for possible application as a light emitting device in the UV range, especially in the diamond-shaped structures is carried out in which the light emitting property is not documented. The nanostructures were analyzed by X-ray diffraction (XRD), field-emission scanning electron

microscopy (FE-SEM), atomic force microscopy (AFM), photoluminescence (PL), and Micro-Raman spectroscopy. Thesis also deals with the two-photon induced PL and lasing of the diamond-shaped nanostructures and combination of nanorods and wires.

The thesis contains eight chapters. The brief descriptions and the contents of the chapters are organized as follows.

Chapter 2 discusses briefly the physical processes and experimental set-up used in the thesis. This includes target preparation, substrate preparation, pulsed laser deposition set-up to grow nanostructures, characterization techniques used to study some properties of grown nanostructures etc. Also, a simple PL set-up using CW-wave He-Ne laser as excitation source is also discussed.

Chapter 3 discusses the effect of substrate temperature (RT to 600^0C) on the structural and optical properties of the grown nanostructures for 20 minutes deposition time at 0.1 mbar O_2 pressure. Since, diamond-shaped nanostructures were observed at 450^0C substrate temperature, so the effect of deposition time is also discussed in order to study the growth mechanism of diamond-shaped nanostructures.

Chapter 4 discusses the effect of substrate temperature (RT – 600^0C) on the structural and optical properties of the combination of nanorods/wires. Nanostructures were deposited at 0.1 mbar O_2 pressure for 60 minutes deposition time.

Chapter 5 discusses the effect of substrate temperature (RT to 750^0C) on the structural and optical properties of the grown flower-shaped nanostructures. Nanostructures were deposited at 0.05 mbar O_2 pressure for 60 minutes deposition time.

Chapter 6 discusses the effect of the oxygen pressure (0.01, 0.03 and 0.05 mbar) on the structural and optical properties of the pores surrounded by craters grown at 600^0C for 45 minutes deposition time. As the crater-like structures were prominent at 0.03 mbar, the effect

of deposition time (5, 15, 30, 45 and 60 minutes) on the formation of crater-like nanostructures is discussed.

Chapter 7 discusses two-photon induced photoluminescence studies on the grown nanostructures. Possible lasing mechanism is also reported.

Chapter 8 Summarizes the results of the thesis and discusses the future scope of the work.

Bibliography

1. C. Klingshirn, Phys. Stat. Sol. (b) 244 (2007) 3027.
2. K. G. Kolovos, S. Barafaka, G. Kakali, S. Tsivilis, Ceramics − Silikáty 49 (2005) 205.
3. J. R. Pluske, Journal of Animal Science and Biotechnology 4 (2013) 7 pages.
4. C. W. Bunn, Proc. Phys. Soc. 47 (1935) 835.
5. R. B. Heller, J. McGannon, A. H. Weber, J. Appl. Phys. 21 (1950) 1283.
6. R. J. Collins, D. A. Kleinman, J. Phys. Chem. Solids. 11 (1959) 190.
7. T. C. Damen, S. P. S. Porto, B. Tell, Phys. Rev. 142 (1966) 570.
8. D. G. Thomas, J. Phys. Chem. Solids. 15 (1960) 86.
9. C. Klingshirn, J. Fallert, H. Zhou, J. Sartor, C. Thiele, F. M-Flaig, D. Schneider, H. Kalt, Physics status solidi b, 247 (2010) 1424.
10. S. J. Pearton, D. P. Norton, K. Ip, Y. W. Heo, T. Steiner, Progress in Materials Science, 50 (2005) 293.
11. Y. S. Choi, J. W. Kang, D. K. Hwang, S. J. Park, IEEE Transactions on Electron Devices, 57 (2010) 26.
12. L. Liao, H. B. Lu, J. C. Li, H. He, D. F. Wang, D. J. Fu, C. Liu, W. F. Zhang, J. Phys. Chem. C, 111 (2007) 1900.
13. A. Wei, L. Pan, W. Huang, Materials Science and Engineering B, 176 (2011) 1409.

14. Qi Qi, T. Zhang, Q. Yu, R. Wang, Y. Zeng, L. Liu, H. Yang, Sensors and Actuators B, 133 (2008) 638.

15. J. Dai, C. X. Xu, K. Zheng, C. G. Lv, Y. P. Cui, Appl. Phys. Lett. 95 (2009) 241110-1.

16. B. Zou, R. Liu, F. Wang, A. Pan, L. Cao, Z. L. Wang, J. Phys. Chem. B, 110 (2006) 12865.

17. R. K. Thareja, A. Mitra, Appl. Phys. B 71 (2000) 181.

18. C. F. Zhang, Z. W. Dong, K. J. Liu, Y. L. Yan, S. X. Qian, H. Deng, Appl. Phys. Lett. 91 (2007) 142109-1.

19. A. B. Djurisic, A. M. C. Ng, X. Y. Chen, Progress in Quantum Electronics. 34 (2010) 191.

20. S. J. Pearton, F. Ren, Current Opinion in Chemical Engineering, 3 (2014) 51.

21. S. N. Cha, J. E. Jang, Y. Choi, G. A. J. Amaratunga, G. W. Ho, M. E. Welland, D. G. Hasko, D. J. Kang, J. M. Kim, Appl. Phys. Lett. 89 (2006) 263102-1.

22. T. Shibata, K. Unno, E. Makino, Y. Ito, S. Shimada, Sensors and Actuators, 102 (2002) 106.

23. S. Liang, H. Sheng, Y.Liu, Z. Huo, Y. Lu, H. Shen, J. Cryst. Growth, 225 (2001) 110.

24. Y. P. Chan, J. H. Lin, C. C. Hsu, W. F. Hsieh, Opt. Exp. 16 (2008) 19900.

25. Z. M. Liao, H. Z. Zhang, Y. B. Zhou, J. Xu, J. M. Zhang, D. P. Yu, Physics Letters A 372 (2008) 4505.

26. Z. D. Fu, Y. S. Cui, S. Y. Zhang, J. Chen, D. P. Yu, S. L. Zhang, L. Niu, J. Z. Ziang, Appl. Phys. Lett. 90 (2007) 263113-1.

27. A. Janotti, Chris G Van de Walle, Rep. Prog. Phys. 72 (2009) 126501.

28. Z. L. Wang, Appl. Phys. A. DOI: 10.1007/s00339-007-3942-8 (2007).

29. Y. R. Ryu, S. Zhu, D. C. Look, J. M. Wrobel, H. M. Jeong, H. W. White, J. Cryst. Growth. 216 (2000) 330.

30. M. K. Yadav, M. Ghosh, R. Biswas, A. K. Raychaudhuri, A. Mookerjee, S. Datta, Phys. Rev. B. 76 (2007) 195450-1.

31. S. Ju, J. Li, N. Pimparkar, M. A. Alam, R. P. H. Chang, D. B. Janes, IEEE Transactions on Nanotechnology, 6 (2007) 390.

32. W. J. Lee, J. Kang, K. J. Chang, J. Kor. Phys. Soc. 53 (2008) 196.

33. H. Morkoc, U. Ozgur, Zinc Oxide, Fundamentals, Materials and Device Technology, WILEY-VCH.

34. C. Jagadish, S. J. Paerton, Zinc Oxide Bulk, Thin Films and Nanostructures, Processing, properties and applications.

35. Z. L. Wang, MRS Bulletin, 37 (2012) 814.

36. Z. L. Wang, J. Phys.: Condens. Mater. 16 (2004) R829.

37. X. Y. Kong, Z. L. Wang, Nano Letters 3 (2003) 1625.

38. U. Ozgur, Y. A. Alivov, C. Liu, A. Teke, M. A. Reshchikov, S. Doan, V. Avrutin, S. J. Cho, H. Morkoc, J. Appl. Phys. 98 (2005) 041301-1.

39. M. Dvorak, S. H. Wei, Z. Wu, Physical Review Letters, 110 (2013) 016402-1.

40. A. B. Djuristic, Y. H. Leung, Small, 2 (2006) 944.

41. C. Y. Chen, M. W. Chen, J. J. Ke, C. A. Lin, J. R. D. Retamal, J. H. He, Pure. Appl. Chem. 82 (2010) 2055.

42. G. Kenanakis, M. Androulidaki, E. Koudoumas, C. Savvakis, N. Katsarakis, Superlattices and Microstructures, 42 (2007) 473.

43. D. Panda, T. Y. Tseng, J. Mater. Sci. 48 (2013) 6849.

44. M. Willander, O. Nur, J. R. Sadaf, M. I. Qadir, S. Zaman, A. Zainelabdin, N. Bano, I. Hussian, Materials, 3 (2010) 2643.

45. S. Vempati, J. Mitra, P. Dawson, Nanoscale Res. Let. 7 (2012) 470.

46. G. Patwari, B. J. Bodo, R. Singha, P. K. Kalita, Research Journal of Chemical Sciences, 3 (2013) 45.

47. B. J. Jin, S. H. Bae, S. Y. Lee, S. Im, Materials Science and Engineering B, 71 (2000) 301.

48. D. C. Look, D. C. Reynolds, J. R. Sizelove, R. L. Zones, C. W. Litton, G. Cantwell, W. C. Harsch, Solid State Commun, 105 (1998) 399.

49. A. V. Desai, M. A. Haque, Sensors and Actuators A, 134 (2007) 169.

50. J. Maeng, G. Jo, M. Choe, W. Park, M. K. Kwon, S. J. Park, T. Lee, Thin Solid Films, 518 (2009) 865.

51. S. W. Kim, S. Fujita, H. K. Park, B. Yang, H. K. Kim, D. H. Yoon, J. Cryst. Growth, 292 (2006) 306.

52. X. Cao, N. Wang, L. Wang, L. Guo, J. Nanopart. Res 12 (2010) 143.

53. L. M. Yu, X. H. Fan, J. Y. Shui, L. Cao, W. Yan, Materials Letters 68 (2012) 423.

54. S. Baruah. J. Dutta, Sci. Technol. Adv. Mater. 10 (2009) 013001.

55. X. Yu, X. Yu, Z. Hu, J. Zhang, G. Zhao, Y. Zhao, Material Letters 108 (2013) 50.

56. L. C. Tien, S. J. Pearton, D. P. Norton, F. Ren, J. Mater. Sci. 43 (2008) 6925.

57. M. Suchea, S. Christoulakis, M. Katharakis, G. Kiriakidis, N. Katsarakis, E. Koudoumas, Appl. Surf. Sci. 253 (2007) 8141.

58. B. El. Zein, S. Boulfrad, G. E. Jabbour, E. Dogheche, Appl. Surf. Sci. 292 (2014) 598.

59. D. B. Chrisey, G. K. Hubler, Pulsed Laser Deposition of Thin Films, John Wiley & Sons, INC. 1994.

60. M. N. R. Ashfold, F. Claeyssens, G. M. Fuge, S. J. Henley, Chem. Soc. Rev. 33 (2004) 23.

61. K. L. Saenger, Processing of Advanced Materials, 2 (1993) 1.

62. F. Xian, W. Bai, L. Xu, X. Wang, X. Li, Material Letters 108 (2013) 46.

63. G. Yang, B. Wang, W. Guo, Q. Wang, Y. Liu, C. Miao, Z. Bu, Material Letters 90 (2013) 34.

64. A. Rahm, M. Lorenz, T. Nobis, G. Zimmermann, M. Grundmann, B. Fuhrmann, F. Syrowatka, Appl. Phys. A 88 (2007) 31.

65. M. Pudukudy, Z. Yakob, Superlattices and Microstructures, 63 (2013) 47.

66. Z. L. Wang, X. Y. Kong, J. M. Zuo, Physical Review Letters 91 (2003) 185502-1.

67. Y. Xi, C. G. Hu, X. Y. Han, Y. F. Xiong, P. X. Gao, G. B. Liu, Solid State Commun. 141 (2007) 506.

68. Y. Peng, A. W. Xu, B. Deng, M. Antonietti, H. Colfen, J. Phys. Chem. B, 110 (2006) 2988.

69. S. W. Kim, H. K. Park, M. S. Yi, N. M. Park, J. H. Park, S. H. Kim, S. L. Maeng, C. J. Choi, S. E. Moon, Appl. Phys. Lett. 90 (2007) 033107-1.

70. X. B. Li, S. Y. Ma, F. M. Li, Y. Chen, Q. Q. Zhang, X. H. Yang, C. Y. Wang, J. Zhu, Material Letters 100 (2013) 119.

71. C. Y. Wu, H. C. Hsu, H. M. Cheng, S. Yang, W. F. Hseih, J. Cryst. Growth 287 (2006) 189.

72. R. Q. Guo, J. Nishimura, M. Matsumoto, D. Nakamura, T. Okada, Appl. Phys. A 93 (2008) 843.

73. T. L. Phan, Y. Sun, R. Vincent, J. Kor. Phys. Soc. 59 (2011) 60.

74. A. Umar, Nanoscale Res. Lett. 4 (2009) 1004.

75. J. W. Rasmussen, E. Martinez P. Louka, D. G. Wingett, Expert Opin. Drug. Deliv. 7 (2010) 1063.

76. B. Kotlyarchuk, V. Savchuk, M. Oszwaldowski, Cryst. Res. Technol. 40 (2005) 1118.

77. J. H. Jo, T. B. Hur, J. S. Kwak, D. Y. Kwon, Y. H. Hwang, H. K. Kim, J. Kor. Phys. Soc. 47 (2005) S300.

78. Y. Sun, G. M. Fuge, M. N. R. Ashfold, Chemical Physics Letters 396 (2004) 21.

79. R. S. Ajimsha, R. Manoj, P. M. Aneesh, M. K. Jayaraj, Current Applied Physics 10 (2010) 693.

80. T. Okada, K. Kawashima, Y. Nakata, X. Ning, Jpn. J. Appl. Phys. 44 (2005) 688.

81. R. Gou, J. Nishimura, M. Matsumoto, M. Higashihata, D. Nakamura, T. Okada, Jpn. J. Appl. Phys. 47 (2008) 741.

82. S. Angappane, N. S. John, G. U. Kulkarni, J. Nanosci. Nanotechnol. 6 (2006) 101.

83. T. Premkumar, P. Manoravi, B. K. Panigrahi, K. Baskar, Appl. Surf. Sci. 255 (2009) 6819.

84. Z. T. Al-dahan, M. A. Abdul Ameer, J. Opt. 42 (2013) 194.

85. P. Zhan, Z. Li, Z. Zhang, Materials Transactions, 52 (2011) 1764.

86. Z. W. Liu, C. K. Ong, T. Yu, Z. X. Shen, Appl. Phys. Lett. 88 (2006) 053110-1.

87. C. McLoughlin, P. Hough, J. Costello, E. McGlynn, J. P. Mosnier, Ultramicroscopy, 109 (2009) 399.

88. M. Roozbehi, P. Sangpour, A. Khademi, A. Z. Moshfegh, Appl. Surf. Sci. 257 (2011) 3291.

89. F. K. Shan, G. X. Liu, B. I. Kim, B. C. Shin, S. C. Kim, Y. S. Yu, J. Kor. Phys. Soc. 42 (2003) s1157.

90. M. Liu, X. Q. Wei, Z. G. Zhang, G. Sun, C. S. Chen, C. S. Xue, H. Z. Zhuang, B. Y. Man, Appl. Surf. Sci, 252 (2006) 4321.

91. Y. Chen. Y. F. Chen, Opt. Exp. 19 (2011) 8728.

92. D. Yu, Y. Chen, B. Li, X. Chen, M. Zhang, F. Zhao, S. Ren, Appl. Phys. Lett. 91 (2007) 091116-1.

93. A. N. Gruzintsev, A. N. Redkin, Z. I. Makovel, E. E. Yakimov, C. Barthou , Semiconductors 41 (2007) 708.

94. Z. K. Tang, G. K. L. Wong, P. Yu, M. Kawasaki, A. Ohtomo, H. Koinuma, Y. Sewaga, Appl. Phys. Lett. 72 (1998) 3270.

95. H. Y. Yang, S. P. Lau, S. F. Yu, A.P. Abiyasa, M. Tanemura, T. Okita, H. Hatano, Appl. Phys. Lett. 89 (2006) 011103-1.

96. X. H. Wu, A. Yamilov, H. Noh, H. Cao, E. W. Seelig, R. P. H. Chang, J. Opt. Soc. Am. B, 21 (2004) 159.

97. A. N. Gruzintsev, G. A. Emelchenko, A. N. Redkin, W. T. Volkov, E. E. Yakimov, G. Visimberga, Semiconductors 44 (2010) 1217.

98. X. Liu, A. Yamilov, X. Wu, J. G. Zheng, H. Cao, R. P. H. Chang, Chem. Mater, 16 (2004) 5414.

99. S. K. Das, M. Biswas, D. Byrne, M. Bock, E. McGlynn, M. Breusing, R. Grunwald, J. Appl. Phys. 108 (2010) 043107-1.

100. P. Xiong, T. Jia, X. Jia, D. Feng, S. Zhang, L. Ding, Z. Sun, J. Qiu, Z. Xu, New Journal of Physics, 13 (2011) 023004-1.

101. J. He, Y. Qu, H. Li, J. Mi, W. Ji, Opt. Exp. 13 (2005) 9235.

102. M.G. Vivas, T. Shih, T. Voss, E. Mazur, C.R. Mendonca, Opt. Exp. 18 (2010) 9628.

103. D. Hofstetter, Y. Bonetti, F. R. Giorgetta, A. -H. El-Shaer, A. Bakin, A. Waag, R. S. Grund, M. Schubert, M. Grundmann, Appl. Phys. Lett, 91 (2007) 111108-1.

104. S. L. Chen, J. Stehr, N. K. Reddy, C. W. Tu, W. M. Chen, I. A. Buyanova, Appl. Phys. B, 108 (2012) 919.

105. W. Cao, W. Du, F. Su, G. Li, Appl. Phys. Lett. 89 (2006) 031902-1.

106. Y. C. Zhong, K. S. Wong, A. B. Djuristic, Y. F. Hsu, Appl. Phys. B 97 (2009) 125.

107. C. F. Zhang, Z. W. Dong, G. J. You, S. X. Qian, H. Deng, H. Gao, L. P. Yang, Y. Li, Appl. Phys. Lett. 87 (2005) 051920-1.

Chapter 2

Physical processes and experimental details

Various techniques of ZnO thin film deposition are reported in the literature. The present work has used PLD as the deposition technique. In this chapter, physical process involved in laser PLD is discussed briefly followed by brief description on the growth and characterization techniques used to study the nanostructures, and the PL setup used for laser induced PL studies.

2.1 Physical processes in PLD

A common feature of laser-target interaction resulting in the formation of plasma is the high degree of ionization and high electron and plasma temperature. The degree of ionization for plasma in local thermodynamic equilibrium is given by Saha equation [1]

$$\frac{n_i}{n_n} = 2.4\times10^{21}\frac{T^{\frac{3}{2}}}{n_i}e^{-U_n/K_BT} \qquad (2.1)$$

where n_i and n_n are the density (in m^{-3}) of ionized and neutral species, T (in K) is the temperature of the plasma, k_B is the Boltzmann constant, and U_n (in eV) is the ionization energy of the plasma, respectively. This results in the formation of a variety of species in the plasma, namely, neutral atoms, electrons, ions, molecules, clusters etc. One of the key applications of these species is in the the pulsed laser deposition. The properties of the deposited material thus depend upon various parameters related to the formation of plasma

(or ablation), namely, laser wavelength, laser energy, spot size, ambient pressure, target-substrate distance, choice of a suitable substrate, and deposition time.

PLD is considered as a three step processes – (a) laser-target interaction resulting in vaporization of material from target surface, (b) interaction of the laser with the expanding plasma resulting in inverse-Bremsstrahlung and photoionization which finally leads to transport of vapor plume and (c) adiabatic expansion resulting in the deposition of particles onto the substrate surface. The first two processes takes place during the laser pulse duration and the last one after its termination.

In PLD, high power laser is required for the vaporization of materials from target surface. Laser induced material removal includes etching and deposition of material. Material removal depends on the target properties such as wavelength dependent reflectivity (R), absorption coefficient (α), specific heat (C_v), vaporization energy (ΔH_v) and thermal conductivity (K) and also the laser parameters like laser wavelength, power density and pulse duration. In thermal process, absorbed laser photons result in thermal energy and cause vaporization. With the increase in energy of the photons further increase in kinetic energy takes place and results in an increase in the temperature of the material surface. A molten pool in a depth, defined as thermal diffusion length (L_{th}) given by $L_{th} = (2D_{th}\tau)$, is formed. τ is the laser pulse duration and D_{th} is the thermal diffusivity defined as $D_{th} = \frac{K}{\rho C_v}$. where, ρ is target density. If the surface temperature is sufficiently high, the molten pool attains the boiling temperature of the material and evaporation takes place. At this stage the deposited energy is equal to the latent heat of sublimation. Vaporization from material surface occurs in two ways: (a) optical absorption depth (α^{-1}) is small compared to L_{th} and (b) α^{-1} is larger than L_{th}. In most of materials, deposition occurs when the first condition gets satisfied. In both the

cases, vaporization of materials occurs if the heat absorbed per unit volume exceeds the latent heat of vaporization. So, threshold energy is required for material removal.

Once the vaporization takes place the incoming laser radiation is absorbed by the plasma vapor which is dominated by inverse-Bremsstrahlung (IB) and photoionization (PI). IB occurs when free electrons absorb the incoming photon and resulting in an increase in the kinetic energy. This increases the collisions and hence promotes ionization and vaporization. The absorption coefficient of the plasma, α_{IB} is given by the relation [2]

$$\alpha_{IB} = 3.69\times10^{8}\left(\frac{n_i^2\bar{Z}^3}{T_e^{\frac{1}{2}}\nu_L^3}\right)\left[1-\exp\left(-\frac{h\nu_L}{K_B T_E}\right)\right] \qquad (2.2)$$

where $\bar{Z}$ is the average charge, n_i is the ion density, T_e is the plasma temperature, h is the Planck constant, k_B is the Boltzmann constant, and ν_L is the frequency of the laser light, respectively. The laser energy is highly absorbed if ($\alpha_{IB}X$) is large, where X is the dimension perpendicular to the target surface. In the above equation it is assumed that the plasma frequency is less than that of the laser light frequency. The term [1-exp(-$h\nu_I/k_BT_e$)] represents the losses due to stimulated emission.

The increase in the density of the plasma due to increase in kinetic energy is not indefinite. At a critical density given by $n_c = [m_e\omega^2/4\pi e^2]$, the plasma becomes opaque to the incident radiation and is reflected back. ω is the laser frequency, e is the charge of electron, and m_e is the mass of electron. The plasma density thus decreases and the laser radiation again start to interact with the plasma. The process thus goes into a self-regulating regime.

For visible and UV laser ablation process, IB absorption is less efficient, however direct PI of excited atoms can be significant. The absorption coefficient α_{PI} (in cm^{-1}) of the process is given by [3]

$$\alpha_{PI} = \sum_n 2.9\times10^{-17} \frac{U_n^{\frac{5}{2}}}{(h\nu_L)^3} N_n \qquad (2.3)$$

where $h\nu_L$ is the photon energy (in eV), U_n is the ionization energy (in eV), and N_n is the number density (in cm^{-3}) of the excited state n, respectively, and the summation is performed over the energy levels which satisfy the condition $h\nu_L > U_n$.

Finally, beyond the laser pulse, the plasma expands with all the energy that it has referred to as adiabatic expansion.

2.2 Target preparation

For depositing ZnO nanostructures, sintered ZnO targets were prepared to form ZnO plasma upon irradiation with high power laser. For Target preparation, 99.5% ZnO powder (Nice Chemicals Pvt. Ltd.) was grinded to obtain fine ZnO particles and then a few drops of poly venyl alcohol (PVA) solution was mixed as a binder with ZnO powder thoroughly and grinded again. The ZnO mixture thus formed was pressed to 13 mm diameter size (as per the size of the die) in a hydrolic pressure unit by giving a pressure of around 3 ton. The pellets were put into a furnace for sintering at 1000^0C temperature for 5 hours. After 5 hours, furnace was cooled down to room temperature by natural cooling and sintered ZnO pellets were taken out for the use as target in PLD experiments.

2.3 Substrate preparation

n-type silicon (Si) (100) substrate was used for the deposition of nanostructures. Si substrate was cleaned by 5% HF solution for removing the oxide layer onto it. After that substrate was cleaned by acetone and then again cleaned ultrasonically for 10 minutes in acetone. Substrate was taken out from acetone and dried to use for the deposition.

2.4 Pulsed laser deposition set-up

The schematic diagram of PLD set-up is shown in figure 2.1 and the photograph of PLD chamber used in lab is shown in figure 2.2.

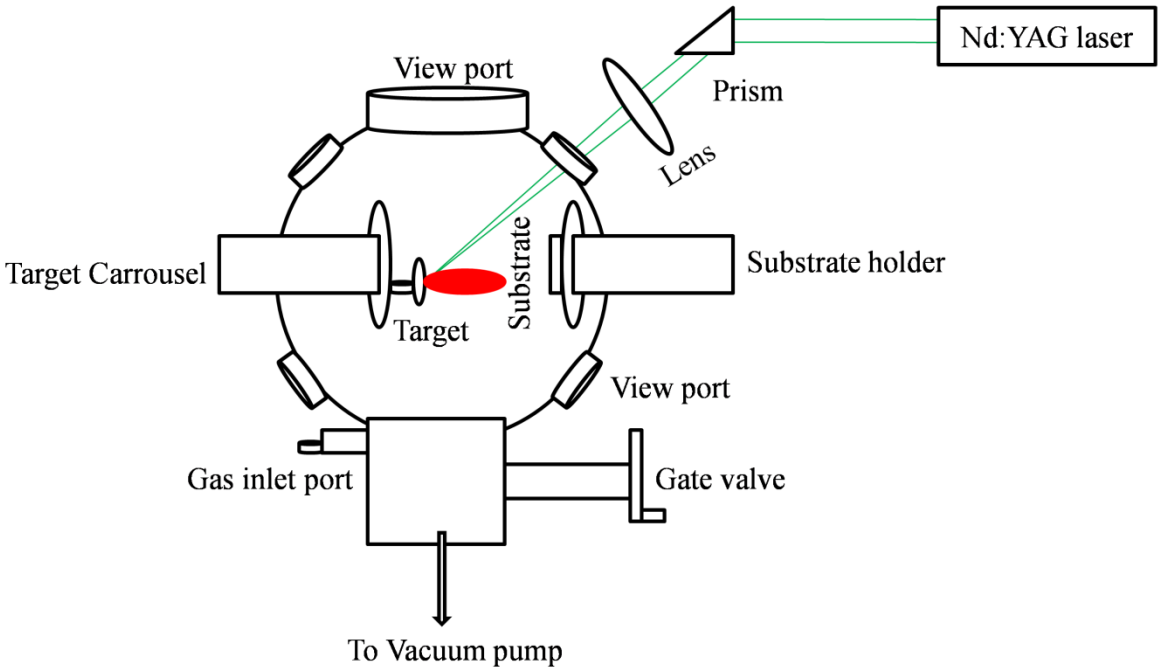

Figure 2.1: Schematic of PLD set-up.

The vacuum chamber used is a spherical chamber (diameter - 12 inch) made up of stainless steel with several view ports of different size. Q-switched Nd:YAG laser (HYL-101) of 532 nm wavelength, repetition rate of 10 Hz, pulse width of 10 ns was focused onto the target surface with a plano-convex lens of 35 cm wavelength.

In order to avoid drilling on the target surface, target was mounted on a motorized target carrousel, interfaced with Automated Target Carrousel Controller (ATCC). Target carrousel was mounted in one of the 150 CF view port. Substrate was mounted on a substrate holder with heating arrangement upto 800^0C.

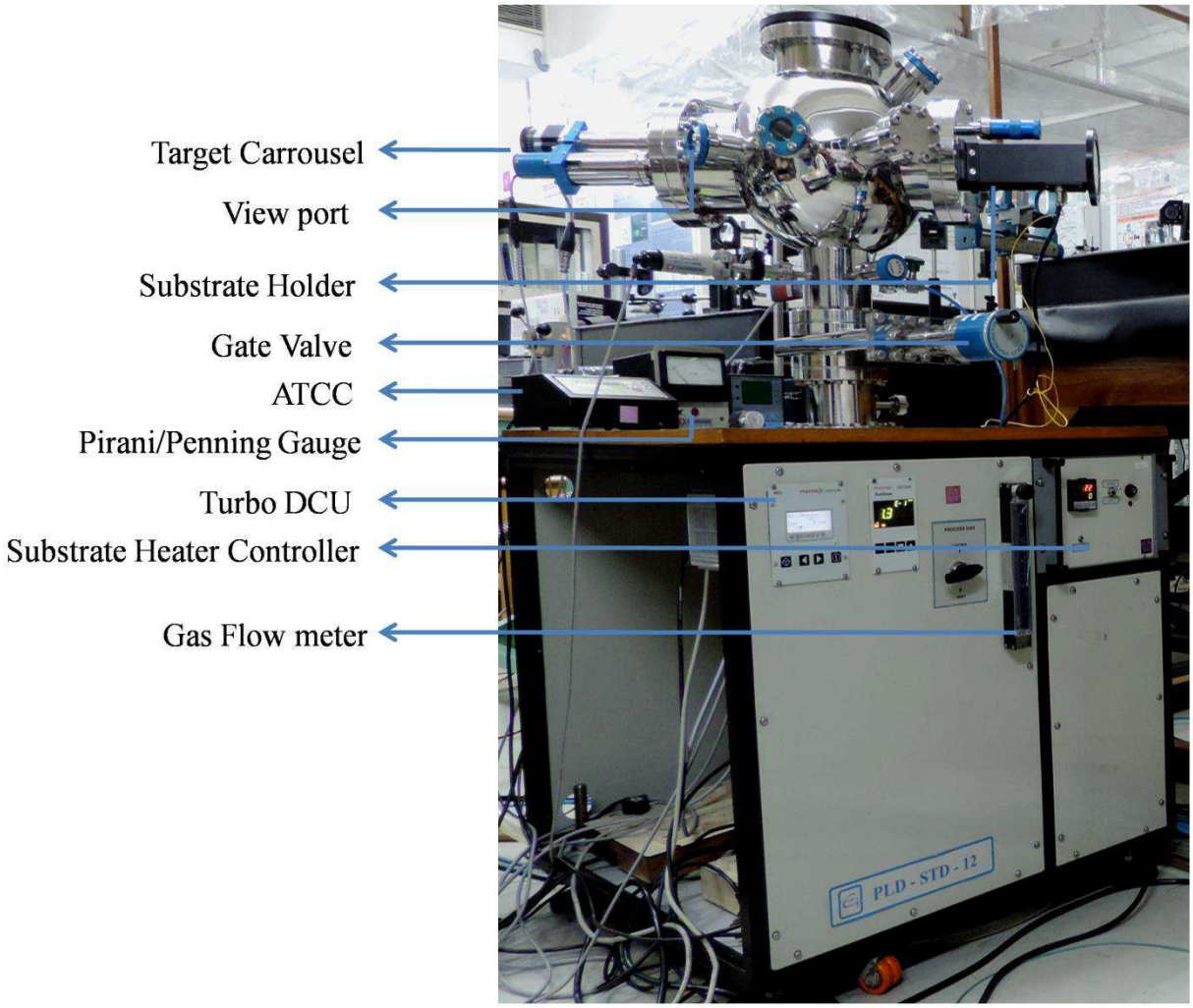

Figure 2.2: Photograph of PLD set-up.

Substrate holder was mounted exactly opposite to the target holder through the other 150 CF view port.

For achieving vacuum inside the chamber, rotary pump and turbo molecular pump (Hi Pace 300C) were connected to the bottom part of the chamber through a 100 CF port. For the flow of O_2 gas inside the chamber, O_2 gas cylinder was connected to the chamber through a gas flow controller. The pressure inside the vacuum chamber was monitored by Pirani (TECHNOVAC, AV-196A) and Penning gauge (TECHNOVAC, AV-196A) connected to the chamber through view ports.

For deposition, the chamber was evacuated to 10^{-6} mbar base pressure and then filled the chamber with O_2 gas (from 10^{-1} to 10^{-2} mbar). Substrate was heated from room temperature (RT) to 750^0C. The deposition time was varied from 5 to 60 minutes. The laser fluence was fixed at 12J/cm^2 and target-substrate distance was fixed at 4 cm throughout the deposition. The parameters varied to obtain various morphologies of ZnO nanostructures are given in table 2.1.

2.5 Characterization of nanostructures

The deposited nanostructures were characterized by various techniques to discuss crystallographic structure and orientation, thickness, surface morphology and optical properties by X-ray Diffraction (XRD), profilometer, field-emission scanning electron microscopy (FE-SEM), atomic force microscopy (AFM), photoluminescence spectroscopy (PL) and Micro-Raman spectroscopy, respectively.

XRD patterns [Bruker Advance D8 with Cukα radiation, seifert 3003-TT XRD, Rigaku TTRAX III] were recorded in θ-2θ mode using CuKα radiation of wavelength of 1.5406 A^0. The working principle of XRD is based on the diffraction from a set of planes in the atomic arrangement satisfying Bragg's law ($2d\sin\theta = n\lambda_x$), where d is interplaner spacing, θ is the angle of reflection, λ_x is the wavelength of x-ray and n is the order of diffraction. In XRD set-up, X-rays falls onto the sample surface and gets scattered by the atoms in the sample. The scattered light interferes constructively or destructively with each other and produces diffraction pattern. The angle at which XRD pattern is observed gives the information regarding the inter-planer spacing, material texture, lattice constants, strain, crystal structure and the crystallite size of the nanostructures.

Table 2.1: Parameters used for the deposition of ZnO nanostructures.

Chapter		Laser Fluence (J/cm^2)	Substrate	Substrate temperatures (^0C)	Deposition Time (minutes)	O_2 pressures (mbar)
Chapter 3	Sample set 1	12	Si	RT (23), 150, 300, 450 and 600.	20	0.1
	Sample set 2	12	Si	450	10, 20, 40 and 60	0.1
Chapter 4	Sample set 3	12	Si	RT (23), 150, 300, 450 and 600.	60	0.1
Chapter 5	Sample set 4	12	Si	RT (23), 150, 300, 450, 600 and 750.	60	0.05
Chapter 6	Sample set 5	12	Si	600.	45	0.01, 0.03 and 0.05.
	Sample set 6	12	Si	600.	5, 15, 30, 45 and 60	0.03

Photoluminescence spectra [ThermoSpectronic, AB2, monochromator xenon flash lamp] were recorded in the range of 360 – 630 nm for all the nanostructures by using excitation wavelength of 325 nm (~3.82 eV). In PL, photon gets absorbed by the semiconductor with energy greater than the band gap energy of semiconductor and results the formation of electron-hole pairs. The electron-hole pairs recombine radiatively and results in PL emission. The emitted light was collected by the detector to analyze the spectra. PL

spectra were recorded to identify the emissions from the nanostructures (due to near band-edge transition, defect levels etc.).

The Micro-Raman spectra (Lab Ram HR-800, Jobin Yvon) were recorded by using an Argon ion laser operating at a wavelength of 488 nm. Argon-ion laser was focused onto the thin film through a 50X microscope objective and the scattered light was collected through detector. In Raman spectroscopy, photon from incident light excites the molecule from ground state to a virtual state. This molecule relaxes to vibrational or rotational state and emits a photon. The difference in energy leads to a frequency shift from the excitation frequency. Raman shift provides the information about the crystallographic orientation, phonon modes of the molecules, defects and stress/strain present in the nanostructures.

Thickness of the nanostructures was measured by Dektak surface profilometer. For measuring the thickness of the nanostructures, a physical step was created on the sample during deposition by placing a small piece of Si on the sample surface. The movement of the sample with respect to the stylus measured the changes in surface height thus provided the sample thickness.

In FE-SEM (Sigma, Zeiss, Oberkochen, Germany), images of the ZnO nanostructures were recorded where a high energy electrons from field emission cathode in electron gun falls onto the sample surface and provides high quality magnified image of the surface. This gives the information about the morphology of the structures, size and its distribution, particulates present in the nanostructures etc.

AFM (Agilent 5500 series with PicoView image software) provides high resolution and three-dimensional images of the nanostructures. The images were recorded to obtain the surface pattern, mainly the surface roughness in the nano-order range. AFM consists of a cantilever with a sharp silicon tip at one of its end. AFM was operated in non-contact mode and when the tip comes closer to sample surface, deflection of the cantilever tip occurs due to

the force act between sample surface and cantilever tip. The deflection of the cantilever tip is measured by the reflection of laser light and the reflection is recorded by the position sensitive detector.

2.6 Set-up for laser induced PL

Lasing action from ZnO bulk as well as nanostructures is possible due to the formation of three different kinds of cavities – (a) random lasing cavity, (b) Fabry-Perot cavity and (c) whispering gallery mode cavity. In random lasing, lights gets scattered due to the random scatterers present in the system and light gets amplified along the closed loop feedback paths caused by the scattering from the scatterers. In Fabry-Perot cavity mode, lasing comes from single one-dimensional nanostructures where two smooth end-facets act as Fabry-Perot mirrors. In Whispering Gallery mode, six boundaries of the hexagonal cavity restrict the light waves and light propagates inside the cavity due to multiple total internal reflections from the end facets of hexagonal cavity.

In order to study the two-photon induced PL in bulk and nanostructured ZnO, a simple set-up (figure 2.3) was used.

A continuous wave Helium-Neon (He-Ne) laser (λ = 632 nm) of maximum 31.2 mW power was focused onto the sample by a lens of focal length of 25 cm and the emitted light was collected by a lens of 15 cm focal length at the entrance slit of monochromator (SPEX 750) to analyze the spectra. Both ZnO pellet and nanostructures were used to record the emission spectra. The neutral density filters were placed in front of the samples to vary the excitation power. The emission spectra were recorded at various excitation powers to study the number of photons involved in absorption process as well as lasing.

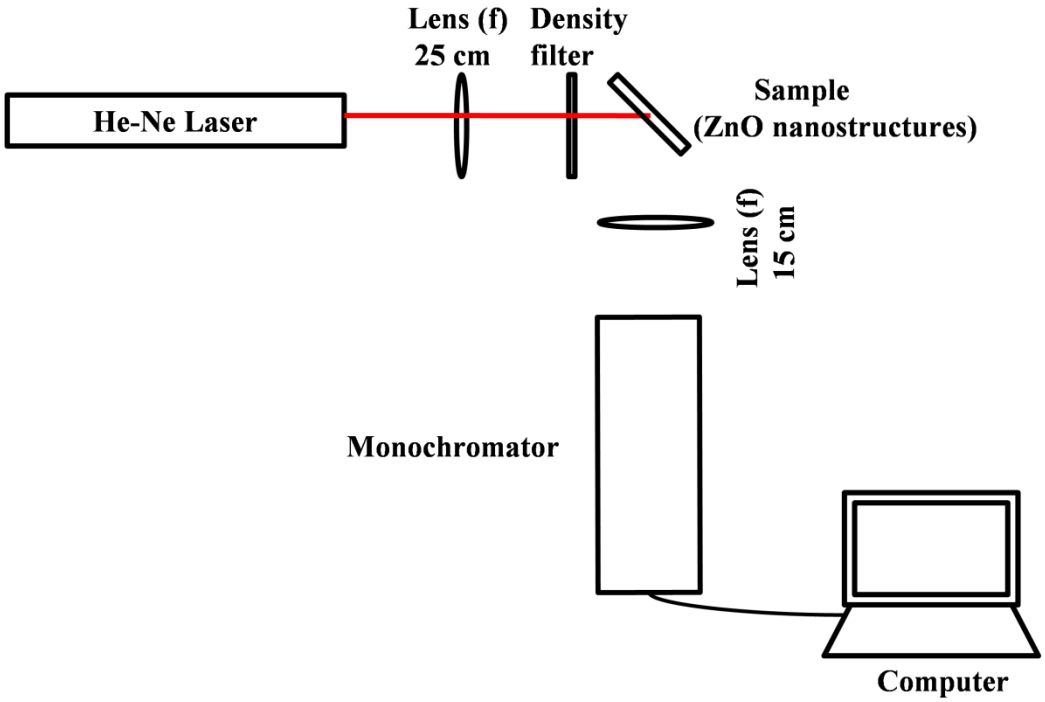

Figure 2.3: Schematic of PL set-up.

Bibliography

1. F. F. Chen, Introduction to Plasma Physics and Controlled Fusion, Springer, 2006.
2. R. K. Singh, J. Narayan, Phys. Rev. B 41 (1990) 8843.
3. S. Amoruso, R. Bruzzese, N. Spinelli, R. Velotta, J. Phys. B 32 (1999) R131.

Chapter 3

Pulsed laser deposited diamond-shaped ZnO nanostructures and their characterization

3.1 Introduction

Zinc oxide nanostructures with morphologies in the form of prism and pyramid are reported in the literature. These include pyramid-like [1], nanoprisms with pyramid tips [2], flat top pyramid-like [3], micropyramids [4], pyramid/prism tipped nanorods [5]. These nanostructures have been synthesized by hydrothermal synthesis [6], thermolysis of Zn-olate complex [1], solvothermal process [2], solid-vapour [3] and PLD methods [7]. The growth of prism/pyramidal faces of ZnO nanostructures is discussed in terms of the growth rates/growth velocities of planes in hexagonal structures of ZnO [6]. The disappearance of [0001] plane results due to the rapid growth velocity along the direction that leads to a pointed tip of the prism/ pyramid structures of ZnO. Also, due to the difference in the growth velocity of the two opposite faces $[0001], [000\bar{1}]$ two parallel hexagonal surfaces (length of one side is longer and other side is shorter) gives rise to flat-top pyramid-like structures [8]. The growth of pyramid-shaped nanostructures by PLD on silicon substrate at 600^0C has shown that the hardness of pyramid-shaped nanostructures is one order more than bulk ZnO as measured by nanoindentor [7]. The excitation power dependent PL spectra measured from diamond-like polyhedrons and microtubes with conical tip (referred as pyramid-shaped nanostructures) has shown lasing in UV range [9].

In this chapter, the growth and characterization of diamond-shaped ZnO nanostructures are reported. `The effect of substrate temperature as well as the deposition

time on ZnO nanostructures is discussed by studying its structural, optical and morphological properties. The formation of diamond-shaped nanostructures is discussed in terms of the growth rate of various planes of ZnO crystal. The role of PLD mechanism in the growth of these planes is also discussed. PL measurement shows intense emission in UV region and these structures are proposed for light emitting applications with studies reported in chapter 7.

3.2 Experimental details

ZnO nanostructures were deposited on Si (100) substrates by PLD set-up as discussed in chapter 2 (section 2.3). These nanostructures were deposited at room temperature (RT – 23^0C), 150, 300, 450, and 600^0C for 20 minutes in presence of O_2 gas at a pressure of 0.1 mbar. Target-substrate distance was fixed at 4 cm and laser fluence was kept around 12 J/cm^2. In order to understand the growth mechanism of diamond-shaped ZnO nanostructures, substrate temperature was fixed at 450^0C and nanostructures were deposited for 10, 40 and 60 minutes with other experimental parameters remaining the same.

Deposited nanostructures were characterized by XRD (Bruker Advance D8 with Cukα radiation), FE-SEM images, PL and Micro-Raman spectroscopy.

3.3 Results and discussions

3.3.1 *X-ray diffraction analysis*

XRD of ZnO nanostructures grown at various substrate temperatures were recorded by using a CuKα1 source at a wavelength of 1.5406 A^0. Figure 3.1 shows the XRD spectra of the nanostructures deposited at substrate temperatures ranging from RT to 600 ^{0}C and are identified with the available literature [2, 4, 5]. Figure 3.1 shows a broad and very less intense peak at 56.6^0 at RT corresponding to (110) plane indicating that the film is almost amorphous

as no preferred orientation is observed [10]. This peak is not observed at other temperatures in the present study. XRD peak corresponding to (002) plane is observed for all the nanostructures except at RT.

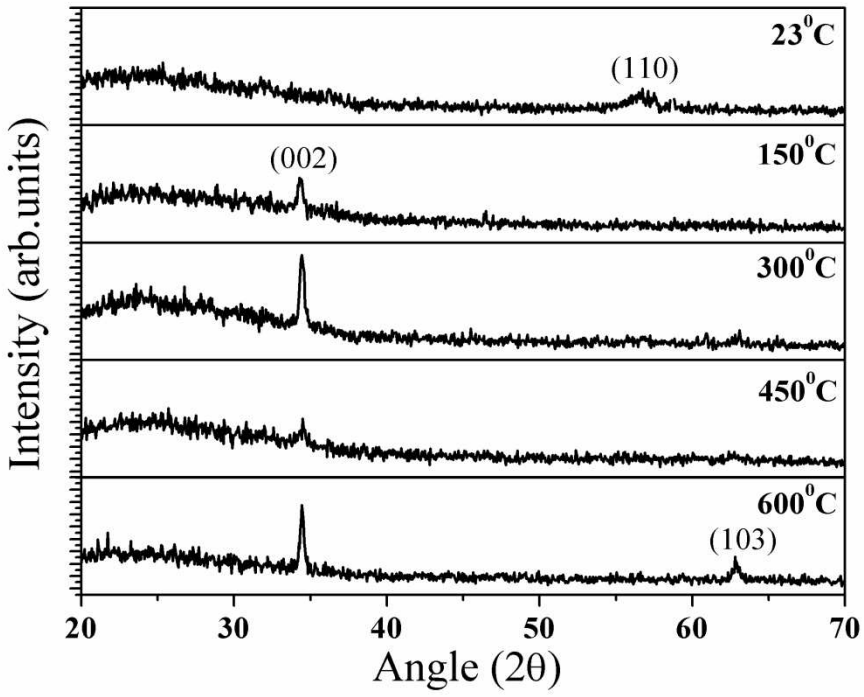

Figure 3.1: XRD spectra of the ZnO nanostructures grown at different substrate temperatures.

When the substrate temperature was increased beyond RT, XRD peak at 34.4^0 corresponding to (002) plane (JCPDS Number – ICSD#: 067849) appeared at 150, 300, and 450^0C respectively. Since this is the only plane observed at 150, 300, and 450^0C substrate temperatures, nanostructures have *c*-axis orientation and are single crystal in nature. At 600 ^{0}C substrate temperature, (103) plane at 62.8^0 along with (002) plane was observed in the nanostructures. The single crystal nature of the nanostructures beyond RT is due to the surface mobility of the impinging atoms sufficient enough to allow the atoms to occupy proper ZnO lattice sites. However, this will certainly not be true at sufficiently high temperatures, since the mobility will then be high enough to knock-out the atoms from

preferred lattice sites and the film will again tend to show polycrystalline nature. This indeed is observed for the thin films deposited at substrate temperature of 600^0C, where along with the peak corresponding to (002) plane, a less intense peak corresponding to (103) plane is observed [4]. The peak intensity of (002) plane increased gradually from 150 to 300 ^{0}C, decreased at 450^0C and increased again at 600^0C (figure 3.1). The intensity of ZnO (002) peak in XRD pattern mainly depends on the number of grains with the *c*-axis orientation, high crystallinity, and regular arrangement of nanoparticles in the thin film [10]. The observed intensity behavior can be attributed to an increase in the number of grains and crystallinity with *c*-axis orientation except at 450^0C substrate temperature.

At 450^0C, the intensity of the peak corresponding to (002) plane decreased drastically indicating that the nanostructures are not highly oriented, have poor crystallinity and irregular arrangement of nanoparticles. The full-width-half-maximum (FWHM) is inversely proportional to the film crystallinity [11]. The FWHM of the peak corresponding to (002) plane has a lower value for the films grown at 300 and 600^0C, and a higher value at 450 ^{0}C (table 3.1).

Table 3.1: FWHM of (002) XRD peak.

Substrate temperature (^{0}C)	**FWHM (degree)**
150	0.371
300	0.342
450	0.564
600	0.307

XRD studies on the growth of hexagonal pyramid-like microrods [4], prism-like nanostructures [2], pyramid-shaped nanocrystals [1], flat-top pyramids [3] have shown less

intense peak at (002) plane as compared to (100) and (001) planes. In the present case only (002) peak is observed with very low intensity for diamond-shaped particles grown at 450^0C.

The strain and stress present in the nanostructures are calculated by the formulae [12]

$$Strain = \frac{(d - d_0)}{d_0} \tag{3.1}$$

$$Stress = 4.5\times10^{11} \times Strain \tag{3.2}$$

where, d is the lattice spacing for ZnO nanostructures and d_0 is the lattice spacing of bulk ZnO. The strain along c-axis and stress present in the nanostructures are given in table 3.2. The change in sign indicates the nature of the stress, whether it is tensile or compressive [13, 14]. It is observed that the stress and strain present in the nanostructures are less indicating almost stress free nanostructures.

Table 3.2: Variation of strain and stress values with substrate temperatures.

Substrate temperature (^{0}C)	Strain	Stress (GPa)
150	0.00047	-0.172
300	-0.00058	0.173
450	-0.00058	0.173
600	-0.00092	0.346

3.3.2 *Surface morphology*

Figure 3.2(a-e) shows the FE-SEM images of the ZnO nanostructures deposited at RT, 150, 300, 450, and 600^0C, respectively, at O_2 pressure of 0.1 mbar. Diamond-shaped structures are prominently observed at 450^0C substrate temperature as shown in figure 3.2(d), however, at 150^0C a few such structures are observed. The formation of diamond-shaped

structure of ZnO deposited by various deposition processes is reported in the literature [1-3, 6, 7].

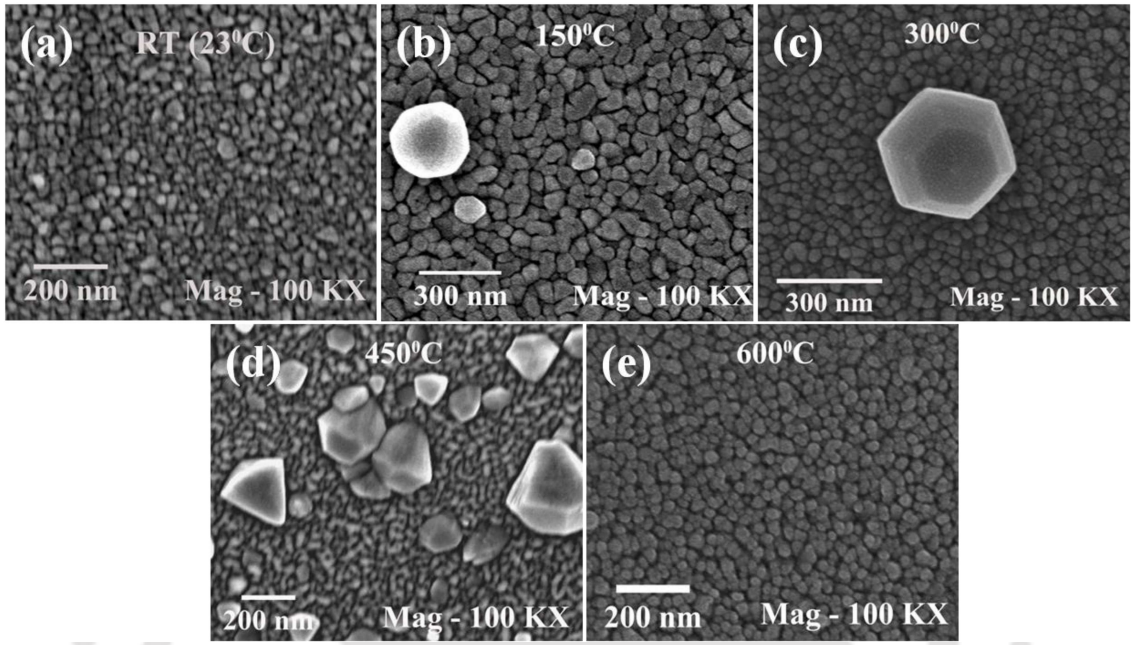

Figure 3.2(a-e): FE-SEM images of the nanostructures grown at different substrate temperatures.

We believe that the formation of diamond-shaped ZnO also follows the mechanism responsible for the growth of pyramid-like structures and more conducive at the reported temperatures (150 and 450^{0}C) and predominantly at 450^{0}C. Though the reason for the growth of diamond-shaped structures at 450^{0}C substrate temperature is not very clear, we have attempted to discuss the formation of diamond-shaped structures with respect to the growth rates of several faces of ZnO [5, 7] as discussed in the next paragraph on page 38. Figure 3.3 shows the variation of number of particles with particle size for the nanostructures at various substrate temperatures. After measuring the particle size from FE-SEM images, it has been observed that the average particle size is larger for the substrate temperatures 150 and 450^{0}C. At substrate temperature of 300 and 600^{0}C, particle size decreases. In the present case, particle size variation with substrate temperature doesn't follow a trend. Average particle size

increases from RT to 150^{0}C, then decreases again at 300^{0}C, again increases at 450^{0}C and decreases at 600^{0}C. This kind of particle size variation with substrate temperature has been reported in a recent work [15].

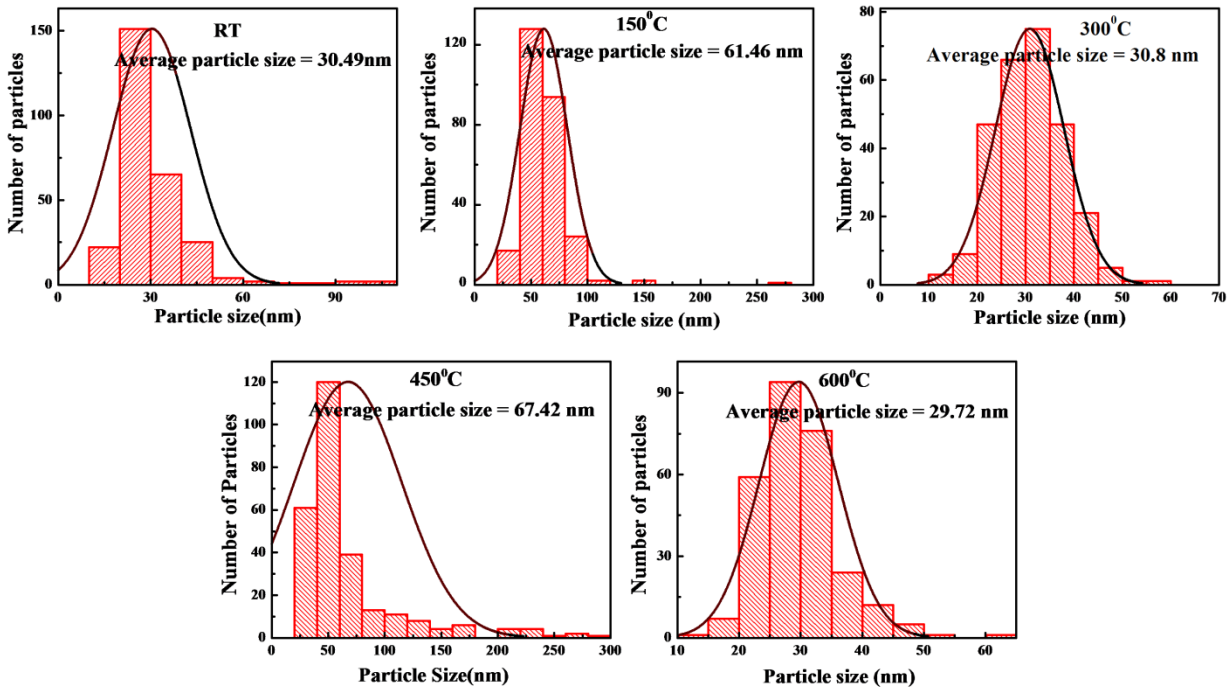

Figure 3.3: Particle size distributions of the nanostructures grown at different substrate temperatures.

We attempted to look at the growth of diamond-shaped structures at 450^{0}C by depositing these structures for 10, 20, 40 and 60 minutes, respectively. The FE-SEM images of the nanostructures are shown in figure 3.4(a-d). Figure 3.4(a1) is the enlarged view of a section of figure 3.4(a). For 10 minutes deposition, a few diamond-shaped particles along with background particles are observed. In addition to these structures, several hexagonal structures are clearly observed whereas they are not observed at other deposition temperatures. For 20 minutes deposition, diamond-shaped structures along with various shaped nanoparticles in the background are observed whereas for the sample with 40 minutes

deposition, the various shaped nanoparticle with a few diamond-shaped structures are observed.

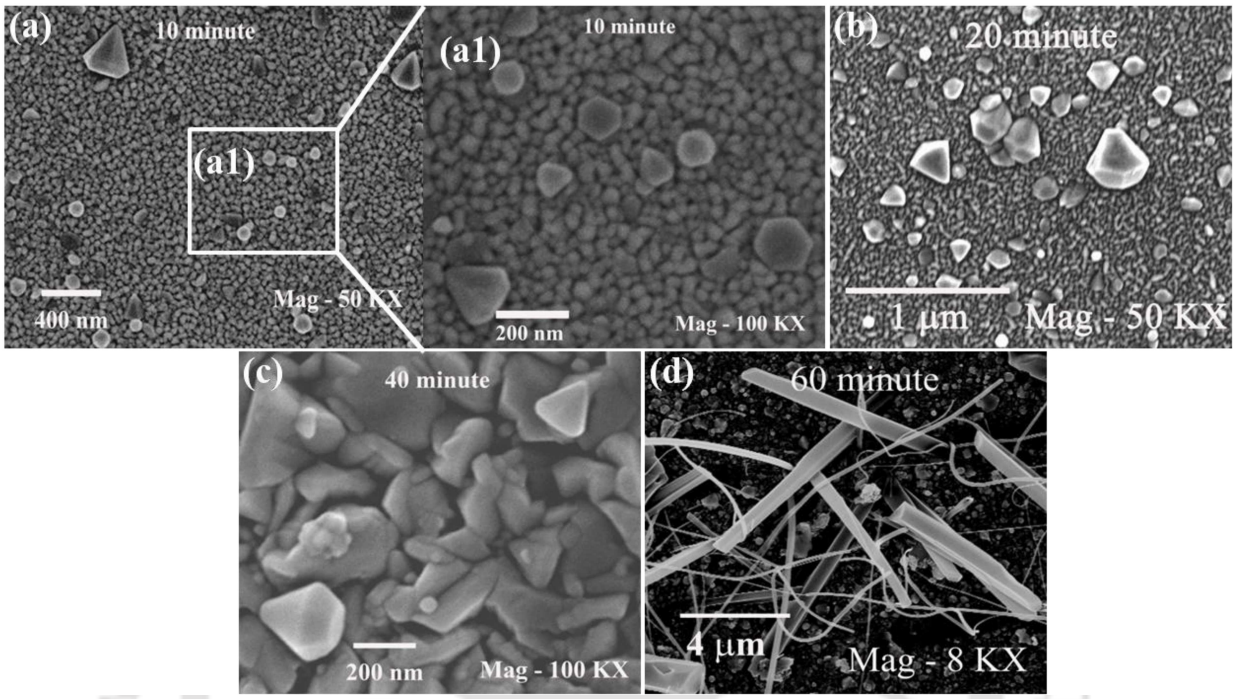

Figure 3.4(a-d): FE-SEM images of the nanostructures grown at different deposition times.

The size of the diamond-shaped structures is much larger than the background particles for the sample with 20 minutes deposition time as well as for 10 minutes unlike the sample with 40 minutes (figure 3.4(c)) deposition time where the size of the nanoparticles is larger than the size of the diamond-shaped structures. However, for 60 minutes time (figure 3.4(d)), both the nanorods and nanowires are observed.

As the substrate temperature remains fixed for the deposition of all nanostructures, the substrate temperature gives the same amount of surface mobility to the deposited atoms to get to the lowest thermodynamically favored lattice positions and therefore the deposition time plays an important role in the growth of these nanostructures. For 10 minute, very few diamond-shaped structures are observed whereas many clear hexagonal structures (in a

rectangular white colour box) of size around (40-50 nm) are observed in the background. As we increase the deposition time to 20 minutes more diamond-shaped structures are observed with slightly increased size. The size of the background particles remains the same and the hexagonal structures are not visible for 20 minutes deposition.

The diamond-shaped structure can be explained in terms of the different growth rates of the hexagonal planes. Various planes that may contribute to the growth habit of ZnO includes $[0001]$, $[000\bar{1}]$, $\{01\bar{1}1\}$, $\{01\bar{1}0\}$, and $\{01\bar{1}\bar{1}\}$, respectively [6, 7]. Figure 3.5 shows these directions as observed in the growth of diamond-shaped structures in the present work. We observed that the growth along [0001] is maximum and hence the XRD shows a drastic dip in the (002) direction. The absence of the plane along $\{01\bar{1}0\}$ gives rise to the diamond-shaped structure. The growth velocity seems to follow the trend $V_{[0001]} > V_{\{01\bar{1}1\}} > V_{\{01\bar{1}\bar{1}\}} > V_{[000\bar{1}]}$ (figure 3.5).

In this work, the ratio of the length of the longer region to that of the shorter region of the diamond-shaped structure is found to be around 3:1 [8] elucidating the formation of diamond-shaped structure. The measurement of the length of two faces of diamond-shaped nanostructures for 20 and 40 minutes deposition time is given in table 3.3 and table 3.4.

For the nanostructures grown for 10 minutes the FE-SEM images show several hexagonal structures (size ~ 50-60 nm) along with very few diamond-shaped structures (small sized). For 40 minutes deposition time, very few diamond-shaped structures of same size are observed while the size of the background particles increased drastically. As the size of the background particles is more than the diamond-shaped particles, very few diamond-shaped structures are observed.

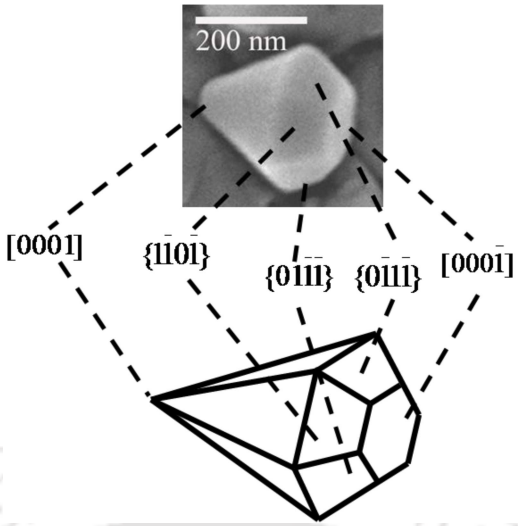

Figure 3.5: Growth mechanism of diamond-shaped structure.

Table 3.3: Ratio of lengths of two opposite faces of diamond-shaped structures for 20 minutes deposition.

Length of diamond structure along (001) direction (nm)	Length of diamond structure in the opposite of (001) direction (nm)	Ratio of the lengths of two opposite faces in opposite direction.
112.5	39.5	2.8:1
122.7	22.0	5.6:1
65.4	24.4	2.7:1
223.0	66.7	3.3:1
176.5	80.0	2.2:1
178.7	75.8	2.4:1
239.4	109.1	2.2:1
88.1	57.6	1.5:1
100.2	36.5	2.7:1
96.3	28.7	3.3:1

In the literature, the growth habit of ZnO crystal is also discussed in terms of three basic theoretical models describing the crystal growth habit, namely, (a) the Bravais Friedel Donnay Harker (BFDH) law, (b) the Periodic Bond Chain theory (PBC), and (c) the theory of growth of basic structural unit of negative ion coordination polyhedron [3, 6]. According to BFDH law, relative growth rates of various crystal faces are inversely proportional to the

planar mesh density, and classification of the crystal faces is based on how easily they appear or disappear.

Table 3.4: Ratio of lengths of two opposite faces of diamond-shaped structures for 40 minutes deposition.

Length of diamond structure along (001) direction. (nm)	Length of diamond structure in the opposite of (001) direction (nm)	Ratio of the lengths of two opposite faces in opposite direction.
135.9	82.4	1.6:1
129.5	35.4	3.7:1
243.7	96.0	2.5:1
123.1	35.9	3.4:1

The PBC theory provides growth habit in terms of the bond chain types between the molecules and attachment energy. The third model is based on the arrangement of negative ion coordination polyhedron growth units resulting in different growth rates in different directions. In BFDH and PBC approach, the top and bottom surfaces ($[0001]$ and $[000\bar{1}]$) have the same properties. Since different relative growth rates of the two faces $[0001]$ and $[000\bar{1}]$ are observed in the present work (see table 3.3 and 3.4), these two approaches are not applicable to discuss the morphology. The third model describes the arrangement of coordination polyhedron at different interfaces. The studies on this approach including growth mechanism are reported either using carbon thermal reduction method (solid-vapor growth process) or by hydrothermal growth mechanism where the growth rate of various crystal faces is related to the way the coordination polyhedron arranges itself at the interface [3, 6].

The presence of liquid helps in providing enough time to the reacting species to form the crystals with various planes. However, in PLD, the growth rate is fast and the growth of

various planes will also be affected by the external parameters and in the present case by temperature (since other physical parameters were kept constant like pressure, deposition time and laser fluence). The diamond-shaped structures do not show the $\{01\bar{1}0\}$ plane. It indicates that this surface has the slowest growth rate as compared to other planes. So slow that by the time the $[0001]$ plane disappeared, it could not have even started to grow. The ambient oxygen collides with the ablated ZnO plasma thereby generating ionic species corresponding to both O and Zn due to high kinetic energy of the electrons. These electrons in effect ionize the Zn and O located at the tetrahedron in the plasma which essentially is the growth unit of the ZnO. The substrate temperature provides the mobility to these units so as to bond to form the coordinating tetrahedrons. These units though exist at all temperatures, however, at sufficiently low and high temperatures are not stable and do not give rise to diamond-shaped structures.

3.3.3 *Photoluminescence*

PL studies were carried out by using a Xenon flash lamp operating at 325 nm as the excitation source. Figure 3.6 shows the PL spectrum of ZnO thin films at O_2 pressure 0.1 mbar and at different substrate temperatures (RT, 150, 300, 450, and 600^0C). It is observed that PL emission in the UV region (378-395 nm) and defect-related emission (467 nm) in blue-green region in the deposited nanostructures. As discussed in chapter 1, PL emission in the range of (373-397 nm) is due to near band edge transition and corresponds to free exciton-exciton recombination [16]. Liu et al. [10] and Fan et al. [11] studied the effect of substrate temperature on the intensity and FWHM of PL emission in the UV range and observed enhancement in the PL intensity and narrowing in FWHM. This observation in the reported temperature range (400 – 500^0C) showed the film with strong *c*-axis orientation corresponding to (002) peak as observed in their XRD spectra.

At RT, the crystallinity is poor. As we increase the temperature the crystallinity improves and at 150 and 450^{0}C, PL intensity increases. But from XRD results, it is clear that the films grown at these temperatures have poor crystalline quality and do not have intense (002) peak.

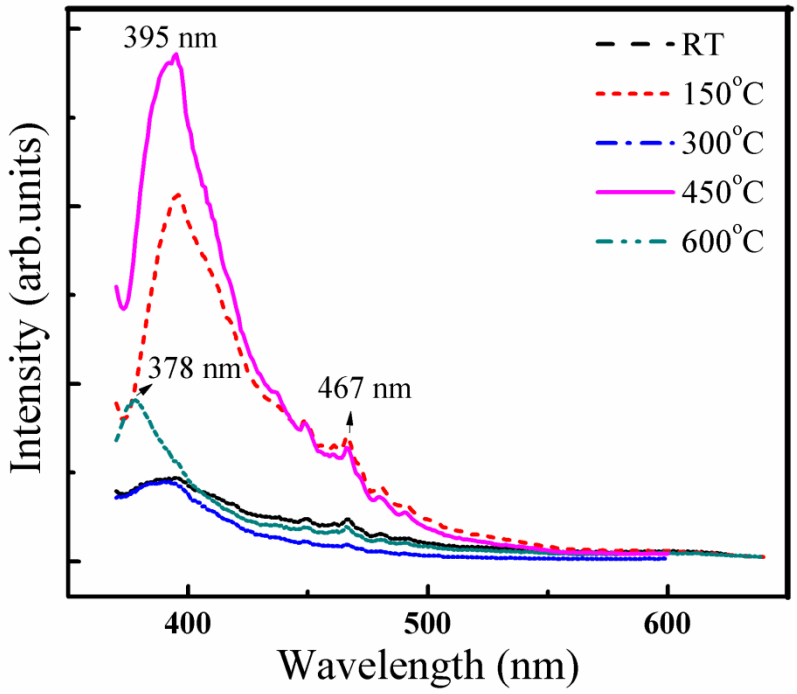

Figure 3.6: PL spectra of the nanostructures grown at different substrate temperatures.

The possible reason for such a high intense peak could be the growth of particulates distributed randomly and possibly with shapes different from the ones compared to that grown at other substrate temperatures.

As discussed in the previous section, diamond-shaped structures on the grown films (in agreement with the FE-SEM images shown in figure 3.2(b) and figure 3.2(d)) were observed and therefore multiple reflections from the facets of such structure will result in an enhancement in the PL intensity. PL intensity is more at 450^{0}C as compared to 150^{0}C since the number of diamond-shaped structures are more at 450^{0}C.

The blue-green peak at 467 nm is due to the defect levels such as oxygen vacancies or the interstitial Zn [18]. Low intense blue peaks are observed in all the nanostructures. Slightly intense blue peaks are observed at 150 and 450^{0}C and are attributed to the interstitial Zn defect. Weaker deep level emissions at around 600 nm are also observed in the nanostructures. These deep level emissions are due to the structural defects. But, negligibly weak deep level emission compared to strong UV emission demonstrates that the deposited nanostructures have low structural defects [11, 19]. The photoluminescence spectra recorded from this prism/pyramid shaped nanostructures gives strong emission nearly at 390 nm [1, 5] and defect related emission at 468 nm [1] which is in agreement with the PL spectra recorded in the diamond-shaped nanostructures.

Figure 3.7 is the plot of the ratio of the intensity of UV to Visible (blue-green) region with the substrate temperature. This ratio is maximum for the structures grown at 300 and 600^{0}C indicating the low structural defects in the nanostructures. This ratio is lowest at RT. However, this ratio is more at 150 ^{0}C than at 450^{0}C indicating more structural defects at 450^{0}C. This is also consistent with the XRD results.

Figure 3.8 shows the PL spectra of the nanostructures deposited at 450^{0}C for 10, 20, 40 and 60 minutes. The near band edge emission at around 395 nm and defect related emissions at 467 nm and 595 nm are observed for all the nanostructures. Strong UV emission is observed for all the nanostructures. This is due to free exciton-exciton recombination corresponding to near band edge transition of wide band gap ZnO [16]. The blue peak at 467 nm [18] comes from the defect related states such as oxygen vacancy or interstitial zinc. The weak and broad yellow emission at around 600 nm and is due to the deep levels caused by some defects like interstitial oxygen [20]. The variation of intensity of near band edge peak and the width of that peak with deposition time shows that the intensity of near band edge

peak of the nanostructures deposited for 20 minute is higher than the other nanostructures since there are more diamond-shaped structures.

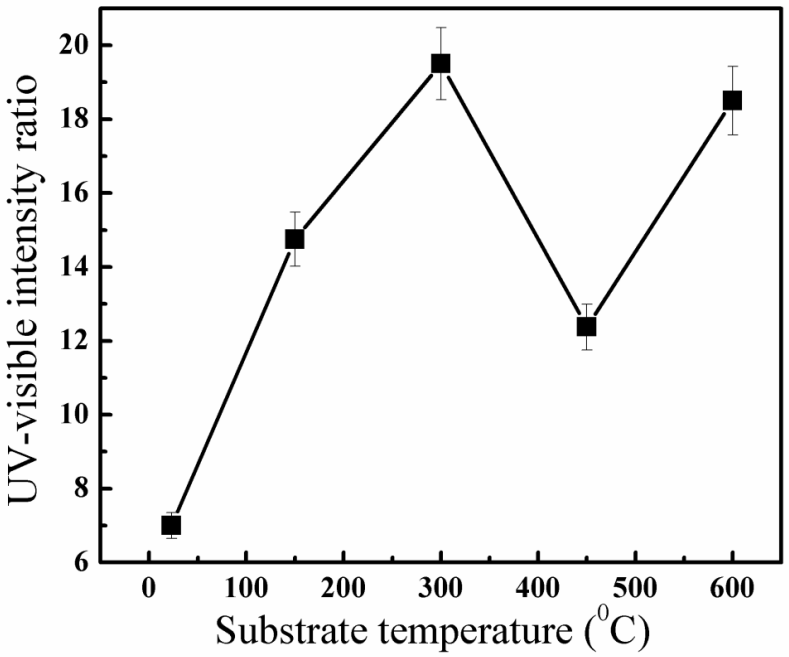

Figure 3.7: Variation of UV-visible emission intensity ratio with substrate temperature.

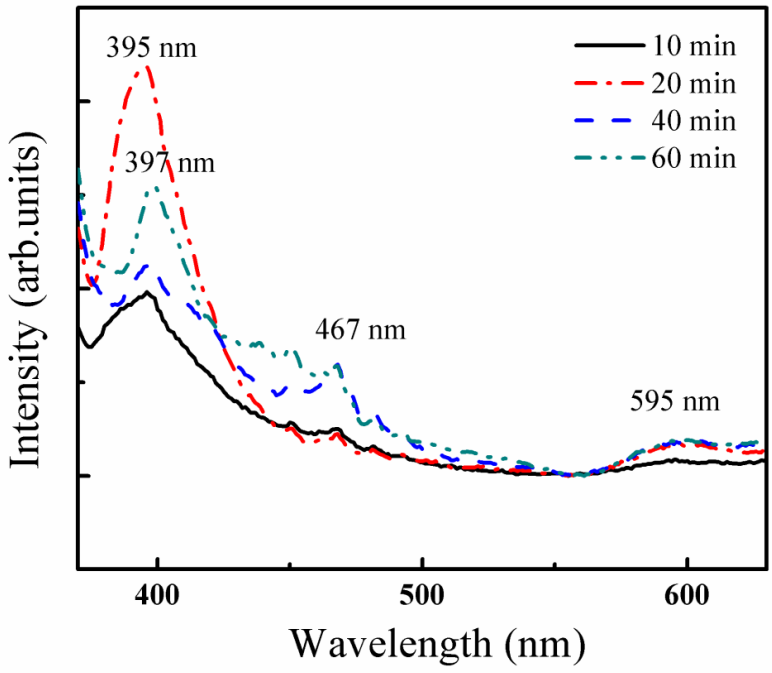

Figure 3.8: PL spectra of the nanostructures grown at different deposition times.

PL studies of pyramid and prism shaped ZnO nanostructures [1, 2] and for pyramid shaped nanostructures [1] shows near band edge peak at around 387 nm and blue green peak at 468 nm. The UV emission is highly intense than that of blue-green emission. This trend in the diamond-shaped ZnO nanostructures indicates better optical properties.

3.3.4 *Micro-Raman analysis*

The Micro-Raman spectra were recorded by using an Argon ion laser operating at a wavelength of 488 nm. ZnO has the wurtzite structure and belongs to C_{6v}^4 space group. Group theory predicts the existence of the following optic phonon modes [21],

$$\Gamma_{opt} = A_1+2B_1+E_1+2E_2$$

where A_1 and E_1 modes are polar and split into transverse optical (A_1 TO and E_1 TO) and longitudinal optical (A_1 LO and E_1 LO) components. E_2 mode consists of two modes of low and high frequency phonons (E_2 low and E_2 high) which are associated with the vibration of the heavy Zn sub lattice and oxygen atoms, respectively. B_1 (low) and B_1 (high) modes are at 260 cm^{-1} and 540 cm^{-1}, respectively [21]. Two B_1 modes are not Raman active [21]. High frequency E_2 mode characterizes the wurtzite phase of ZnO [22]. The second order vibrations are at 208 and 330 cm^{-1}. The broad peak at 330 cm^{-1} is attributed to second-order Raman process. The broad peak at 663 cm^{-1} belongs to the multiphonon process [21]. The Raman modes for bulk ZnO and ZnO nanostructures are listed in table 3.5. In bulk ZnO, E_2(high) and E_2(low), A_1(TO), E_1(TO) and E_1(LO) modes were observed. Also, the Micro-Raman peaks at 331 cm^{-1} and 661 cm^{-1}, attributed to second order Raman process, were also observed.

Figure 3.9 shows the Micro-Raman spectra of ZnO nanostructures deposited at RT, 150, 300, 450, and 600^{0}C, respectively, and at O_2 pressure of 0.1 mbar. E_2(low), E_2(high) modes are at 102 cm^{-1} and 439 cm^{-1} respectively for all the nanostructures. E_2(low) is

associated with Zn sublattice and E_2(high) is associated with the oxygen atoms [21, 23]. E_2 (high) mode is observed in all the nanostructures and its intensity for the nanostructures deposited at 150 and 450^{0}C substrate temperature are comparable than that deposited at other substrate temperatures.

Table 3.5: Raman modes of bulk ZnO and ZnO nanostructures.

Phonon modes	**E_2(low)**	**Multi phonon**	**A_1(TO)**	**E_1(TO)**	**E_2(high)**	**A_1(LO)**	**E_1(LO)**
Bulk ZnO	99 cm^{-1}	331 cm^{-1}, 661 cm^{-1}	380 cm^{-1}	408 cm^{-1}	437 cm^{-1}		584 cm^{-1}
ZnO nanostructures	102 cm^{-1}			403 cm^{-1} (Only at 150^{0}C)	439 cm^{-1}	576 cm^{-1}	

The presence of E_2 (high) mode confirms the wurtzite structure [22, 23]. The Raman peak at 303 cm^{-1} is observed due to the multiphonon feature of Si [24]. E_1 (TO) mode at 403 cm^{-1} and A_1(LO) mode at 576 cm^{-1} are observed at 150^{0}C. Frequency shift in E_1(TO) mode is considered due to stress in contact with the substrate [25] but its value is less as confirmed from XRD results. The width for the E_2(high) mode calculated from the Lorentzian fit of the Raman spectra at various temperatures is plotted in figure 3.10. It is maximum at 450^{0}C and minimum at other substrate temperatures. The narrow width of the E_2(high) mode at 300 and 600^{0}C as compared to that at 450^{0}C indicates better crystallinity at those temperatures [21] consistent with the XRD results.

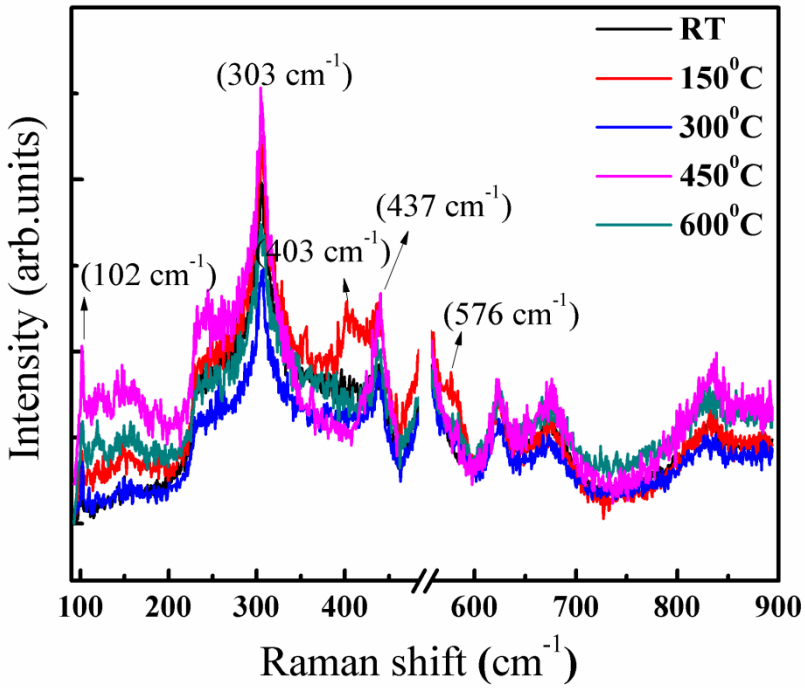

Figure 3.9: Micro-Raman spectra of the nanostructures grown at different substrate temperatures.

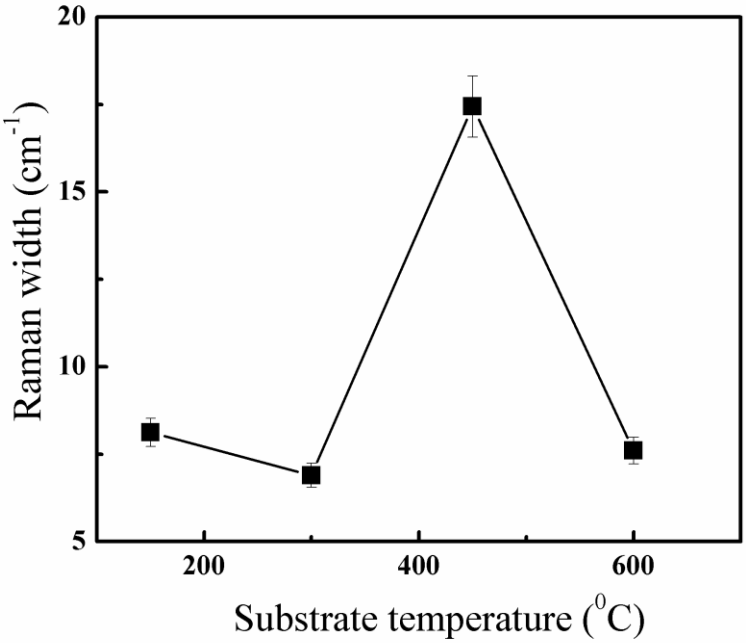

Figure 3.10: Variation of width of E_2(high) mode with substrate temperature.

3.4 Conclusions

Diamond-shaped ZnO nanostructures were synthesized successfully by PLD technique without using any catalyst at substrate temperatures of 150^0C (very few) and predominantly at 450^0C. XRD data showed that the nanostructures have strong *c*-axis orientation (along (002) direction). Nanostructures also exhibited less strain and stress. FE-SEM images showed the formation of diamond-shaped structures at 150 and 450^0C substrate temperatures indicating high growth rate along (0001) plane, and hence a sharp decrease in (002) peak intensity in the XRD data. The growth mechanism of diamond-shaped nanostructures was studied by varying the deposition time at substrate temperature of 450^0C. The growth is attributed to the growth rate of (0001) plane. Deposition time seems to play an important role in the formation of these structures as at 60 minutes the formation of nanorods/wires was observed. PL spectra showed intense emission in the UV region as compared to blue-green emission for the diamond-shaped nanostructures. The strong emission in the UV region for diamond-shaped nanostructures is attributed to the multiple reflections. This is an indication of probable use of such structures as light emitting devices. Micro-Raman analysis of the nanostructures revealed the wurzite nature of grown nanostructures.

Bibliography

1. S-H. Choi, E-G. Kim, J. Park, K. An, N. Lee, S. C. Kim, T. Hyeon, J. Phys. Chem. Letters B, 109 (2005) 14792.
2. D. Wang, C. Song, J. phys. Chem. B, 109 (2005) 12697.
3. MA Shufang, L. Jian, L. Xuguang, Z. Junfu,, XU Bingshe, Journal of Wuhan University of Technology – Mater. Sci. Ed. Feb 2011, DOI: 10:1007/s11595-011-0159-7.

4. M. Pudukudy, Z. Yakob: Superlattices and Microstructures, 63 (2013) 47.

5. Z. Zhang, J. Mu, J. Colloid. Interface. Sci, 307 (2007) 79.

6. W-J. Li, E-W. Shi, W-Z. Zhong, Z-W. Yin, J. Cryst. Growth. 203 (1999) 186.

7. S. Angappane, N. S. John, G. U. Kulkarni, Pyramidal Nanostructures of ZnO J. Nanoscience.Nanotechnol. 6 (2013) 101.

8. H. Morkoc and U. Ozgur, Zinc Oxide Fundamentals, Materials and Device Technology, Chapter 2 [section 2.1]

9. H. Dong, L. Sun, W. Xie, W. Zhou, X. Shen, Chen, Z. J. Phys. Chem. C 114 (2010) 17369.

10. M. Liu, X. Q. Wei, Z. G. Zhang, G. Sun, C. S. Chen, C. S. Xue, H. Z. Zhuang, B. Y. Man, Appl. Surf. Sci. 252 (2006) 4321.

11. S. S. Kim, B. T. Lee, Thin solid Films 446 (2004) 307.

12. A. Ismail, M. J. Abdullah, Journal of King Saud University-Science 25 (2013) 209.

13. G. Anil Kumar, M. V. Ramana Reddy, K. N. Reddy, Journal of Physics: Conference Series 365 (2012) 012031.

14. V. Gupta, A. Mansingh, J. Appl. Phys. 80 (1996) 1063.

15. K. A. Eswar, J. Rouhi, H. F. Husairi, M. Rusop, S. Abdullah, Advances in Material Science and Engineering, Vol-2014, Article ID-796759 (6 pages)

16. G. Kenanakis, M Androulidaki, E. Koudoumas, C. Savvakis, N. Katsarakis, Superlattices and Microstructures 42 (2007) 473.

17. X. M. Fan, J. S. Lian, Z. X. Guo, H. J. Lu, Appl. Surf. Sci. 239 (2005) 176.

18. Y. H. Yang, Y. Feng, G. W. Yang, Appl. Phys. A, 102 (2011) 319.

19. O. Lupan, G. A. Emelchenko, V. V. Ursaki, G. Chai, A. N. Redkin, A. N. Gruzintsev, I. M. Tiginyanu, L. Chow, L. K. Ono, B. Roldan Cuenya, H. Heinrich, E. E. Yakimov, Mater. Res. Bull. 45 (2010) 1026.

20. H. Zhang, R. Xie, T. Sekiguchi, X. Ma, D. Yang, Mater. Res. Bull. 42 (2007) 1286.

21. R. Zhang, P. G. Yin, N. Wang, L. Gou, Solid State Sci. 11 (2009) 865.

22. N. Tripathi, K. Vijayarangamuthu, S. Rath, Mater. Chem. & Phys. 126 (2011) 568.

23. S. K. Panda, C. Jacob, Appl. Phys. A 96 (2009) 805.

24. B. Yang, A. Kumar, P. Feng, R. S. Katiyar, Appl. Phys. Lett. 92 (2008) 233112.

25. S. B. Yahia, L. Znaidi, A. Kanaev, J. P. Petitet, Spectrochim. Acta A 71 (2008) 1234.

Chapter 4

Pulsed laser deposited combination of ZnO nanorods and nanowires and their characterization

4.1 Introduction

ZnO nanowires have gained tremendous research interest because of their applications in optical, electrical and mechanical fields such as in light emitting devices [1, 2, 3], UV detectors [2, 4], field effect transistors, field emission devices [2, 5], nanogenerators [2, 6], sensors [5] etc. ZnO nanorods (including size confinement and doping) are also useful in various optoelectronic and mechanical applications such as lasing emission, luminescence, field emission, electron transportation, sensing [7] etc. ZnO nanostructures show emissions in UV and visible regions due to excitons, shallow donor/acceptor levels, interstitial and antisite zinc and oxygen, and zinc and oxygen vacancies [8].

ZnO nanorods have been grown by hydrothermal method [9], chemical method [10], PLD [11] etc. ZnO nanowires have been grown by thermal evaporation [12], PLD [13], Chemical vapour deposition [14] etc.

Several groups have synthesized ZnO nanowires with the help of PLD technique. Rahm et al. synthesized regular arrangement of ZnO nanowires on sapphire substrate by using Au as a catalyst [13]. Sun et al. reported ZnO nanowires deposited by PLD in two ways. One is directly on Si substrate at high temperature and other one is on the seed layers of ZnO grown on Si substrate [15]. These reported nanowires are highly (002) oriented. Another reported nanowire structures are polycrystalline in nature but have intense peak along (002) direction, synthesized by thermal oxidation of Zn thin films on glass substrate

[16], thermal evaporation method on *n*-type silicon substrate [12] etc. ZnO nanorods grown on sapphire, Si, glass, substrates are shown to be polycrystalline in nature when deposited by chemical [10] and hydrothermal method [17]. Also, well aligned (*c*-axis oriented) ZnO nanorods have been grown on ZnO/glass substrates by thermal evaporation method [18]. Reported Micro-Raman spectra of ZnO nanorods shows E_2(low), E_2(high), A_1(TO), E_1(LO) modes [17, 19] and nanowires shows E_2(high), A_1(LO), E_1(LO) modes [20]. ZnO nanorods shows PL emission at 380 nm (UV emission) and defect related emission in green-yellow region due to defect states such as oxygen vacancies, both zinc and oxygen interstitials etc [15]. ZnO nanowires shows UV emission at 385 nm, related to near band edge transition and defect related emission in the range of 420-600 nm originated from singly ionized oxygen vacancy [20]. PL peaks of ZnO at different wavelengths and their origin in details are listed [21] and discussed in Chapter 1.

In chapter 3, deposition was carried out for 20 minutes deposition time at various substrate temperatures. In this chapter, the deposition time was increased to 60 minutes in order to see the effect of deposition time on structural, optical as well as morphological properties of the nanostructures discussed in chapter 3. The effect of substrate temperature on the structural, optical properties of ZnO nanostructures is also discussed. Both rod- and wire-like structures with different dimensions at RT, 150 and 450^{0}C substrate temperatures, and only wire-like structures at 300 and 600^{0}C are observed.

4.2 Experimental details

ZnO nanostructures were deposited on Si (100) substrates by PLD set-up as discussed in Chapter 2 (Section 2.3). These nanostructures were deposited at (RT - 23), 150, 300, 450 and 600^{0}C for 60 minutes in presence of O_2 gas pressure of 0.1 mbar. Target-substrate

distance was fixed at 4 cm and laser fluence was around 12 J/cm^2. The structural, optical and morphological analysis of the nanostructures is done by XRD (seifert 3003-TT XRD), FE-SEM, PL and Micro-Raman spectroscopy.

4.3 Results and discussions

4.3.1 *X-ray diffraction analysis*

XRD spectra of the nanostructures were recorded by using a CuKα1 source at a wavelength of 1.5406A^o. Figure 4.1 shows the XRD of the nanostructures at substrate temperature ranging from RT to 600^{0}C with deposition time of 60 minutes. Various peaks are identified with the literature [22].

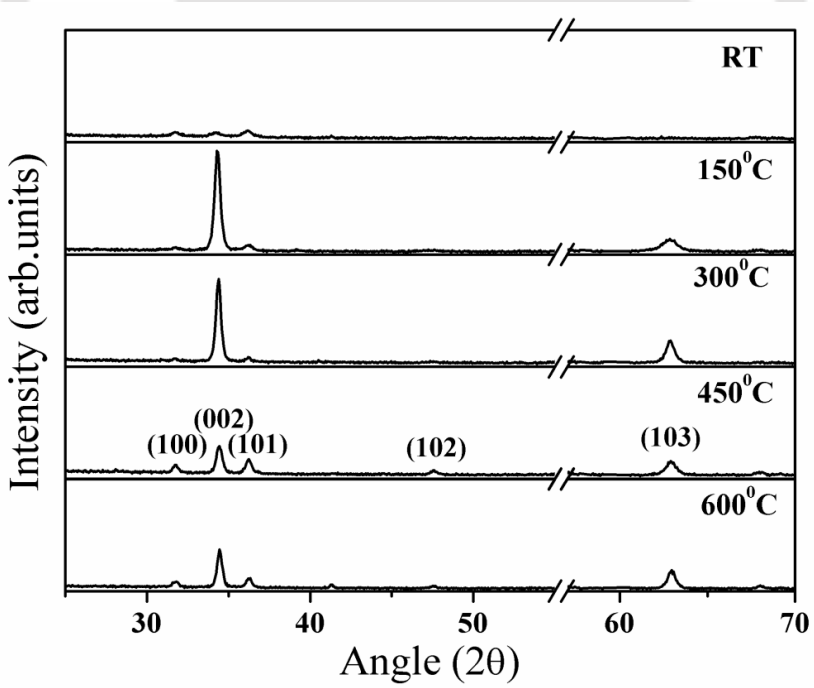

Figure 4.1: XRD of the nanostructures deposited at different substrate temperatures.

The intensity of (002) peak corresponding to 34.4^0 angle is relatively high compared to other peaks. The peaks indicate that the nanostructures have the wurtzite structure [23].

Nanostructures grown at 150 and 300^{0}C substrate temperatures are strongly *c*-axis oriented than that deposited at RT, 450 and 600^{0}C. For the nanostructures deposited at RT and 600^{0}C, the peak at 41.3^0 corresponds to zinc as shown in figure 4.1 [24]. Figure 4.2 is the expanded version of figure 4.1 showing the presence of weak peak corresponding to zinc. The presence of Zn indicates the deficiency of oxygen in the films. The fluence of the incident beam is much beyond the ablation threshold. Thus, the interaction of laser with ZnO will also result in the production of Zn. Since there is no surface mobility at RT on the substrate, some Zn is expected and hence its appearance in the XRD data.

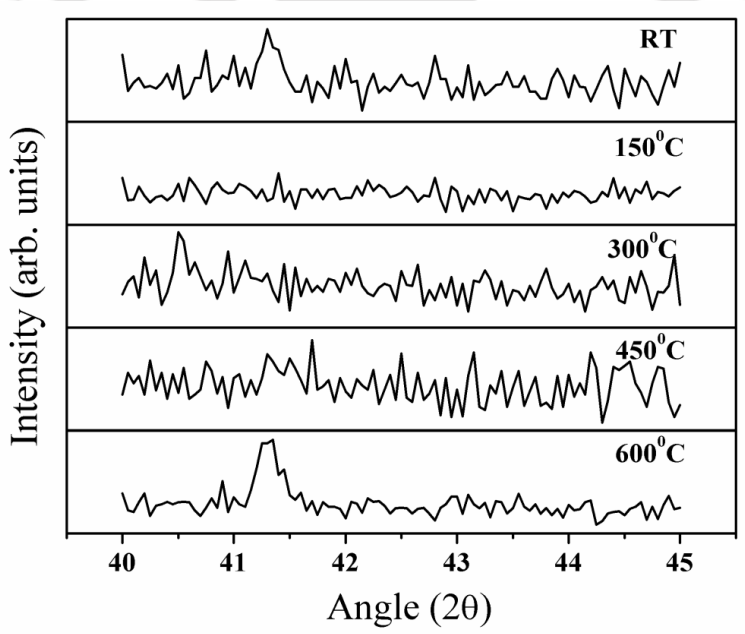

Figure 4.2: XRD of the deposited nanostructures showing the presence of Zn at different substrate temperatures.

At high temperature (600^{0}C), Zn will remain in the molten state. At other temperatures molten Zn in the plasma plume will readily combine with the surrounding oxygen to form ZnO.

The lattice spacing of the nanostructures is calculated by using the relation $(2d\sin\theta = n\lambda_x)$ where θ is the angle corresponding to (002) peak, d is lattice spacing and λ_x

is the wavelength of X-ray. The lattice spacing of bulk ZnO is 2.603 A^0 [25]. The lattice spacing deviates for the nanostructures grown at RT and 150^{0}C, whereas for others grown at elevated temperatures have values close to bulk ZnO. The deviation of lattice spacing from bulk value indicates the presence of stress and strain in the nanostructures grown at low substrate temperature. The values of lattice spacing, strain and stress with substrate temperature are given in table 4.1. Strain and stress [26] are calculated by using the eqns. (3.1) and (3.2). The sign in stress value indicates the nature of the stress whether it is tensile or compressive. It is observed that the stress is tensile [27] along *c*-axis in case of nanostructures grown at RT, 150 and 300^{0}C, whereas it is compressive along *c*-axis at 450 and 600^{0}C. Thus the nanostructures grown at high substrate temperatures are almost stress free in nature.

Table 4.1: Values of lattice spacing, strain and stress with substrate temperatures.

Substrate Temperature (^{0}C)	Lattice spacing (A^0)	Strain	Stress (GPa)
RT (23)	2.618	0.00587	-2.64
150	2.610	0.00281	-1.26
300	2.605	0.00077	-0.3466
450	2.602	-0.00024	0.1098
600	2.6	-0.00091	0.4135

The degree of crystal orientation is defined as $P = I(002)/\sum I(hkl)$, where $I(002)$ is the intensity of (002) diffraction peak and $\sum I(hkl)$ is the intensity of all diffraction peaks [28]. The variation of integrated intensity ratio $I(002)/I(101)$ and the FWHM of the (002) plane at 34.4^0 with the substrate temperature is shown in figure 4.3. It shows that this ratio increases from RT to 300^{0}C and then decreases gradually from 300^{0}C to 600^{0}C indicating that the

nanostructures grown at 150^{0}C and 300^{0}C are highly oriented along (002) direction and more so at 300^{0}C whereas no preferred orientation is observed for the nanostructures grown at other substrate temperatures. The FWHM is narrower for the nanostructures grown at 300^{0}C and 600^{0}C whereas it is broader at RT and in between at 150^{0}C and 450^{0}C. Narrower FWHM indicates better crystallinity. Other planes also showed similar behavior in FWHM.

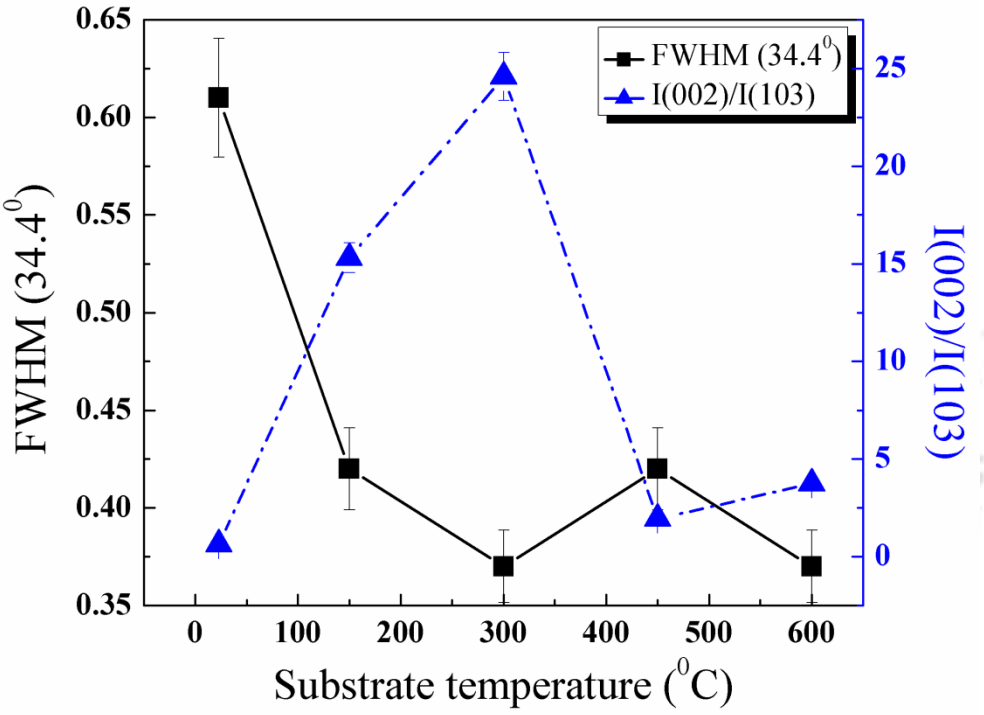

Figure 4.3: Variation of FWHM and intensity ratio of (002) and (103) peak of XRD with substrate temperatures.

4.3.2 *Surface morphology*

FE-SEM images of the deposited nanostructures are shown in figure 4.4. At RT, 150 and 450^{0}C substrate temperatures both the rod- and wire-like nanostructures are observed whereas at 300 and 600^{0}C only wire-like structures are observed. There are very few rod-like structures at RT. Such a distribution is attributed to the wide distribution of the size of nanoparticles deposited on the surface of the substrate that formed the nucleation sites for the

further growth of nanowires/rods as observed in this work described in previous chapter (chapter 3, section 3.3.2) on the deposition of ZnO nanostructures for 20 minutes under the same experimental conditions.

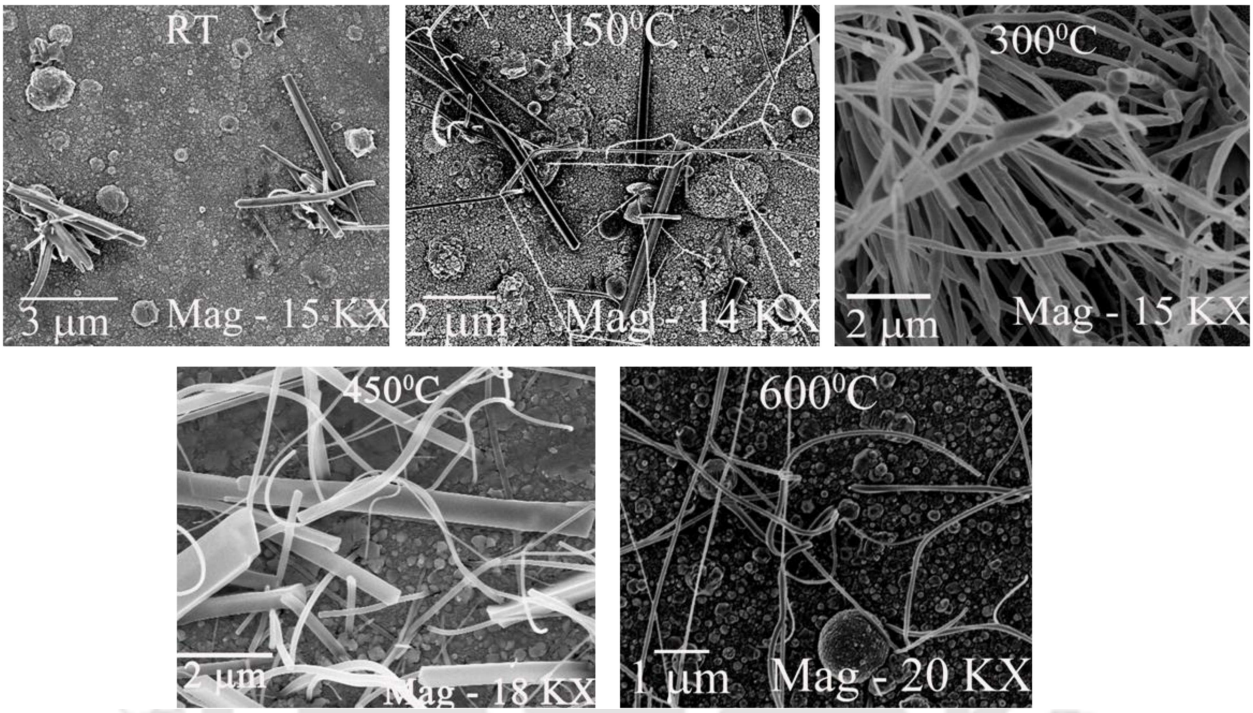

Figure 4.4: FE-SEM images of nanostructures deposited at different substrate temperatures.

Figure 3.2 (a-e) showed the formation of diamond-like structures on the surface apart from other particulates at 150 and 450^{0}C substrate temperatures, however, very smooth surfaces with nanoparticles were observed at 300 and 600^{0}C, respectively. The particles in the range of a few tens of nanometer have resulted in the growth of nanowires whereas those with larger size, a few hundreds of nanometers have resulted in the growth of nanorods. Very likely, a few of the nucleation sites with smaller dimension will merge in a way so as to favour the growth of nanorods (as observed at RT). Therefore, such surface morphologies have resulted in the growth of combination of rod- and wire-like or wire-like nanostructures. FWHM of (002) XRD peak, average size of nanorods and nanowires are given in table 4.2.

The FWHM (table 4.2) of (002) XRD peak changes with dimensions of the nanostructures. Only wire-like nanostructures show narrower FWHM whereas for the combination of rods- and wires-like structures it is broader. The FWHM of (002), (101) and (103) follows the same trend (figure 4.5) with the variation of substrate temperature.

Table 4.2: FWHM of (002) XRD peak, nanowire and nanorod diameters at different substrate temperatures.

Substrate temperature (^{0}C)	FWHM (002) (degree)	Nanowire diameter (nm)	Nanorod diameter (nm)
RT (23)	0.61	65	165
150	0.422	60	560
300	0.373	120	--
450	0.423	80	420
600	0.374	78	--

4.3.3 *Photoluminescence*

PL spectra of ZnO nanostructures at different substrate temperatures are shown in figure 4.6. Nanostructure deposited at RT have the near band-edge peak at 396 nm, at 150 and 450^{0}C, peak is at 397 nm, at 300^{0}C it is at 389 nm and at 600^{0}C, peak is at around 398 nm.

The PL emission in the range 388 – 395 nm is attributed to near band-edge emission and is observed for all the nanostructures. Only for the nanostructures deposited at 600^{0}C substrate temperature, a small peak is observed at 377 nm. This is due to the free exciton-exciton recombination near band-edge transition [29, 30]. A small intense peak in the blue-green region is also observed at 467 nm for all nanostructures. Reported PL peak at 468 nm peak is related to the defect levels such as surface defects and oxygen vacancy [31]. The

nanostructures grown at 300^{0}C show a low intense blue-green peak than the nanostructures grown at RT, 150, 450 and 600^{0}C indicating less defects for those grown at 300^{0}C.

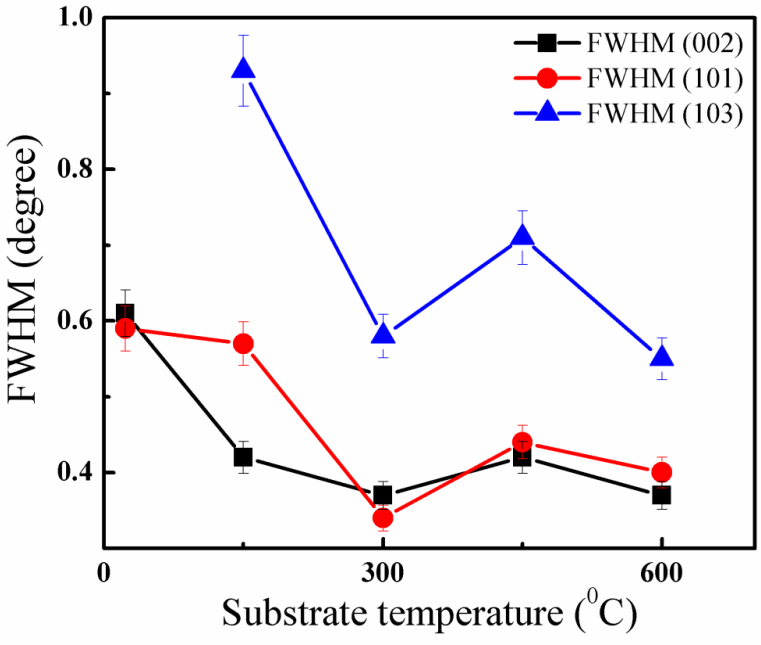

Figure 4.5: Variation of FWHM of (002), (101) and (103) XRD peaks at different substrate temperatures.

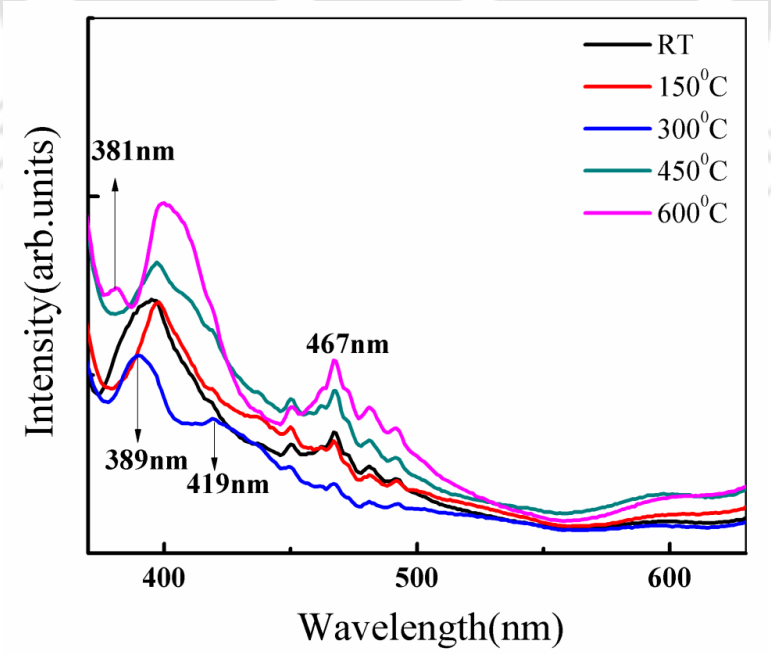

Figure 4.6: PL spectra of ZnO nanostructures deposited at different substrate temperatures.

Also, a broad peak in the yellow-red region is observed at around 595-602 nm. The peak at 600 nm is the yellow-red emission band and is due to the defects caused by deep levels [32]. It is clear that at substrate temperature of 450^0C, this peak is more prominent than the nanostructures deposited at other temperatures. The defect related emission comes due to the defect states present in ZnO such as states like oxygen/zinc vacancies, interstitial zinc/oxygen etc [21, 31-33]. The defects are minimum for the nanostructures grown at 300^0C substrate temperature. The Gaussian fitted PL peak positions in the range of 370 – 550 nm are given in table 4.3 and shown in figure 4.7.

The possible origin of PL peaks at different wavelengths in the range of 373-750 nm and that at 388 nm, 394 nm, 414-449 nm, 466 nm, 498-573 nm, 593 nm, 703 nm are discussed in literature [8, 21]. PL peak in the visible range (400-750 nm) is attributed to the deep level emission which is due to the defects like zinc or oxygen vacancies, antisite defects, interstitial zinc/oxygen etc [34].

Table 4.3: PL peaks at different substrate temperatures.

Substrate temperature (^{0}C)	**Location of PL peaks (nm)**
RT (23)	392, 425, 458
150	397, 424, 440, 467
300	388, 421, 445, 466
450	394, 418, 458,
600	375, 402, 467

PL peak at 419 nm is due to the defect related to interstitial oxygen [33] whereas at around 427 nm is from interstitial zinc [35]. PL emission in the range of 414 - 449 nm is due

to interstitial zinc defects [21]. PL peaks observed in the present work matches well with those reported in the literature [21].

PL spectra in the present work shows that the defects due to interstitial zinc or oxygen are present for all the nanostructures except at 600^{0}C. The defects due to interstitial zinc are more at RT and 150^{0}C. With the increase in temperature ambient oxygen reacts with ZnO plasma, the defects related to interstitial zinc diminishes, and defects related to interstitial oxygen appears. At 300^{0}C, a prominent PL peak related to interstitial oxygen defects is observed.

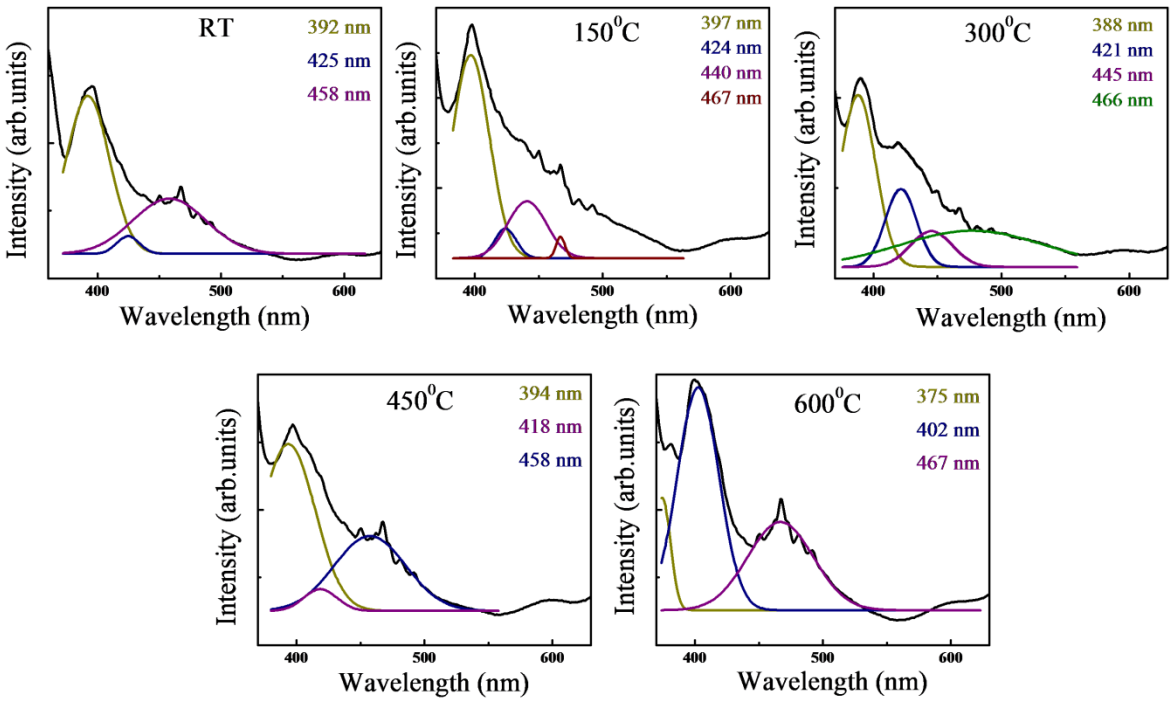

Figure 4.7: Gaussian fitted PL of the nanostructures deposited at different substrate temperatures.

4.3.4 *Micro-Raman analysis*

Micro-Raman spectra of the nanostructures recorded in the range of 200 – 900 cm^{-1} are shown in figure 4.8. The frequencies of the fundamental optical modes in bulk ZnO and ZnO nanostructures are summarized in table 4.4.

Three modes, namely, (E_2(high), E_1(TO) and A_1(LO)) are observed in the Raman spectra. E_2(high) peak is weak in intensity for the nanostructure deposited at RT, whereas the peak intensity increases continuously beyond RT till 600^{0}C. The presence of E_2(high) peak confirms the wurtzite structure of ZnO [36] and suggest that all the nanostructures except the nanostructure grown at RT are wurtzite in nature. E_2(high) peak at 438 cm^{-1} for all the nanostructures matches with the E_2(high) peak of ZnO nanorods [37]. E_1(TO) mode becomes prominent at RT but with the increase of substrate temperature, intensity of this mode diminishes and it vanishes at 600^{0}C substrate temperature. A_1(LO) mode is observed for all the grown nanostructures except that grown at 600^{0}C.

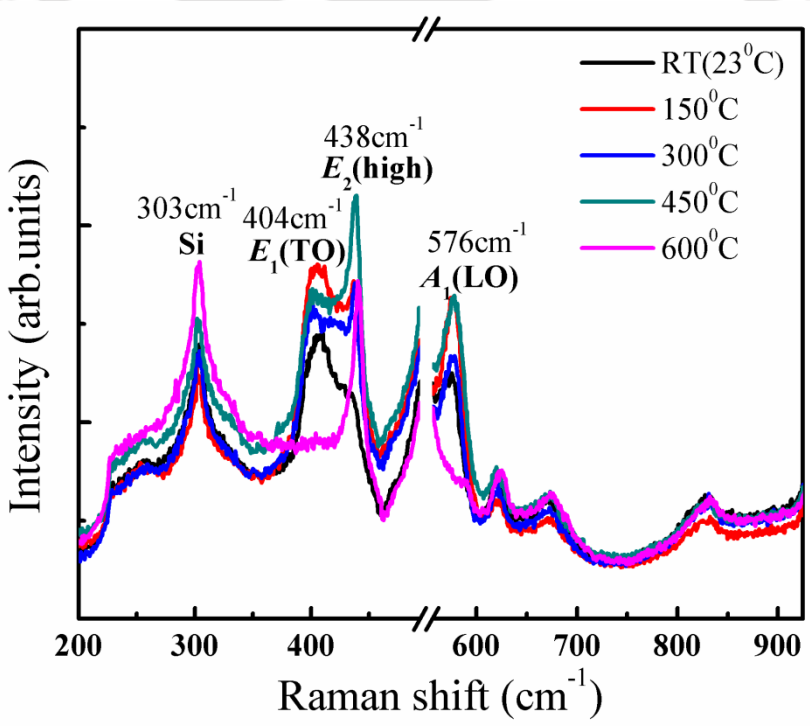

Figure 4.8: Micro-Raman spectra of ZnO nanostructures deposited at different substrate temperatures.

Micro-Raman spectra of ZnO nanorods and nanowires are reported [17, 19, 20]. The Raman mode positions and the width of E_2(high) mode for all the nanostructures in the present work are given in table 4.5. E_2(high) and E_1(TO) mode appears when incident light is

perpendicular to *c*-axis of ZnO and E_2, A_1(LO) mode appears only when incident light is parallel to the *c*-axis of wurzite ZnO [22]. As both E_1(TO) and A_1(LO) modes are present, the nanostructures are polycrystalline in nature as also observed in XRD results. Both A_1(LO) and E_1(TO) mode vanishes completely at 600^0C. A_1(LO) mode arises when the nanostructures are *c*-axis oriented [22] or from interstitial [38] defects present in ZnO.

Table 4.4: Raman modes of bulk ZnO and ZnO nanostructures deposited at different substrate temperatures.

	Multiphonon	A_1**(TO)**	E_1**(TO)**	E_2**(high)**	A_1**(LO)**	E_1**(LO)**
Bulk ZnO	334 cm^{-1} , 665 cm^{-1}	380 cm^{-1}	408 cm^{-1}	437 cm^{-1}		584 cm^{-1}
Present Work	667 cm^{-1}		404 cm^{-1}	438 cm^{-1}	576 cm^{-1}	

XRD spectra showed that at 600^0C substrate temperature, nanostructures are *c*-axis oriented though the intensity is weak. Also, from PL spectra, it is observed that the emission corresponding to interstitial defect (in the range of 415-430 nm) is absent only at 600^0C substrate temperature whereas this defect related emission is present at other substrate temperatures. So, the origin of A_1(LO) mode in Raman spectra is due to interstitial defects in the present work. The Lorentzian width of E_2(high) mode is given in table 4.5 and it is narrower at 300 and 600^0C as compared to others. Narrow width of E_2(high) mode is the indication of high crystal quality [39] and is consistent with XRD result.

The Raman peak at 303, 619 and 669 cm^{-1} is observed due to the multiphonon feature of silicon [40]. Shift in E_2(high) mode is the indication of the stress [41] in the nanostructures. E_2(high) mode is at 437 cm^{-1} for bulk ZnO and from table 4.4 and table 4.5, we observe that the stress in the nanostructures are less for 300 and 450^0C and is in accordance with XRD.

Table 4.5: Raman mode positions at different substrate temperatures.

Substrate Temperature (^{0}C)	Raman mode shift (cm^{-1})		
	E_1(TO)	E_2(high) & width	A_1(LO)
RT	407	435 (18.56)	570
150	404	436 (31.43)	573
300	401	438 (8.31)	573
450	401	438 (10.41)	574
600	-	439 (9.86)	-

4.4. Conclusions

ZnO nanowires, combination of ZnO nanorods and nanowires were successfully synthesized by PLD technique. XRD confirms the wurzite structure of ZnO and the growth of almost stress free nanostructures at 300 and 450^{0}C substrate temperature. FWHM of (002) XRD peak is narrower at 300 and 600^{0}C. FE-SEM images show the growth of nanowires alone at 300 and 600^{0}C, whereas combination of nanorods and nanowires at other substrate temperatures. PL of the nanostructures shows that the emission occurs from both the near band edge as well as deep levels. Deep levels are the defects related to vacancies, interstitial and antisite sites in the ZnO nanostructures. Micro-Raman spectra of the nanostructures confirm the wurtzite nature of nanostructures. Width of E_2(high) mode of Raman spectra is narrower at 300 and 600^{0}C. XRD, Raman and FE-SEM analysis indicates that for nanowires, FWHM of XRD peak as well as width of E_2(high) mode is narrower.

Bibliography

1. M. H. Huang, S. Mao, H. Feick, H. Yan, Y. Wu, H. Kind, E. Weber, R. Russo, P. Yang, Science, 292 (2001) 1897.
2. Y. Zhang, M. K. Ram, E. K. Stefanakos, D. Y. Goswami, J. Nanomaterials, 2012, 624520 (22 pages).
3. E. Lai, W. Kim, P. Yang, Nano Res, 1 (2008) 123.
4. L. Guo, H. Zhang, D. Zhao, B. Li, Z. Zhang, M. Jiang, D. Shen, Sensors and Actuators B, 166-167 (2012) 12.
5. Z. fan, D. wang, P. C. Chang, W-Y. Tseng, J. G. Lu, Appl. Phys. Lett. 85 (2004) 5923.
6. Z. L. Wang, J. Song, Science, 312 (2006) 242.
7. G. C. Yi, C. Wang, W. I Park, Semicond. Sci. Technol. 20 (2005) s22.
8. A. B. Djuristic, A. M. C. Ng, X. Y. Chen, Progress in quantum Electronics, 34 (2010) 191.
9. S. Baruah and J. Dutta, Sci. Technol. Adv. Mater. 10 (2009) 013001-1.
10. N. Boukos, C. Chandrinou, K. Giannakopoulos, G. Pistolis, A. Travlos, Appl. Phys. A, 88 (2007) 35.
11. S. Choopun, H. Tabata, T. Kawai, J. Cryst. Growth, 274 (2005) 167.
12. H. Ham, G. Shen , J. H. Cho, T. J. Lee, S. H. Seo, C. J. Lee, Chem. Phys. Lett, 404 (2005) 69.
13. A. Rahm, M. Lorenz, T. Nobis, G. Zimmermann, M. Grundmann, B. Fuhrmann, F. Syrowatka, Appl. Phys. A, 88 (2007) 31.
14. H. Wan, H. E. Ruda, J. Mater. Sci: Mater Electron, 21 (2010) 1014.
15. Y. Sun, G. M. Fuge, M. N. R. Ashfold, Superlattices and Microstructures, 39 (2006) 33.

16. M. R. Khanlary, V. Vahedi, A. Reyhani, Molecules, 17 (2012) 5021.

17. D. Polsongkram, P. Chamninok, S. Pukird, L. Chow, O. Lupan, G. Chai, H. Khallaf, S. Park, A. Schulte, Physica B, 403 (2008) 3713.

18. A. Umar, C. Ribeiro, A. Al-Hajry, Y. Masuda, Y. B. Hahn, J. Phys. Chem. C. 113 (2009) 14715.

19. N. Ekthammathat, T. Thongtem, A. Phuruangrat, S. Thongtem, J. Nanomaterials, 2013, Article ID. 208230 (4 pages).

20. L. L. Yang, J. H. Yang, D. D. Wang, Y. J. Zhang, Y. X. Wang, H. L. Liu, H. G. Fan, J. H. Lang, Physica E, 40 (2008) 920.

21. G. Patwari, B. J. Bodo, R. Singha, P. K. Kalita, Research Journal of Chemical Sciences, 3 (2013) 45.

22. R. Zhang, P. G. Yin, N. Wang, L. Gou, Solid State Sci. 11 (2009) 865.

23. P. S. Kumar, A. D. Raj, D. Mangalaraj, D. Nataraj, Appl. Surf. Sci. 255 (2008) 2382.

24. S. Cho, J. Ma, Y. Kim, Yi. Sun, G. K. L. Wong, J. B. Ketterson, Appl. Phys. Lett. 75 (1999) 2761.

25. J. Zhao, L. Hu, Z. Wang, J. Sun, Z. Wang, Appl. Surf. Sci. 253 (2006) 841.

26. A. Ismail, M. J. Abdullah, Journal of King Saud University-Science 25 (2013) 209.

27. R. J. Lad, P. D. Funkenbusch, C. R. Aita, J. Vac. Sci. Technol, 17 (1980) 808.

28. A. Mohanto, R. K. Thereja, J. Appl. Phys. 104 (2008) 044906-1.

29. Ye. Sun, G. M. Fuge, M. N. R. Ashfold, Chem. Phys. Lett. 396 (2004) 21.

30. S. Chakraborty and P. Kumbhakar, Materials Letters 100 (2013) 40.

31. Y. H. Yang, Y. Feng, G. W. Yang, Appl. Phys. A. 102 (2011) 319.

32. J. Dai, C. X. Xu, Z.L. Shi, R. Ding, J.Y. Guo, Z. H. Li, B. X. Gu, P. Wu, Opt. Mater. 33 (2011) 288.

33. S. Vempati, J. Mitra, P. Dawson, Nanoscale Res. Let. 7 (2012) 470.

34. M. Willander, O. Nur, J. R. Sadaf, M. I. Qadir, S. Zaman, A. Zainelabdin, N. Bano, I. Hussian, Materials, 3 (2010) 2643.

35. A. B. Djurisic, W. C. H. Choy, V. A. L. Roy, Y. H. Leung, C. Y. Kwong, K. W. Cheah, T. K. G. Rao, W. K. Chan, H. F. Lui, C. Surya, Advanced Functional Materials, 14 (2004) 856.

36. S. K. Panda, C. Jacob, Appl. Phys. A 96 (2009) 805.

37. R. Vinodkumar, I. Navas, N. V. Unnikrishnan, V. P. Mahadevan Pillai, Optoelectronics and Advanced Materials-Rapid Commun. 6 (2012) 411.

38. G. J. Exarhos, S. K. Sharma, Thin Solid Films, 270 (1995) 27.

39. F. Guell, J. O. Osso, A. R. Goni, A. Cornet, J. R. Morante, Superlattices and Microstructures, 45 (2009) 271.

40. B. Yang, A. Kumar, P. Feng, R. S. Katiyar, Appl. Phys. Lett. 92 (2008) 233112.

41. S. B. Yahia, L. Znaidi, A. Kanaev, J. P. Petitet, Spectrochimica Acta Part A 71 (2008) 1234.

Chapter 5

Pulsed laser deposited flower-shaped ZnO nanostructures and their characterization

5.1 Introduction

Synthesis of ZnO nanoflowers are reported using several techniques such as hydrothermal route on copper substrate [1], microwave irradiation technique [2], two step method involving the growth of ZnO seed layer on polystyrene sphere by PLD and followed further growth of nanoflowers consisting of nanowires on seed layer by hydrothermal method [3], solution process at low temperature [4], wet-chemical method [5], microwave hydrothermal technique [6] etc. Flower-shaped nanostructures have been obtained by combination of nanorods [2, 4], nanowires [3], nanosheets [1, 5], and are polycrystalline [1, 2, 4] in nature. UV-visible emission spectrum shows absorption at around 399 nm [2] from flower-shaped ZnO nanostructures. PL spectra of flower-shaped ZnO nanostructures showed near band-edge emission at 380 nm and visible emission at 515 nm [4]. Raman spectra of flower-shaped nanostructures showed various Raman modes, namely, E_2(high), A_1(TO), A_1(LO), E_1(TO), E_1(LO) modes [2, 4, 6, 7]. Despite various optical applications, flower-shaped nanostructures also show photocatalytic applications [5, 8], gas sensitivity [7] etc.

The effect of substrate temperature on ZnO thin films grown by PLD [9], radio frequency magnetron sputtering [10], atmospheric pressure metalorganic chemical vapor deposition [11] etc. has been reported. With the annealing of nanostructures small size grains sintered with each other and formed large sized grains [12]. The morphology changed a lot as the films become textured with the increase in substrate temperature [11].

In chapter 4, deposition was carried out at 0.1 mbar O_2 pressure at various substrate temperatures. In the present chapter, oxygen pressure was reduced from 0.1 mbar to 0.05 mbar in order to see the effect of oxygen pressure on structural, optical as well as morphological properties of the nanorods and wires. The effect of substrate temperature on the structural, optical and morphological properties on ZnO nanostructures is also studied.

5.2 Experimental details

ZnO nanostructures were deposited on silicon (100) substrates by PLD set-up discussed in chapter 2 (Section 2.3). These nanostructures were deposited at RT, 150, 300, 450, 600 and 750^{0}C for 60 minutes in presence of O_2 gas pressure of 0.05 mbar. Target-substrate distance was fixed at 4 cm and laser fluence was around 12 J/cm^2 under the base pressure of 10^{-5} mbar. Nanostructures were characterized by XRD (Rigaku TTRAX III), FE-SEM, PL and Micro-Raman spectroscopy.

5.3 Results and discussions

5.3.1 *X-ray diffraction analysis*

XRD of the ZnO nanostructures is shown in figure 5.1. It predominately shows (002) peak, indicating the wurtzite nature of the nanostructures.

Increase in substrate temperature shows the presence of less intense ZnO peaks (very less intense) corresponding to (100), (002), (101), (102), (110) and (103) planes along with the (002) peak. The intensity of (002) peak increases with the increase in substrate temperature up to 600^{0}C and then decreases at 750^{0}C. The variation of FWHM of the (002) XRD peak with substrate temperature of the nanostructures is shown in figure 5.2. It shows that the FWHM decreases at 150^{0}C and then increases at 300^{0}C and 450^{0}C, again decreases with the

increase in substrate temperature. Film is almost crystalline at 150 and 300 ^{0}C but tends to polycrystalline nature at or beyond 450^{0}C. This is due to high surface mobility at reduced pressure where the atoms will be knocked-out from the preferred lattice sites.

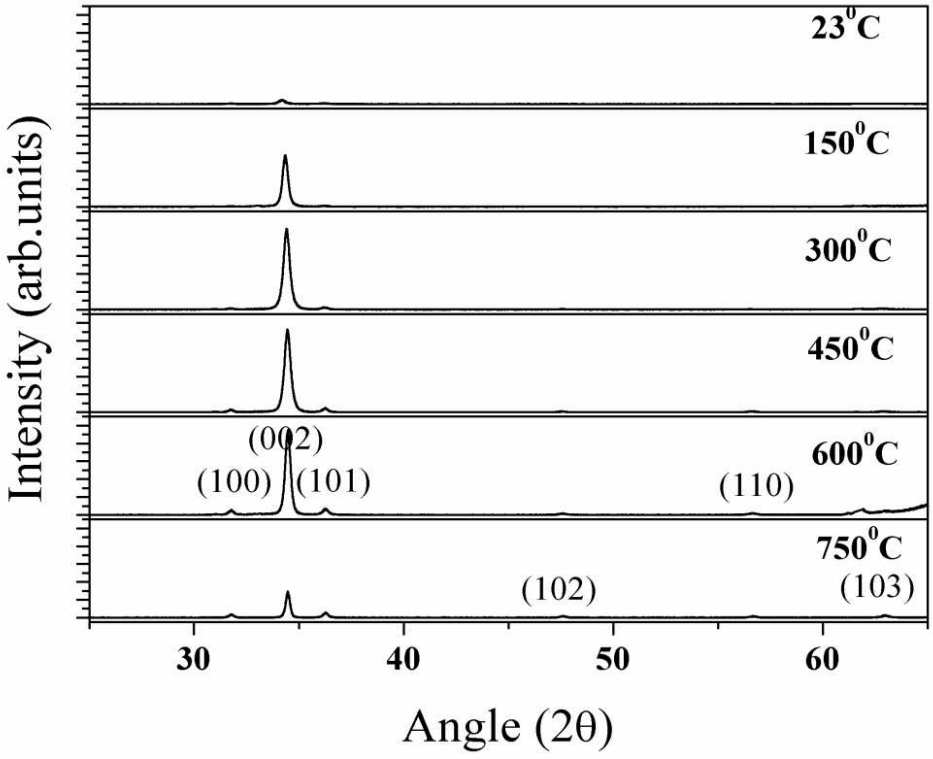

Figure 5.1: XRD spectra of ZnO nanostructures deposited at different substrate temperatures.

The lower value of FWHM indicates the high crystallinity of the nanostructures [13, 14]. Therefore, the crystallinity is better for the nanostructures grown at 750^{0}C as compared to that at other substrate temperatures. This shows an improvement in the crystallinity of the nanostructures with the increase in substrate temperature. The grain size calculated using Debye Scherrer's formula is given by [14]

$$D = \frac{0.9\lambda}{\beta \cos\theta} \tag{5.1}$$

and its variation with temperature is shown in figure 5.3. The lattice spacing is calculated and its variation with temperature is shown in figure 5.3.

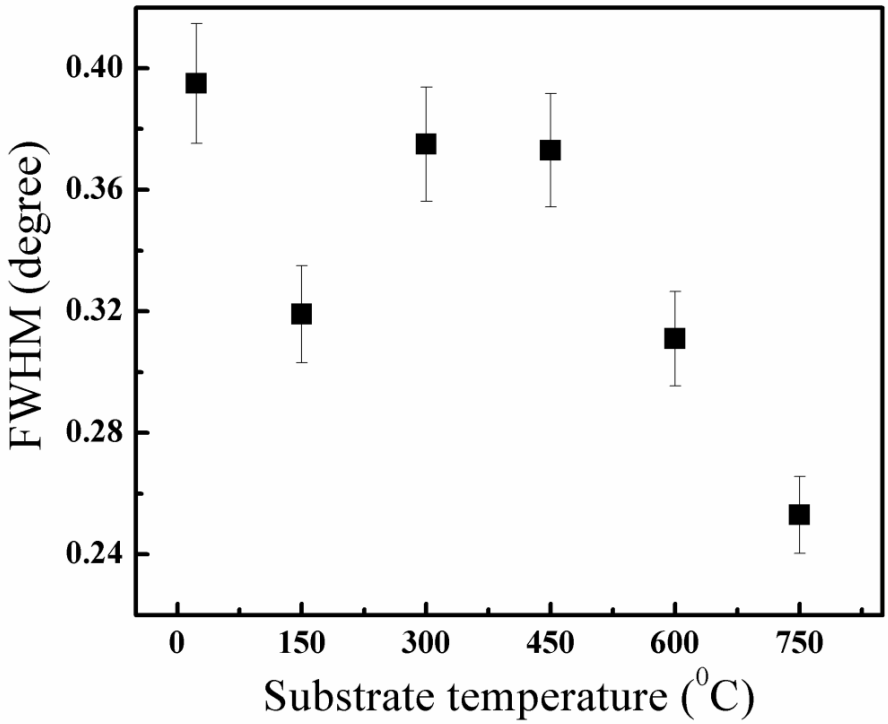

Figure 5.2: Variation of FWHM of (002) XRD peak of the nanostructures with substrate temperature.

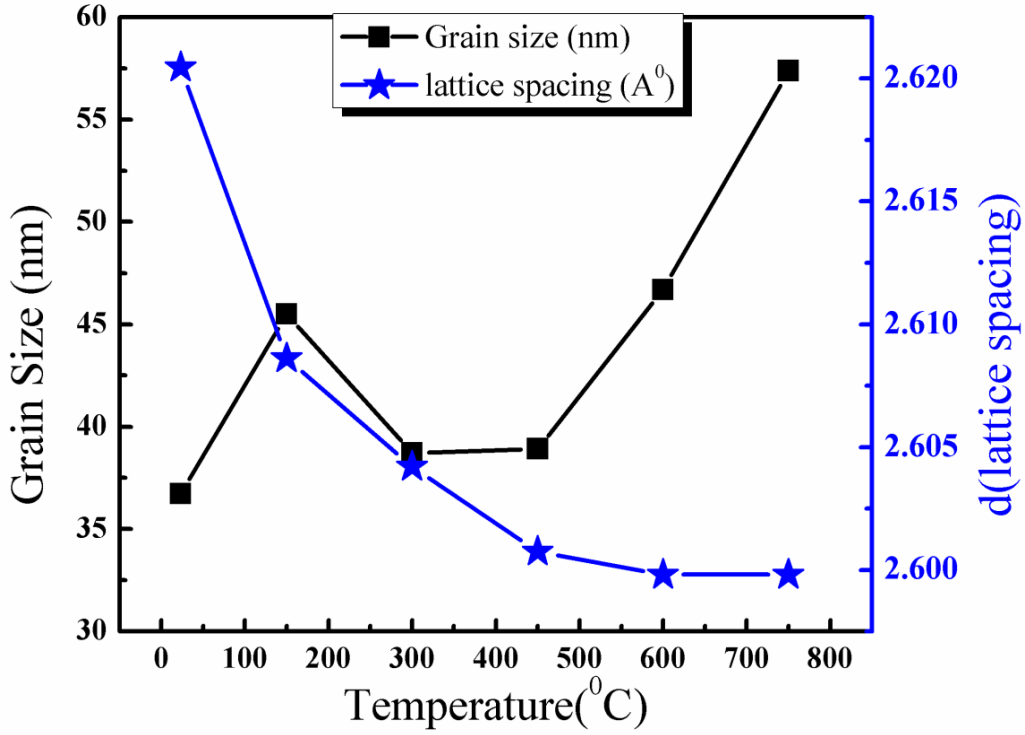

Figure 5.3: Variation of grain size and lattice spacing calculated from XRD peak of the nanostructures with substrate temperature.

The lattice spacing is found to be more at RT and decreases gradually with the increase in substrate temperature. The lattice spacing of bulk ZnO is 2.603 A^0. Figure 5.3 indicates that there is a release in stress as the substrate temperature increases. The strain and stress value are calculated by using the eqns. (3.1) and (3.2) and are given in table 5.1. The values of lattice spacing and the grain size are also given in table 5.1. The nanostructures grown at RT has a stress value of 3.02 GPa which is largest as compared to other nanostructures deposited at higher temperature.

Table 5.1: Table of lattice spacing, strain, stress and grain size of the nanostructures at different substrate temperatures.

Substrate temperature (^{0}C)	**Lattice spacing (A^0)**	**Strain ($\times10^{-3}$)**	**Stress (GPa)**	**Grain Size (nm)**
RT (23)	2.620	6.72	-3.02	36.72
150	2.608	1.92	-0.86	45.49
300	2.604	0.38	-0.17	38.70
450	2.600	-1.15	0.51	38.91
600	2.600	-1.53	0.67	46.67
750	2.600	-1.53	0.67	57.38

The stress has the lowest value for the nanostructures grown at 300^{0}C because the lattice spacing is close to that of bulk ZnO. Also, there is a change in sign in stress value (substrate temperature change of 300^{0}C to 450^{0}C) and the sign is the indication of whether the stress is compressive or tensile [15]. The sample grown at 300^{0}C is almost stress free [15]. With the increase in substrate temperature beyond 300^{0}C, there is a compression in the normal lattice of ZnO. Stress in ZnO films comes from both the extrinsic stress and intrinsic

stress [16]. Intrinsic stress is due to the impurities, defects and lattice distortions whereas extrinsic stress is due to lattice mismatch and lattice thermal expansion coefficient mismatch.

At low substrate temperature, thin films become amorphous in nature [9] and shows polycrystalline nature [11] but with the increase in substrate temperature, film become crystalline [9, 11]. With further increase in substrate temperature, films tend to polycrystalline in nature [10]. Flower-shaped structures reported in literature [1, 2, 4] show polycrystallinity. In this work, with the increase in substrate temperature, a few flower-shaped nanostructures along with nanoparticles were observed [Section 5.3.2].

5.3.2 *Surface morphology*

Surface morphology of the nanostructures was recorded by FE-SEM images as shown in figure 5.4. Surface morphology changes a lot with the change of substrate temperature [9, 11]. With the increase in substrate temperature, surface mobility of the deposited particles increase and distribution of the particles on the surface becomes uniform, resulting in good crystalline particles. But, at high substrate temperature, because of high kinetic energy, collision occurs and because of re-evaporation, surface gets rough and the crystallinity degrades.

At RT, particles formed are smaller in size At 150^0C, some of small particles coalesce and form large particles. At 150^0C, grain boundaries are observed between the larger particles that consists of small sized particles as shown in FE-SEM images. As we move to 300^0C, larger particles are observed with distinct grain boundaries and particles. Such a transformation from RT to 300^0C is obvious because, with the increase in substrate temperature, surface mobility increases and the particles distribute on the surface as the particles try to move in the lowest energy sites [9, 10].

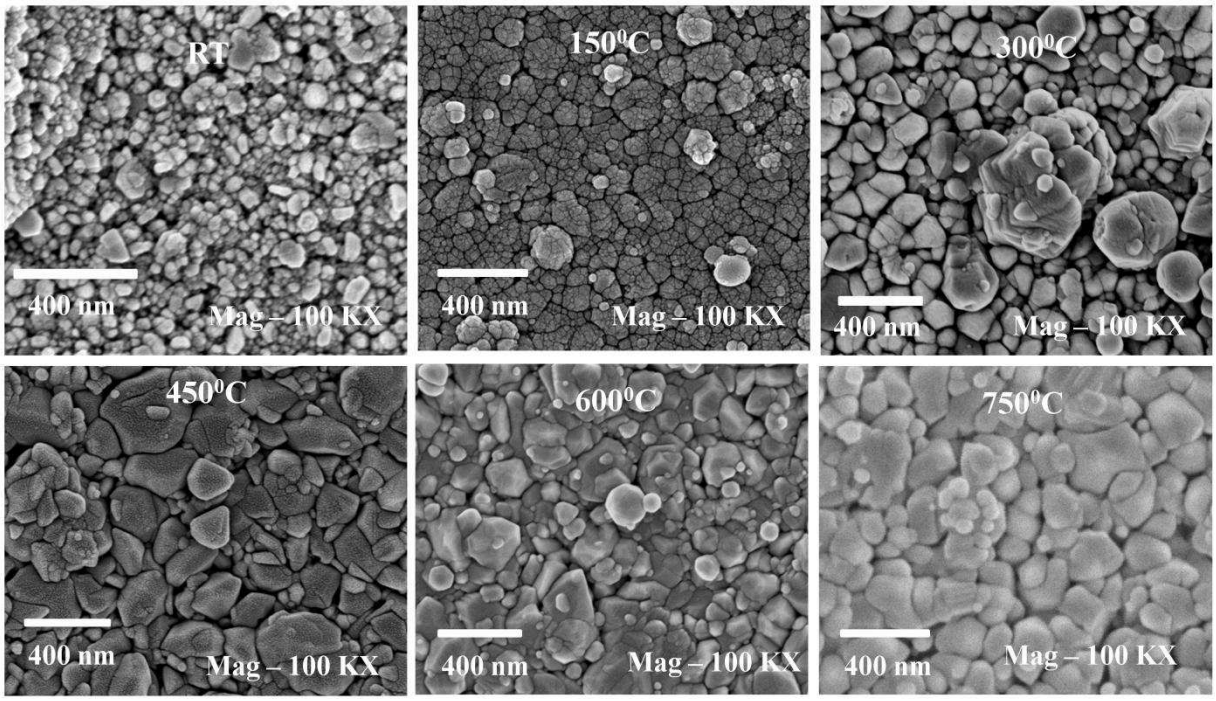

Figure 5.4: FE-SEM images of the nanostructures at different substrate temperatures.

Increasing temperature allows the nanoparticles to sinter and form large particles [12]. This transformation is very clear from RT to 300^{0}C in the present experiment as well. Small size nanoparticles (at RT) start to sinter with each other and try to form large size particles at 150^{0}C. At 300^{0}C, nanoparticles sinter completely and form distinct and large size particles. With the increase in substrate temperature, particles with *c*-axis orientation increase and become more crystalline. At 150^{0}C, FWHM of (002) peak decreases suddenly from RT and again increases at 300^{0}C. The grain boundaries at 150^{0}C are large as observed from FE-SEM images. Hence, in XRD spectra, decrease in FWHM at 150^{0}C is observed. At 450^{0}C, some diamond shaped particles with hexagonal top faced surface are present and at 600^{0}C, particles are distinct and some are hexagonal in shape as shown in FE-SEM images. Further increase in substrate temperature result in highly crystalline particles with strong (002) orientation. At 750^{0}C, distinct paricles are observed. Less intense (002) peak indicate that the number of

particles with *c*-axis orientation is less. This is because at very high substrate temperature, particles re-evaporate from the surface.

As shown in figure 5.5, at RT some of the particles agglomerate scatterly on the surface as there is no added energy to the surface atoms and hence the agglomerated particles do not get any particular shape. At 150^{0}C, the agglomeration of the particles still occur but the shape of the agglomerated particles tend to a shape of flower-shaped nanostructures and each petal consist of small distinct particles as shown from FE-SEM images.

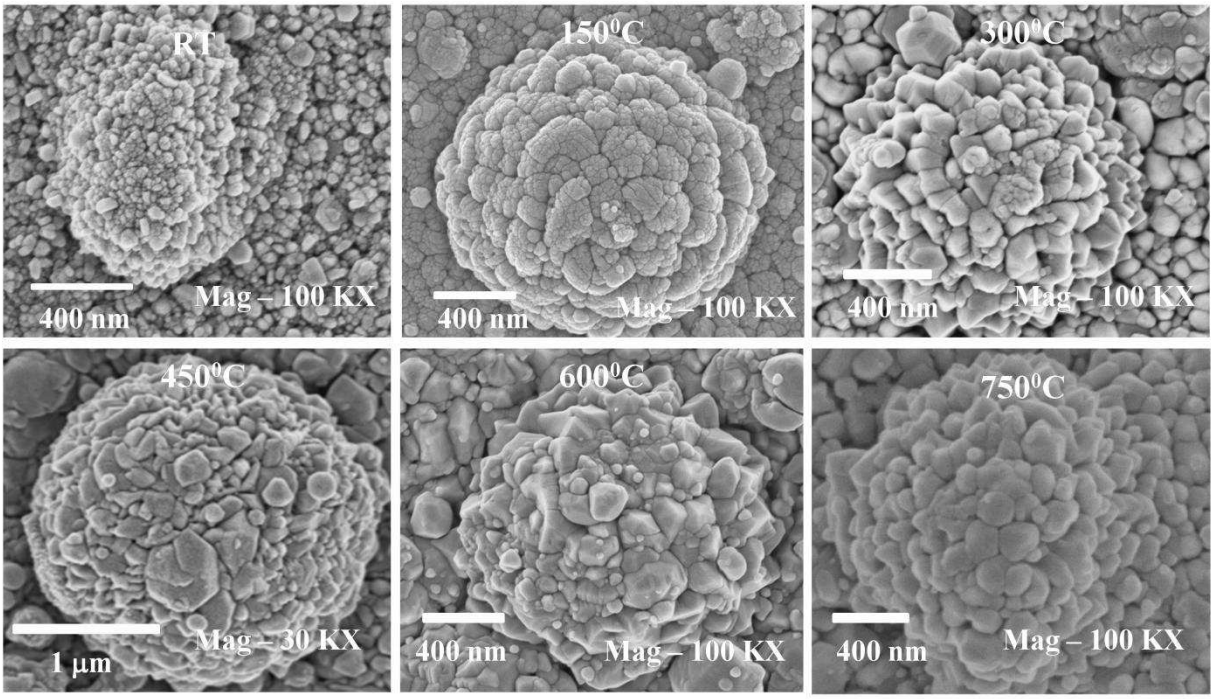

Figure 5.5: FE-SEM images of the flower-shaped nanostructures at different substrate temperatures.

The reason is that some energy is added to the surface atoms and the atoms try to move on to the thermodynamically favorable sites and tends to attain a particular shape. At 300^{0}C, also the agglomeration of the distinct particles tends to the shape of a flower-shaped nanostructures and the density of particle forming the flower-shaped structures is less as

compared to that at RT and 150^{0}C. At higher substrate temperatures, there is no such change in flower-shaped structures whereas the density of particles forming the flower-shaped structures decreases with the increase in substrate temperature.

5.3.3 *Photoluminescence*

PL spectra of the nanostructures are shown in figure 5.6. The Gaussian fitted (figure 5.7) PL peaks at various substrate temperatures are shown in table 5.2. The nanostructures grown at RT and 150^{0}C have a distinct peak at around 380 nm whereas for others grown at elevated temperatures have a weak shoulder at 380 nm. Nanostructures other than at RT and 150^{0}C showed near band edge emissions in the range of 393 - 398 nm. The peaks at 380 and 382 nm are observed for the nanostructures at RT and 150^{0}C. The PL peaks in the range of 380-400 nm are attributed to near band edge emission [17-19]. Wide peak at 404 nm observed for the nanostructures grown at RT and 150^{0}C is due to the transitions from zinc interstitial to zinc vacancy [20].

Other PL peaks are identified from the literature [21, 22]. The peaks in the range of 400 - 750 nm are the visible emission in the blue-green-yellow region that results from the defects such as zinc and oxygen vacancies, interstitial zinc and oxygen, antisite zinc and oxygen [22 - 25] etc. as also identified in the present work. Blue green emissions centered at 415, 440 and 470 nm [26] and 420, 440, 486, 573 nm are reported in the literature [27]. Blue emission at 467 nm observed for the nanostructures at 450^{0}C is attributed to the defect states such as surface defects and oxygen vacancies [25] and zinc vacancy [23]. Figure 5.7 shows that the emission from the interstitial zinc defect is more for the nanostructures grown at RT and 150^{0}C. Emissions beyond 500 nm are from the oxygen vacancies. The oxygen vacancies are not observed in all nanostructures and are due to the fact that the nanostructures are free from the defects coming from oxygen vacancies.

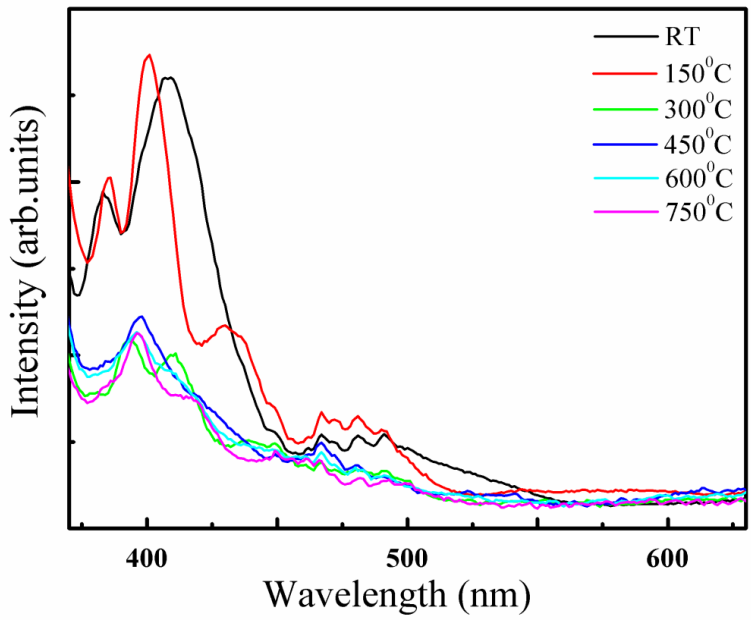

Figure 5.6: PL spectra of the nanostructures deposited at different substrate temperatures.

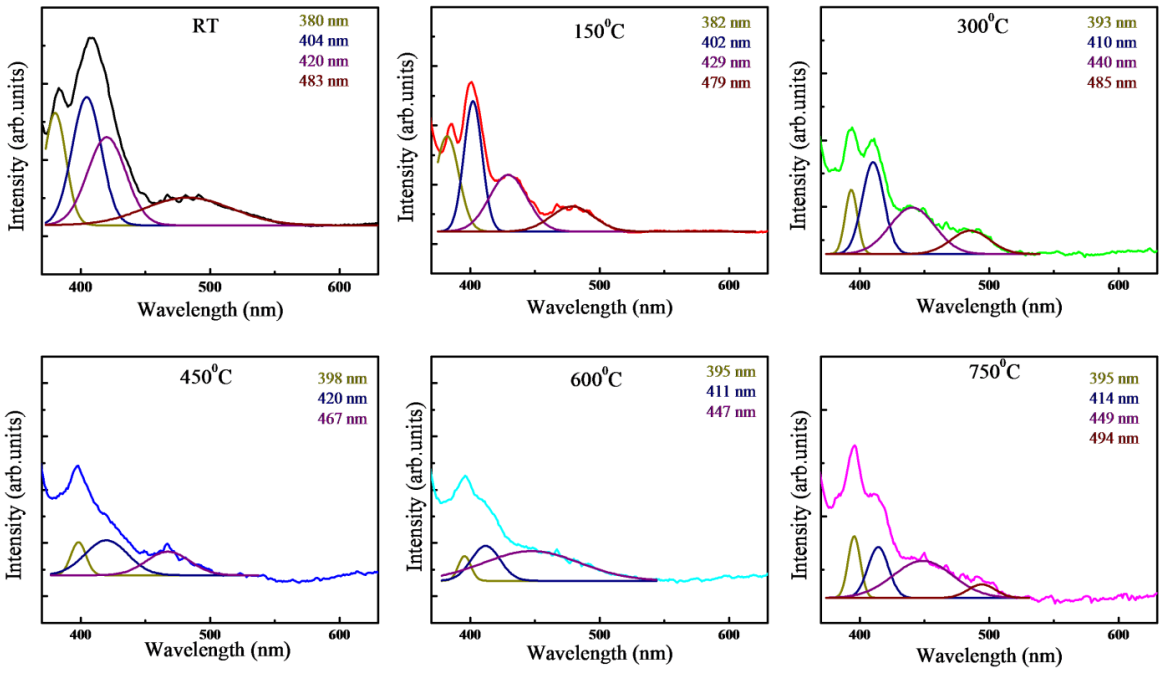

Figure 5.7: Gaussian fitted PL peaks of the nanostructures deposited at different substrate temperatures.

PL spectra shows that the nanostructures have low defects as the intensity of defect related emissions are low as compared to the near band edge emission. ZnO nanoflowers

reported in [6] have PL emission at 402, 425, 560 nm, and emissions at 373, 429, 482 and 521 nm as reported in [28]. PL peaks of ZnO nanoparticles reported in [29] are at 396, 416, 445, 481 and 524 nm. Almost all of these PL peaks are observed in the nanostructures and are given in table 5.2.

Table 5.2: Gaussian fitted PL peaks of the nanostructures at different substrate temperatures.

Substrate temperature (^{0}C)	PL peak positions (nm)
23	380, 404, 420, 483
150	382, 402, 429, 479
300	393, 410, 440, 485
450	398, 420, 467
600	395, 411, 447
750	395, 414, 449, 494

5.3.4 *Micro-Raman analysis*

Micro-Raman spectra of the nanostructures are shown in figure 5.8. where E_2(low) and E_2(high) mode shows strong dependence on substrate temperature. Other two modes, (E_1(TO) at 407 cm^{-1}and A_1(LO) at 574 cm^{-1} [27] are observed at low substrate temperature (RT to 450^{0}C) whereas they vanish completely at high substrate temperatures (600 and 750^{0}C).

The variation of FWHM of Lorentzian fitted E_2(high) mode with temperature is shown in figure 5.9 and it is observed that the FWHM decreases with the increase in substrate temperature.

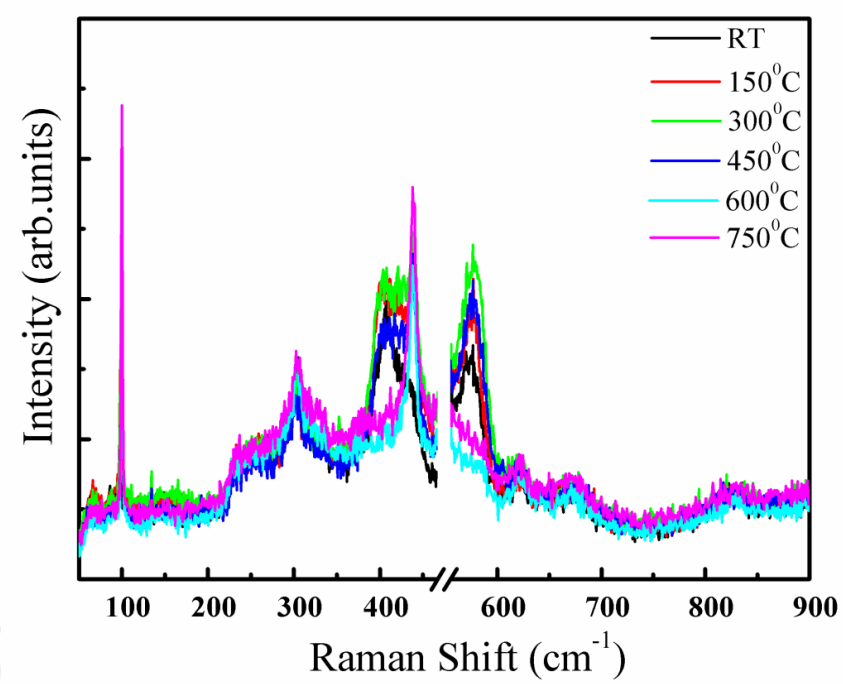

Figure 5.8: Micro-Raman spectra of the nanostructures deposited at different substrate temperatures.

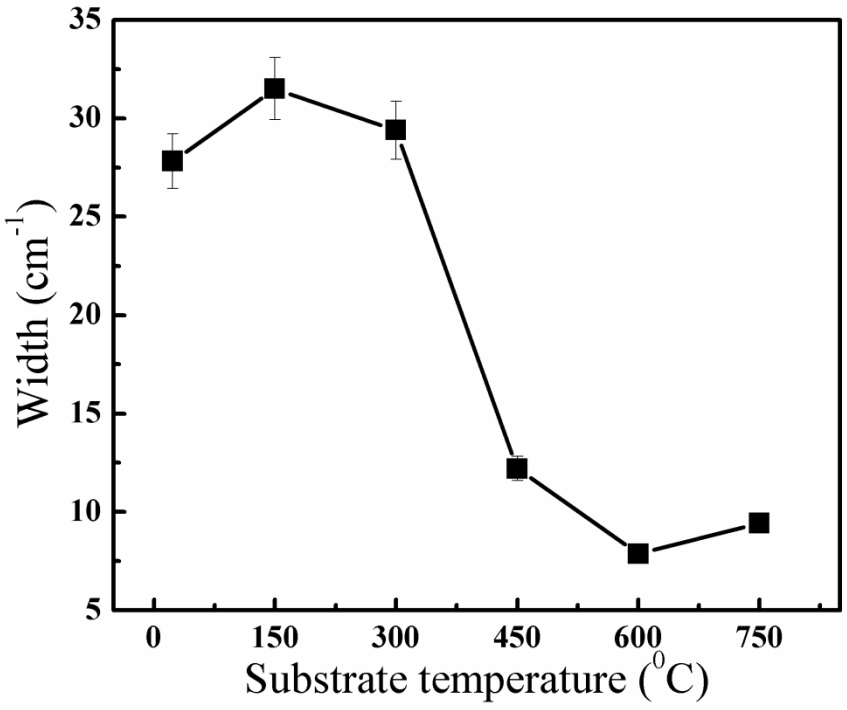

Figure 5.9: Variation of the width of E_2(high) mode with substrate temperature.

The high intensity and narrowing of the peak indicates the good crystal quality [30] of the nanostructures and supports the XRD results. Also, it is observed that E_1(TO) mode vanishes gradually with the increase in substrate temperature and A_1(LO) mode increases gradually upto 300^0C and decreases at 450^0C and vanishes completely at higher substrate temperatures. The Raman mode position of all the nanostructures and its deviation from the reported values [31] are listed in table 5.3. Raman modes of the flower-shaped nanostructures are observed i.e., E_2(high) at 437 cm^{-1} [4], 439 cm^{-1} [2], 438 cm^{-1} [6, 7], A_1(TO) at 381 cm^{-1} [4], 386 cm^{-1} [2], 383 cm^{-1} [6], 380 cm^{-1} [7], E_1(LO) at 582 cm^{-1} [4], 583 cm^{-1} [2], E_1(TO) at 410 cm^{-1} [6], 409 cm^{-1} [7], A_1(LO) at 574 cm^{-1} [6] etc. Reported Raman modes of ZnO nanoparticles are at 436 cm^{-1} (E_2(high) mode), 574 cm^{-1} (A_1(LO) mode) [10].

It is argued that A_1(LO) mode may arise due to the point defects [32] or in case of highly oriented ZnO nanostructures, where incident light falls exactly normal to the surface [31]. XRD data showed that the nanostructures have high (002) orientation upto 300^0C substrate temperature, whereas other peaks of ZnO also appear with the increase in substrate temperature. However A_1(LO) mode is not observed at higher substrate temperatures whereas nanostructures show (002) XRD peak. So, the contribution of A_1(LO) mode may arise from the defects related to oxygen vacancy [33] or interstitial zinc [34] as these defect related emissions are observed in PL spectra. PL peak is observed at around 420 nm for the nanostructures grown at substrate temperature from RT to 450^0C, whereas PL peak shifts to around 411 nm at substrate temperatures of 600^0C and 750^0C. PL peak at 420 nm originates from zinc interstitials defects. So, A_1(LO) mode (related to interstitial zinc) is observed at low substrate temperatures. With the increase in substrate temperature, excess Zn gets oxidized and oxygen defects get reduced. So, A_1(LO) mode vanish at higher substrate temperatures and PL peak at 411 nm that originates due to interstitial oxygen defect is observed. The peak at 303, 619 and 669 cm^{-1} arises due to the silicon substrate [35].

Table 5.3: Table of Raman mode positions and its deviation from reported values of the nanostructures.

Symmetry	Theory	RT	150^{0}C	300^{0}C	450^{0}C	600^{0}C	750^{0}C
E_2(low)	101		98.5 (-2.5)	99.2 (-1.8)	99.8 (-1.2)	99.9 (-1.1)	99.9 (-1.1)
E_1(TO)	407	407	404.8 (-2.2)	405.2 (-1.8)			
E_2(high)	437	436 (-1.0)	436 (-1.0)	436.9 (-0.1)	438.08 (+1.08)	438.22 (+1.22)	438.33 (+1.33)
A_1(LO)	574	570 (-4.0)	570 (-4.0)	574.05 (+0.05)	573 (-1.0)		

E_1(TO) mode reflect the strength of polar lattice bonds [36]. E_1(TO) mode is also observed when the *c*-axis of the nanostructures become parallel to substrate surface [37]. The presence of E_1(TO) and A_1(LO) modes indicate polycrystalline nature of the nanostructures as observed in XRD analysis. The position of E_2(high) mode shifts due to the presence of stress in the films [38]. It is observed that E_2(high) mode shifts approximately by 1 cm^{-1} in the higher frequency side (compressive stress) for the nanostructures grown at RT and 150^{0}C and by 1 cm^{-1} in the lower frequency side (tensile stress) for the nanostructures grown at 450, 600 and 750^{0}C. But there is no such shift in the nanostructures grown for 300^{0}C which indicates nanostructures are stress free as also observed in XRD analysis

5.4 Conclusions

Highly c-axis oriented ZnO nanostructures with a few flower-shaped nanostructures were synthesized successfully by PLD technique without using any catalyst. FWHM of (002) peak for the nanostructures at 150^{0}C decreased, again increased at 300^{0}C, and then decreased

gradually with the increase in substrate temperature. This variation is attributed to the contribution from large sized grains. FE-SEM images showed that with the increase in substrate temperature, small size particles start to sinter with each other and form larger particles. This transition is observed very well for the nanostructures deposited at RT to 300^0C. Flower-shaped nanostructures were also observed and the density of flower-shaped structures decreased with the increase in substrate temperature. Photoluminescence showed emissions from both from near band-edge as well as defect related states for all the nanostructures. Increase in E_2(low) and E_2(high) Raman mode intensity with increasing substrate temperature indicated better crystallinity. Shifting in E_2(high) mode peak position indicated the presence of stress in the nanostructures except at 300^0C. Intense A_1(LO) mode was present for the nanostructures grown upto 450^0C, then vanished completely at 600^0C and 750^0C. Both PL and Raman spectra indicated that A_1(LO) mode may arise due to the defect related to interstitial zinc. Defect related to interstitial zinc was not observed at elevated substrate temperatures.

Bibliography

1. S. Shao, P. Jia, S. Liu, W. Bai, Material Letters, 62 (2008) 1200.
2. F. Ahmed, S. Kumar, N. Arshi, M. S. Anwar, R. Prakash, Adv. Mat. Lett. 2 (2011) 183.
3. F. Xie, A. Centeno, B. Zou, M. P. Ryan, D. J. Riley, N. M. Alford, J. Colloid. Interface. Sci. 395 (2013) 85.
4. R. Wahab, S. G. Ansari, Y. S. Kim, H. K. Seo, G. S. Kim, G. Khang, H. S. Shin, Mater. Res. Bull. 42 (2007) 1640.
5. S. Kuriakose, N. Bhardwaj, J. Singh, B. Satpati, S. Mohapatra, Beilstein J. Nanotechnol, 4 (2013) 763.

6. WU Shui-Sheng, JIA Qing-Ming, SUN Yan-Lin, JIANG Li-Hong, Wang Ya-Ming, Trans. Nonferrous. Met. Soc. China, 22 (2012) 2465.
7. T Zhang, Y Zeng, H T Fan, L J Wang, R Wang, W Y Fu, H B Yang, J. Phys. D: Appl. Phys, 42 (2009) 045103.
8. S. K. Kansal, A. H. Ali, S. Kapoor, D. W. Bahnemann, Separation and Purification Technology, 80 (2011) 125.
9. M. Liu, X. Q. Wei, Z. G. Zhang, G. Sun, C. S. Chen, C. S. Xue, H. Z. Zhuang, B. Y. Man, Appl. Surf. Sci. 252 (2006) 4321.
10. S. Youssef, P. Combette, J. Podlecki, R. Al Asmar, A. Foucaran, Crystal Growth and Design, 9 (2002) 1088.
11. V. Khranovskyy, R. Yakimova, Physica B 407 (2012) 1533.
12. J. Li, H. Fan, X. Jia, J. Chen, Z. Cao, X. Chen, Journal of Alloys and Compounds, 481 (2009) 735.
13. S. S. Kim, B. T. Lee, Thin solid Films, 446 (2004) 307.
14. C-X. Cun, Z-J. Ping, W-H. Yang, X-P. Shou, P-G. Qiang, Chin. Phys. B, 20 (2011) 096102.
15. V. Gupta, A. Mansingh, J. Appl. Phys. 80 (1996) 1063.
16. T. P. Rao, M. C. Santosh Kumar, S. A. Angayarkanni, M. Ashok, Journal of alloys and compounds, 485 (2009) 413.
17. W. Liu, W. Li, Z. Hu, Z. Tang, X. Tang, J. Appl. Phys. 110 (2011) 013901.
18. A. B. Djuristic, Y. H. Leung, Small, 2 (2006) 944.
19. C. Y. Chen, M. W. Chen, J. J. Ke, C. A. Lin, J. R. D. Retamal, J. H. He, Pure. Appl. Chem. 82 (2010) 2055.
20. S. Chakraborty, P. Kumbhakar, Material Letters 100 (2013) 40.
21. N. R. Panda, B.S. Acharya, P. Nayak, Material Letters 100 (2013) 257.

22. A. B. Djuristic, A. M. C. Ng, X. Y. Chen, Progress in Quantum Electronics 34 (2010) 191.

23. G. Patwari, B. J. Bodo, R. Singha, P. K. Kalita, Research Journal of Chemical Sciences, 3 (2013) 45.

24. M. Willander, O. Nur, J. R. Sadaf, M. I. Qadir, S. Zaman, A. Zainelabdin, N. Bano, I. Hussian, Materials, 3 (2010) 2643.

25. Y. H. Yang, Y. Feng, G. W. Yang, Appl. Phys. A 102 (2011) 319.

26. M. Pudukudy, Z. Yaakob, Superlattices and Microstructures 63 (2013) 47.

27. S. K. Panda, C. Jacob, Appl. Phys. A, 96 (2009) 805.

28. P. Mishra, R. S. Yadav, A. C. Pandey, Struct. Chem. 22 (2011) 1281.

29. S. K. Mishra, R. K. Srivastava, S. G. Prakash, R. S. Yadav, A. C. Pandey, Optoelectronics Review, 18 (2010) 467.

30. F. Guell, J. O. Osso, A. R. Goni, A. Cornet, J. R. Morante, Superlattices and Microstructures, 45 (2009) 271.

31. M. Koyano, P. QuocBao, L. T. ThanhBinh, L. HongHa, N. NgocLong, S.I. Katayama, Phys. Stat.Sol.(a) 193 (2002) 125.

32. X. Zhu, H-Z. Wu, D-J. Qiu, Z. Yuan, G. Jin, J. Kong, W. Shen, Optics Communications 283 (2010) 2695.

33. X. L. Xu, S. P. Lau, J. S. Chen, G. Y. Chen, B. K. Tay, J. Cryst. Growth 223 (2001) 201.

34. G. J. Exarhos, S. K. Sharma, Thin Solid Films, 270 (1995) 27.

35. B. Yang, A. Kumar, P. Feng, R. S. Katiyar, Appl. Phys. Lett. 92 (2008) 233112.

36. N. Ashkenov, B. N. Mbenkum, C. Bundesmann, V. Riiede, M. Lorenz, D. Spemann, E. M. Kaidashev, A. Kasic, M. Schubert, M. Grundmann, G. Wagner, H. Neumann, V. Darakchieva, H. Arwin, B. Monemar, J. Appl. Phys. 93 (2003) 126.

37. R. Zhang, P. G. Yin, N. Wang, L. Gou, Solid State Sci. 11 (2009) 865.

38. S. B. Yahia, L. Znaidi, A. Kanaev, J. P. Petitet, Spectrochimica Acta Part A 71 (2008) 1234.

Chapter 6

Pulsed laser deposited ZnO pores and their characterization

6.1 Introduction

2-Dimensional (2D) ZnO nanostructures have gained research interest because of their diverse shape, large surface area, high surface to volume ratio as compared to thin films. These structures like ZnO nanowall-network [1, 2, 3], nanowall network with honeycomb structures [4] are shown to have potential applications as sensors [3, 5], UV emitters [2, 5, 6], solar cells [2] etc. Another kind of morphology of ZnO such as porous nanostructures [7-9] has shown its applications in solar cell devices. In between these two morphologies, porous thin films composed of nanowalls [10-12] have been synthesized by several deposition techniques as MOCVD [11], chemical soft solution technique [12], PLD [4], vapour phase transport process [5], plasma-assisted molecular beam epitaxy [1], aqueous solution growth method [7] etc. The growth mechanism of ZnO nanowall network [2, 10] is attributed to the anisotropic growth of ZnO nanowires where pyramidal ZnO nuclei formed after capturing by Au nanoparticles coalesce and form nanowall-network structures. Reported pores as well as nanowall-networks structures of ZnO are mostly single crystalline and highly oriented along (002) direction [1, 9, 13]. Polycrystalline nanowall structures with high (002) orientation are also reported [5, 11, 12]. Maeng et. al. have reported the PL emission in UV range of nanowall-network structure at both RT and low temperature [11]. Zein et. al. have reported the PL emission of nanowall-network structure in UV and visible region from the excitonic recombination and defects related emission, respectively [4]. PL emission at 378 nm (UV

range) and visible emission at 550 nm of nanowall structures has been reported by He-Cd laser at 325 nm excitation wavelength [5].

In previous chapters, pressure was kept constant and the effect of change of substarte temperature was considered. Now, keeping deposition time fixed at 45 minutes, ambient pressure was varied from 0.01 to 0.05 mbar. Surface morphology changed drastically within this variation range. At 0.03 mbar, the formation of pores surrounded by craters was observed. Hence, for further investigations, keeping pressure fixed at 0.03 mbar, depositions were carried for different deposition time.

6.2 Experimental details

ZnO nanostructures were deposited on silicon (100) substrates by PLD set-up discussed in Chapter 2 (Section 2.3). These nanostructures were deposited at 600^0C for 45 minutes in presence of O_2 gas pressure of 0.01, 0.03 and 0.05 mbar. Target-substrate distance was fixed at 4 cm and laser fluence was around 12 J/cm^2 under the base pressure of 10^{-5} mbar. Keeping the oxygen pressure fixed at 0.03 mbar, ZnO nanostructures were then deposited for different deposition time duration (5, 15, 30, 45, 60 minutes) keeping other deposition parameters fixed. O_2 was kept at 0.03 mbar pressure as pores surrounded by craters were observed at this pressure. Nanostructures were characterized by XRD (Bruker Advance D8 with Cukα radiation), FE-SEM, AFM and PL spectroscopy.

6.3 Results and discussions

6.3.1 *X-ray diffraction analysis*

The XRD spectra of the synthesized ZnO structures at 0.01, 0.03 and 0.05 mbar oxygen pressures are shown in figure 6.1. The presence of a strong diffraction peak at $2\theta =$

34.55^0 corresponding to the (002) plane of ZnO indicates highly crystalline *c*-axis orientation of the pore structures bounded by craters. Its presence also indicates the wurtzite nature of these structures with the lattice parameters as $a = 3.241A^0$ and $c = 5.187A^0$ [JCPDS No. – 790205, ICSD: 065119]. The peak is slightly more intense at 0.01 mbar O_2 pressure as compared to those deposited at other O_2 pressures.

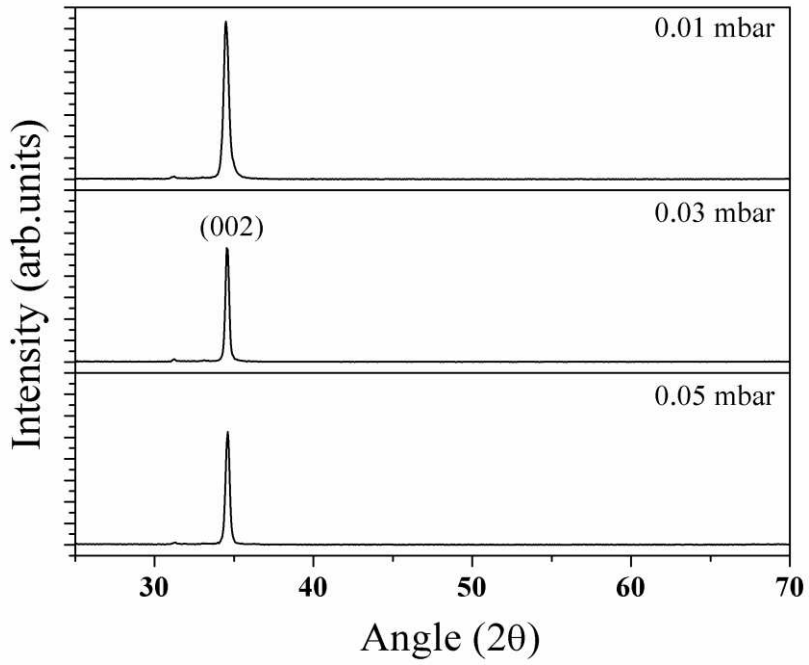

Figure 6.1: XRD spectra of the nanostructures deposited at 0.01, 0.03 and 0.05 mbar O_2 pressures.

Earlier reported porous and nanowall network ZnO structures have shown high crystallinity along (002) direction [1, 9, 13]. The variation of FWHM of (002) peak and the grain size calculated using Debye Scherrer's formula [1] (eqn. 5.1) at different O_2 pressures is given in table 6.1. The FWHM decreases at 0.03 mbar O_2 pressure and then increases again. Since FWHM is a measure of the crystallinity [14] of the structures, the pores deposited at 0.03 mbar are more crystalline. As the pore structures were observed at 0.03 mbar O_2 pressure, further depositions were carried out at various deposition times. The XRD spectra of the nanostructures grown for 5, 15, 30, 45 and 60 minutes are shown in figure 6.2. With

time variation, XRD shows one strong diffraction peak at $2\theta = 34.55^0$ corresponding to the (002) plane of ZnO crystal which reveals that the nanostructures are highly *c*-axis oriented and single crystal in nature.

Table 6.1: FWHM and grain size from XRD of the nanostructures deposited at 0.01, 0.03 and 0.05 mbar O_2 pressures.

Oxygen pressure (mbar)	**0.01**	**0.03**	**0.05**
FWHM (degree)	0.366	0.263	0.298
Grain size (nm)	22.7	31.6	27.9

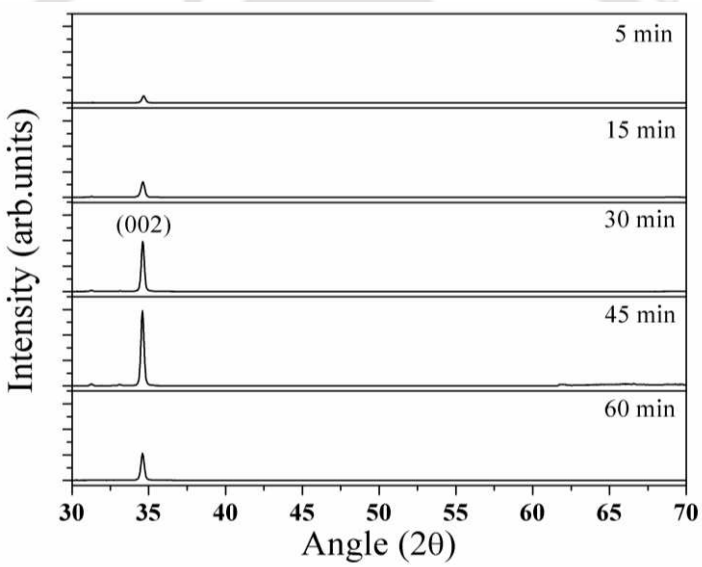

Figure 6.2: XRD spectra of the nanostructures grown for 5, 15, 30, 45 and 60 minutes at 0.03 mbar O_2 pressure.

The FWHM of (002) XRD peak and grain size are given in table 6.2. Table 6.2 shows that the FWHM decreases with the increase in deposition time upto 30 minutes and again increases slightly for 45 minutes and decreases for 60 minutes, indicating that nanostructures typically have better crystallinity at and beyond 30 minutes deposition time. The lower value of FWHM of XRD peak indicates the better crystallinity [14]. Better crystallinity at 30 minutes and 60 minutes nanostructures can be related to the FE-SEM images (section 6.3.1).

The pore size decreased and therefore the density of the pores increased at 30 and 60 minutes deposition time. The growth of the sidewalls of the pores is along *c*-axis which resulted in an increase in the intensity of (002) peak thus enhancing the crystallinity of the nanostructures.

Table 6.2: FWHM and grain size from XRD of the nanostructures grown for 5, 15, 30, 45 and 60 minutes at 0.03 mbar O_2 pressure.

Deposition time (minutes)	**5**	**15**	**30**	**45**	**60**
FWHM (degree)	0.309	0.296	0.233	0.259	0.236
Grain size (nm)	26.97	28.14	35.67	32.2	35.21

The lattice spacing, stress and strain of the nanostructures using eqns. (3.1) and (3.2) were also calculated. The lattice spacing of bulk ZnO is 2.603 A^0 [15, 16]. The nanostructure deposited at 0.01 mbar has lattice spacing close to bulk ZnO, and with the increase in O_2 pressure, there is a slight deviation. Nanostructures deposited for lower deposition time (5, 15 minutes) have lattice spacing at around 2.588 A^0 whereas with the increase in deposition time, value of lattice spacing is close to bulk ZnO. The variation of lattice spacing with oxygen pressure and deposition time is shown in figure 6.3 and figure 6.4, respectively. The deviation in lattice spacing with respect to bulk ZnO indicates the presence of stress and strain in the nanostructures [17].

6.3.2 *Thickness and surface morphology*

The average thickness of the ZnO pore structures was measured by a profilometer and is found to decrease with increase in O_2 pressure (1.13, 1.05, 0.97 μm at 0.01, 0.03, and 0.05 mbar, respectively). Increase in O_2 pressure results in the plasma confinement thereby reducing the flux of the ablated ZnO reaching the substrate and thus giving rise to lesser film thickness. The surface morphology of the ZnO pore structures is shown in figure 6.5.

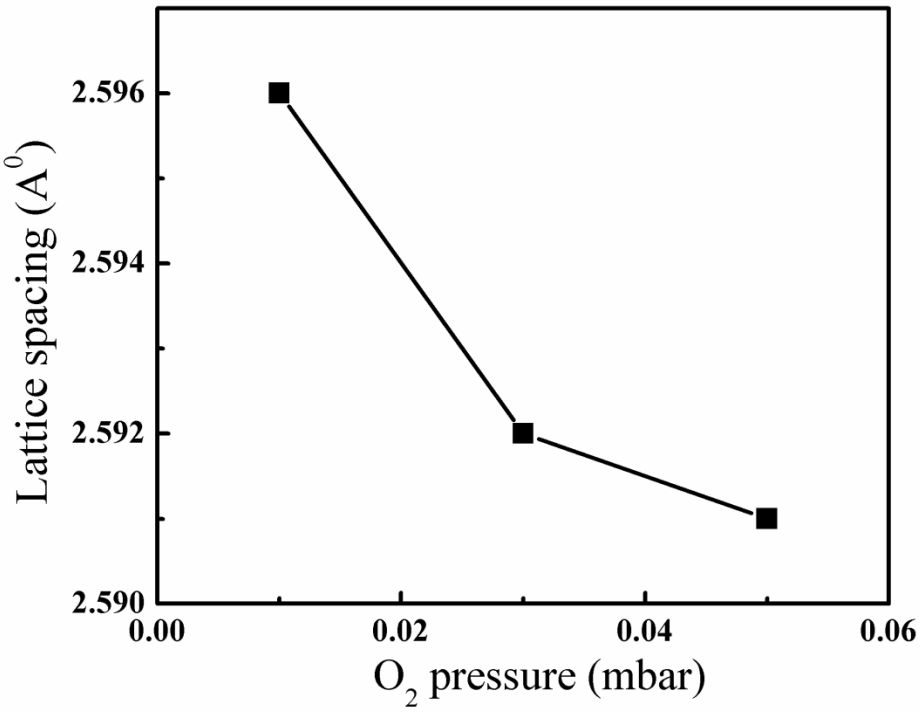

Figure 6.3: Variation of lattice spacing of the nanostructures deposited at 0.01, 0.03 and 0.05 mbar O_2 pressures.

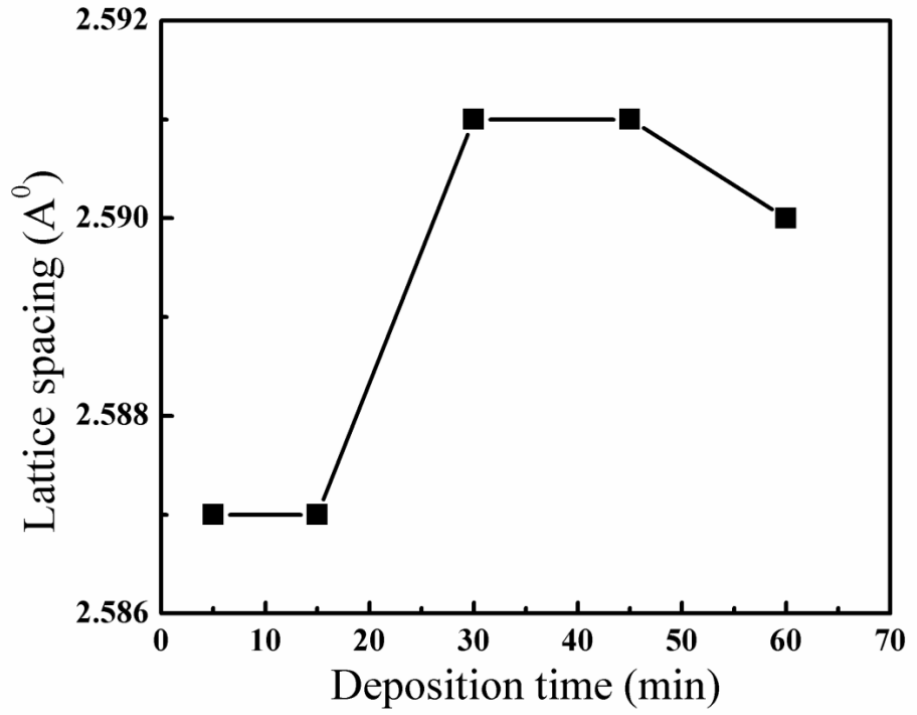

Figure 6.4: Variation of lattice spacing of the nanostructures grown for 5, 15, 30, 45 and 60 minutes at 0.03 mbar O_2 pressure.

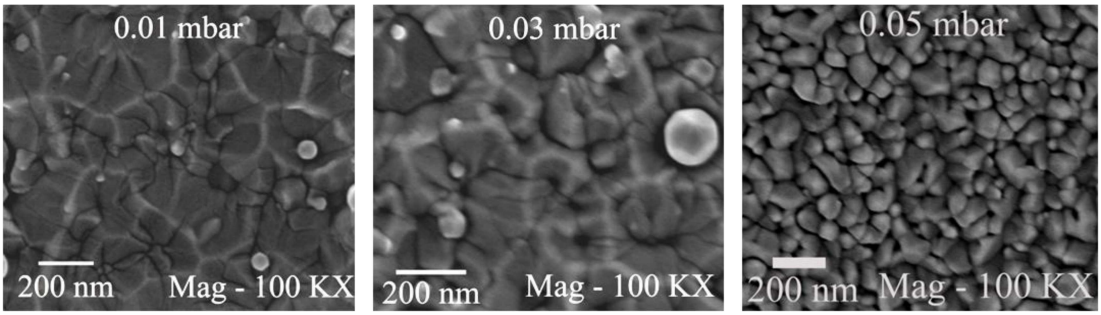

Figure 6.5: FE-SEM images of the nanostructures deposited at 0.01, 0.03 and 0.05 mbar O_2 pressures.

The nanostructures deposited at 0.01 mbar show crater-like structures, however, at 0.03 mbar, pore-like structures (pores) also appears while the sidewalls retained the crater-like structures. With the increase in O_2 pressure, the sidewalls of the pores get thicker and at 0.05 mbar well defined particles are formed. This shows that the formation of pores strongly depends upon the O_2 pressure. Su et. al. [1] have discussed the morphological evolution of nanowalls grown by plasma assisted molecular beam epitaxy with the increase in O_2 pressure and observed that at low O_2 pressure, zinc atoms have enough ability to migrate on the surface and in order to minimize the system energy, adsorbed zinc atoms tend to move to the dislocation reticulation that results in a nanowall-network morphology. Increase in O_2 pressure allows excessive oxygen atoms to decrease the migration of zinc atoms via bonding thereby replacing nanowall-networks by large number of grains.

The thicknesses of the nanostructures increased with deposition time (180, 500, 970, 1051, 1084 nm at 5, 15, 30, 45, and 60 minutes, respectively) due to availability of more particles at higher deposition time. The surface morphology (FE-SEM images) of the nanostructures is shown in figure 6.6. All nanostructures show pore formation and the sidewalls around the pores form crater-like structures. The nanostructures grown for 5, 15, and 45 minutes have well defined crater-like structures along with pores whereas for 30 and 60 minutes, the density of pores is low and the sidewalls are thicker as compared to other nanostructures. The size of the pores, walls and the particles of all nanostructures grown at different deposition

time are listed in table 6.3. The pore size is more for deposition time of 15 and 45 minutes whereas the wall size is less as compared to other nanostructures. Also, the intensity of (002) peak is highly intense for 30 and 60 minutes growth which indicates that *c*-axis orientation of the nanostructures is along the walls.

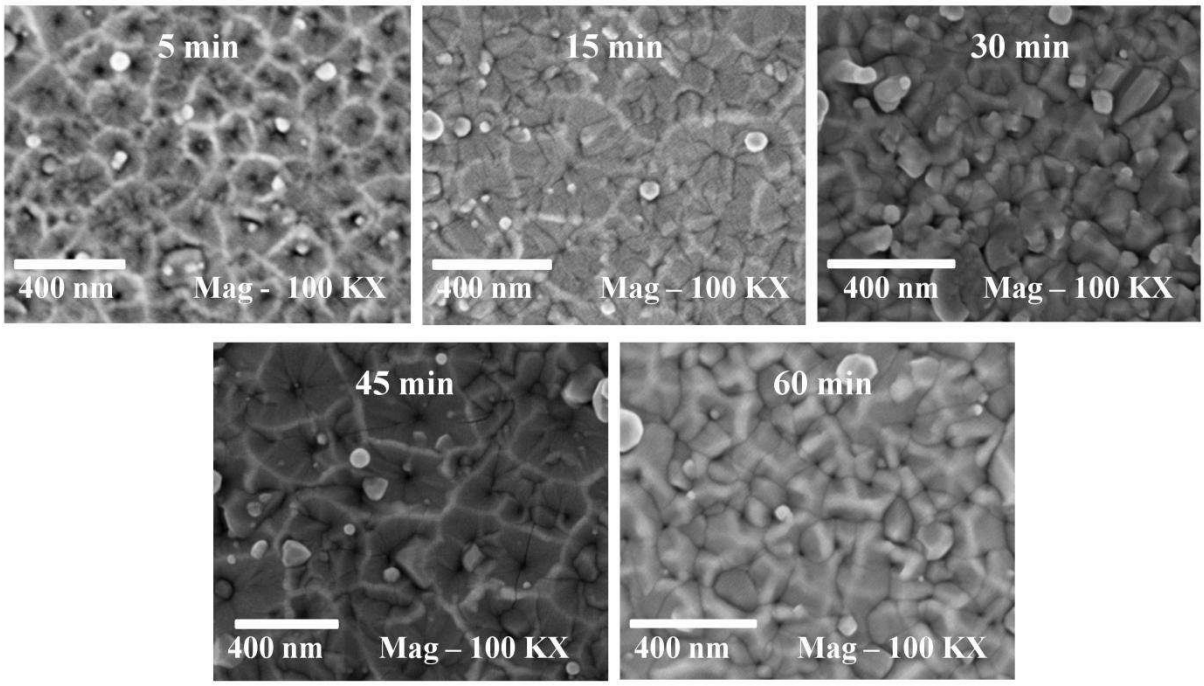

Figure 6.6: FE-SEM images of the nanostructures grown for 5, 15, 30, 45 and 60 minutes at 0.03 mbar O_2 pressure.

Table 6.3: Size of the pores, walls and the particles of the nanostructures grown at different deposition times (from FE-SEM images).

Deposition time (minutes)	Pore size (nm)	Wall width (nm)	Particle size (nm)
5	113.5	17.8	37.1
15	147.9	18.0	26.0
30	132.9	29.4	42.6
45	183.7	19.8	40.5
60	117.4	26.9	34.1

Increase in deposition time allows more and more particles to occupy the surface and hence decreases the pore density. This could be due to the merging of the nearby crater-like structures with each other. This contrast is more visible at 5 and 45 minutes deposition time. However, further increase in deposition time fills up the larger craters thereby again leading to the formation of small craters and reduction in the pore size (60 minutes deposition time).

The mechanism of pore and crater formation can be understood as follows. In PLD, nanostructures are grown by three different growth mechanisms. These are (a) Frank-van-der-Merwe (layer-by-layer growth) (b) Volmer-Weber (island growth) and (c) Stranski-Krastanov (layer-by-layer and island growth). As FE-SEM images show the island growth we attempt to explain pore formation in light of Stranski-Krastanov growth [18]. This growth mechanism occurs when there is a lattice mismatch between the substrate and growth material (i.e., stress present in the material). As we have used Si as a substrate, there is a lattice mismatch (~ 39.1%) between the substrate and ZnO.

First, the role of pressure has to be looked at. At low O_2 pressure (0.01 mbar), collisions between the atomic and ionic species of ZnO and the oxygen atoms is weak so that the kinetic energy of the deposited particles is very high. The high kinetic energy thus scatters the newborn layers [16] and forms the craters surrounded with less wall thickness. As O_2 pressure increases to 0.03 mbar, kinetic energy of the deposited particles decreases and that scatters the newborn layers with lower energy than that at 0.01 mbar. Therefore, the crater size decreases and wall thickness increases as confirmed from FE-SEM images. Further increase in O_2 pressure results in less kinetic energy of deposited particles and hence scattering of newborn layers decreases further in effect decreasing the migration of ZnO. So, the particle-like structures were observed at 0.05 mbar.

To look at the role of deposition time, deposition time evolution of craters bounded by walls has to be looked at and is shown as figure 6.7. Atoms from plasma sit on the substrate

initially layer-by-layer and then forms three dimensional islands. We consider the growth as initially layer-by-layer followed by the formation of three dimensional islands. At 5 minutes deposition, we observed pores formation bounded by craters and the size of the craters is small (figure 6.7a). Particles are energetic hence only these walls of the craters will form as atoms will continue to impinge because of the added energy from the substrate as well. During this process, layer-by-layer growth also continues due to the filling of gaps between 3D-islands. Thus each of the layers gets farther away from the substrate surface. This leads to reduction in the mobility of atoms.

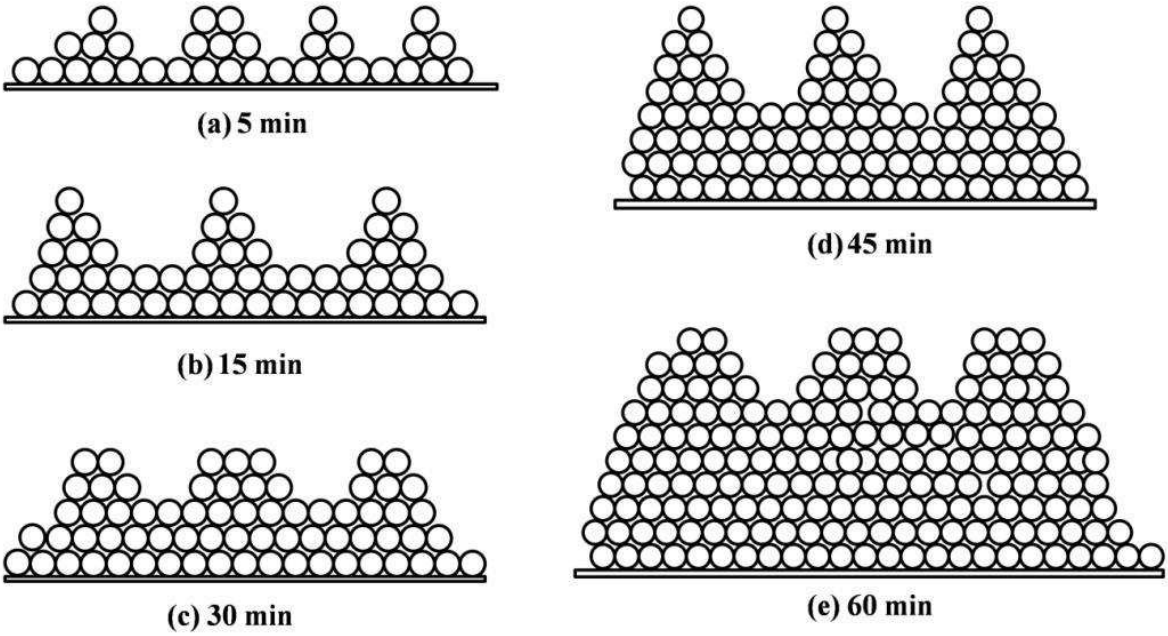

Figure 6.7: Growth mechanism of craters with respect to deposition time.

With the increase in deposition time to 15 minutes, number of particles depositing on the surface increases and forms the 3-D islands on the top of the previous atom layer as shown in figure 6.7(b). With further increase in deposition time, particles occupy the spaces between 3D islands and the size of the craters decreases whereas the width of the wall of the craters increases (figure 6.7(c)-(e)).

6.3.3 *Atomic Force Microscopy*

3-dimensional (3D) AFM images of the nanostructures deposited at 0.01, 0.03 and 0.05 mbar O_2 pressures recorded in non-contact mode are shown in figure 6.8. The roughness of the nanostructures is given in table 6.4. The AFM images show that the roughness decreases with the increase in O_2 pressure which indicates that the pore formation diminishes with the increase in O_2 pressure (as also seen in the FE-SEM images). 3D AFM images of the nanostructures at different deposition time are shown in figure 6.9. The roughness of the nanostructures is given in table 6.5. The AFM images shows that the roughness is very high indicating the porous nature of the surface [19] and is more so for the nanostructures grown for 15, 30 and 45 minutes, respectively.

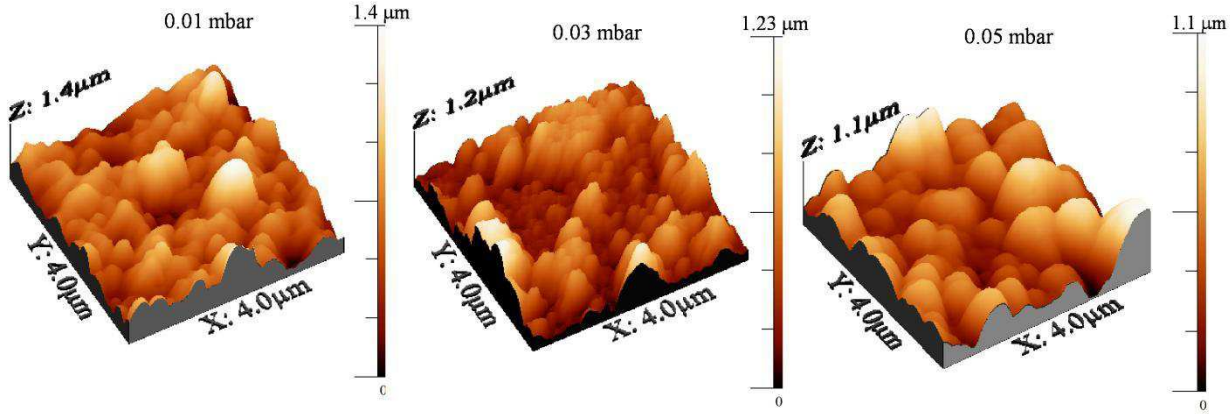

Figure 6.8: 3D AFM images of the nanostructures deposited at 0.01, 0.03 and 0.05 mbar O_2 pressures.

Table 6.4: RMS roughness of the nanostructures deposited at 0.01, 0.03 and 0.05 mbar O_2 pressures.

Oxygen pressures (mbar)	**0.01**	**0.03**	**0.05**
RMS roughness (nm)	206	195	122

2D AFM images of the nanostructures grown at different ambient pressure are also shown in figure 6.10. The line profile corresponds to the green line marked in the images. 2D AFM images of the nanostructures grown at different deposition time are also shown in figure 6.11. Nanostructures deposited for 5 minutes shows that the surface contains small islands. The line profile shows the height difference of around 100 nm and the separation between the islands of same height to be around 10-150 nm. This indicates that the islands form pore-like structures.

In case of 15 minutes growth, surface contains islands of various size and height, as seen from the line profile. The height difference is around 250-350 nm and the separation between the islands is not fixed. So the craters of both the large and small size are observed. Further increase in deposition time to 30 minutes shows that the size of the islands increases which reduces the number of craters.

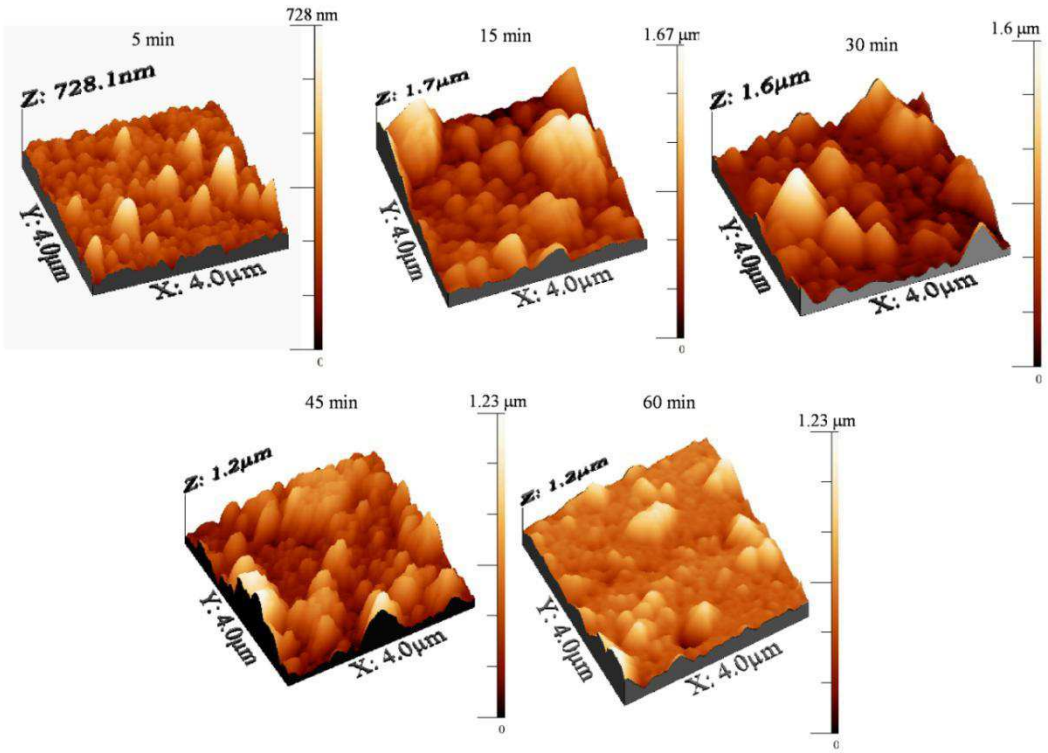

Figure 6.9: 3D AFM images of the nanostructures grown for 5, 15, 30, 45 and 60 minutes at 0.03 mbar O_2 pressure.

Table 6.5: RMS roughness of the nanostructures grown for 5, 15, 30, 45 and 60 minutes at 0.03 mbar O_2 pressure.

Deposition Time (min)	5	15	30	45	60
RMS roughness (nm)	80	270	240	195	134

Line profile shows the height difference of around 200-250 nm and the separation between two islands of same height is less than that of 15 minutes growth. The pore size thus looks small as compared to that for 15 minutes growth. Again, increase in deposition time to 45 minutes, the line profile shows the height difference of around 200-350 nm and the distance between two islands is same height of about 2.5 mm whereas in between there are several pores of around 200-500 nm size. Thus, the analysis shows that the deposition time affects the surface roughness. At larger deposition time, the ambient oxygen gets more time to interact with the ablated species as well as with the particles on the surface.

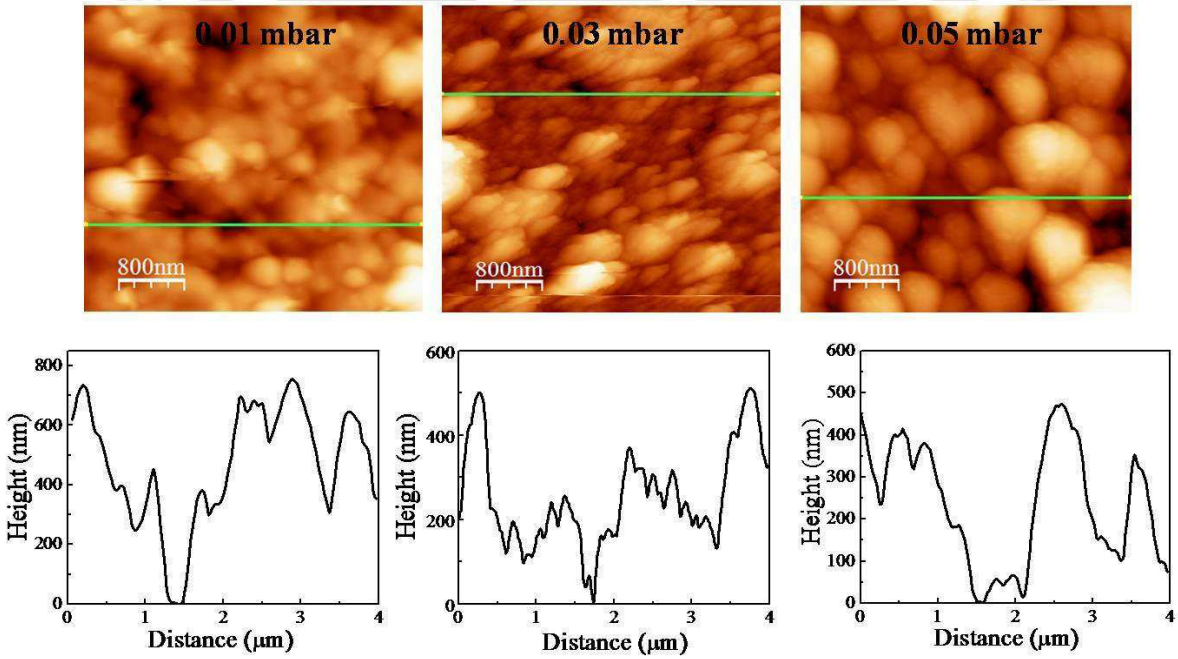

Figure 6.10: 2D AFM images of the nanostructures deposited at 0.01, 0.03 and 0.05 mbar O_2 pressures.

This will allow formation of bigger particles on the surface thus reducing the gaps between the particles.

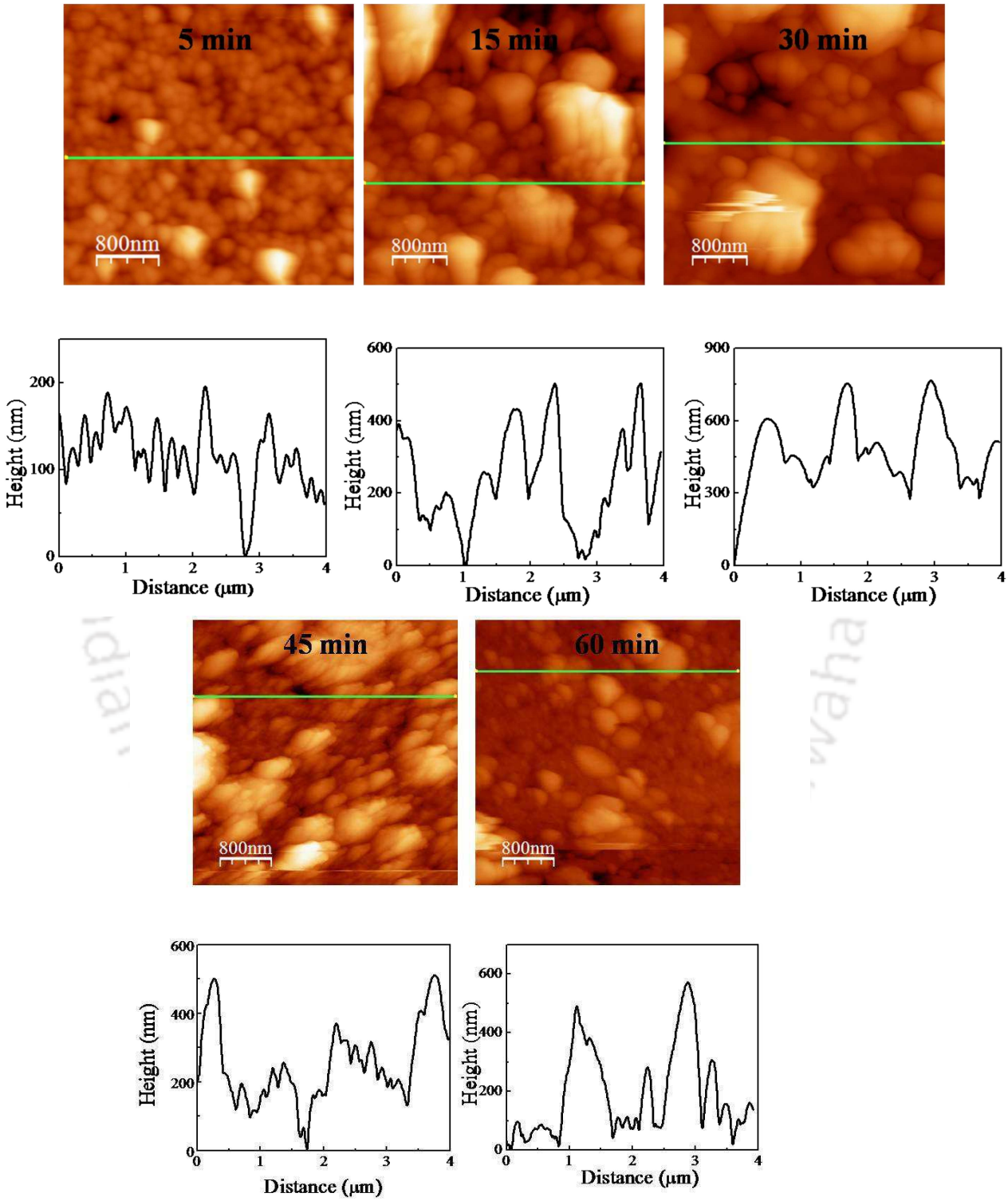

Figure 6.11: 2D AFM images of the nanostructures grown for 5, 15, 30, 45 and 60 minutes at 0.03 mbar O_2 pressure.

6.3.4 *Photoluminescence*

PL spectra of the ZnO pore structures were recorded by using a xenon lamp with 325 nm wavelength as an excitation source. As shown in figure 6.12, the near-band-edge emission is observed at around 393 nm. The less intense excitonic peak is also observed at around 376 nm which is present at 0.03 and 0.05 mbar. Along with that, broad and less intense peak at around 600 nm due to O_2 defects is observed at 0.01 and 0.03 mbar. It is almost absent at 0.05 mbar.

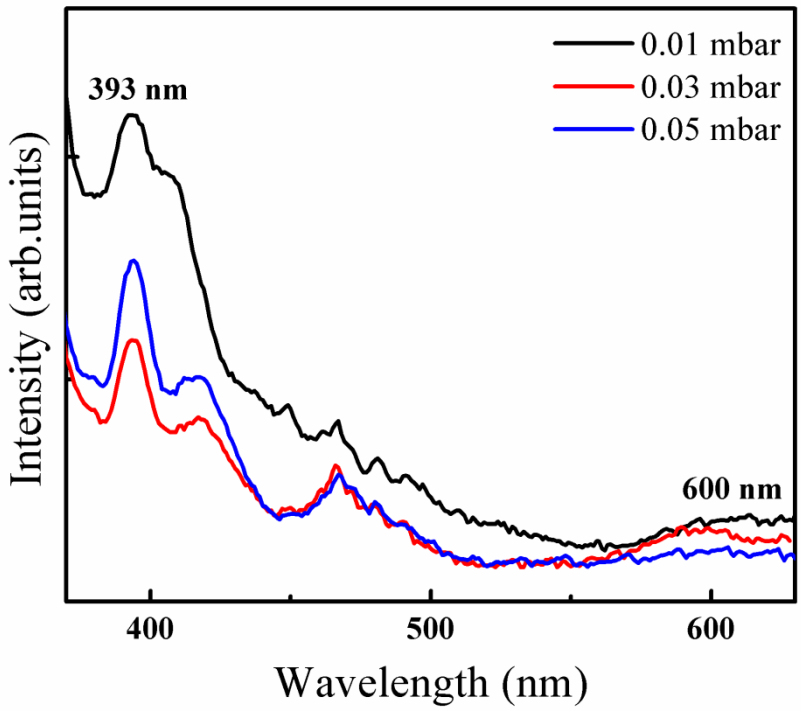

Figure 6.12: PL spectra of the nanostructures deposited at 0.01, 0.03 and 0.05 mbar O_2 pressures.

With the increase in O_2 pressure, more and more oxygen atoms get incorporated in the nanostructures, so the defects due to oxygen vacancy diminish. Gaussian fitted PL peaks are shown in figure 6.13 and listed in table 6.6. Small and broad peak at around 419 nm is observed for the nanostructures grown at 0.03 mbar and 0.05 mbar whereas peak at 411 nm is observed at 0.01 mbar. The peaks at around 410 nm and 420 nm are due to the interstitials defects in ZnO [20 - 22].

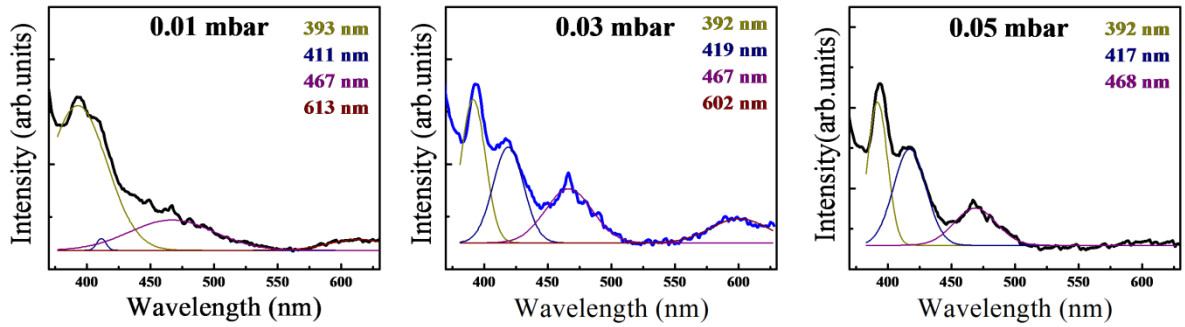

Figure 6.13: Gaussian fitted PL peaks of the nanostructures deposited at 0.01, 0.03 and 0.05 mbar O_2 pressures.

Table 6.6: Gaussian fitted PL peak positions of the nanostructures deposited at 0.01, 0.03 and 0.05 mbar O_2 pressures.

Oxygen pressures (mbar)	PL peak positions (nm)
0.01	393, 411, 467, 613
0.03	393, 420, 468, 602
0.05	392, 417, 468

After Gaussian fitting (figure 6.13) of the PL spectra, the width of the near-band-edge emission is more for the sample grown at 0.01 mbar, and then it decreases at 0.03 mbar and again increases slightly at 0.05 mbar. The width of the near-band-edge emission of PL peak and the FWHM of (002) XRD peak follows the same trend. The decrease in the peak width indicates better crystallinity [23] at 0.03 mbar as compared to that at other pressures and is consistent with the XRD analysis.

PL spectra of the nanostructures at different deposition time are shown in figure 6.14. The nanostructures grown for 5 and 15 minutes have broad near-band-edge emission and with the increase in deposition time, the width of the PL peak of near-band-edge emission decreases gradually. Decrease in width indicates the better crystallinity of the nanostructures [23].

Along with that, low intense excitonic emission and defect related emission at around 420 nm becomes prominent.

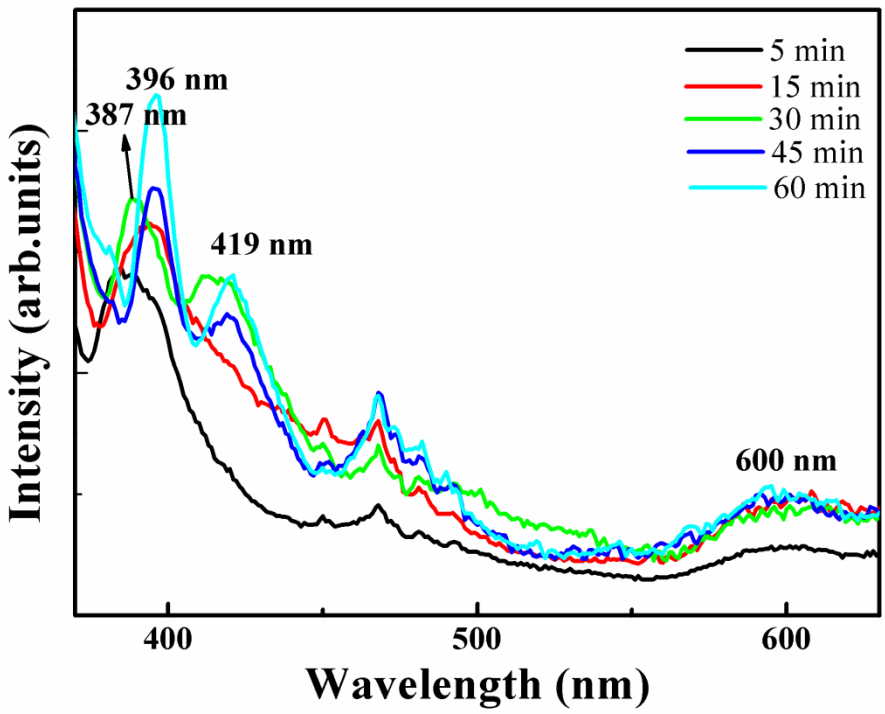

Figure 6.14: PL spectra of the nanostructures grown for 5, 15, 30, 45 and 60 minutes at 0.03 mbar O_2 pressure.

The violet emission centered at 420 nm is due to radiative defects related to interface traps existing at the grain boundaries and emitted from radiative transitions between the trap level and valence band [20]. Also, it is reported that emissions centered at 420 nm are due to interstitial O [19] and at 429 nm is due to interstitial Zn [24]. Patwari et al. have reported that the emission in the range of 414 – 449 nm is due to the emission from interstitial Zn to valence band [22]. All nanostructures have broad peak at around 600 nm (yellow-red emission band) and is attributed to the defects like oxygen vacancies, zinc interstitials etc [25]. The yellow-red emission at 593 nm is due to defect related to zinc vacancy [22]. It is also observed to be dominant for the nanostructures deposited at and beyond 15 minutes

deposition time. Less intense peak at 377 nm is observed for the nanostructures grown for 45 and 60 minutes. The near-band-edge emission is in the range of 387-394 nm. The intensity of near-band-edge emission peak increases with the increase in deposition time. This indicates the crystallinity gets better with the increase in deposition time [26]. The Gaussian fitted peaks of all the nanostructures are shown in figure 6.15 and listed in table 6.7.

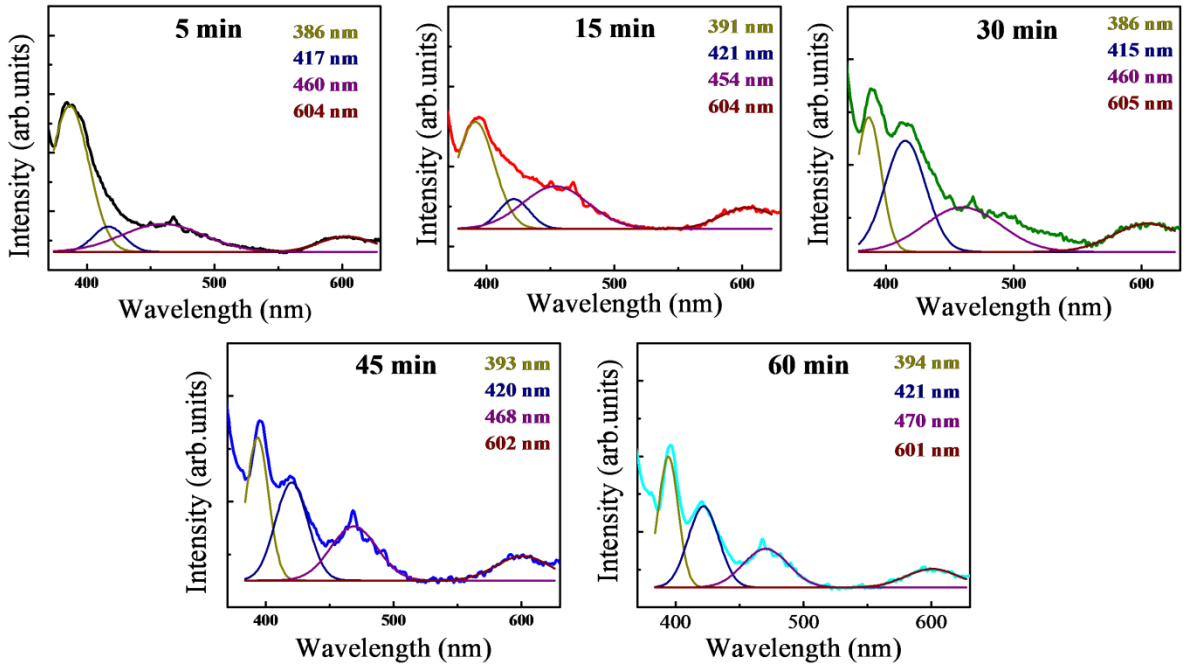

Figure 6.15: Gaussian fitted PL peaks of the nanostructures grown for 5, 15, 30, 45 and 60 minutes at 0.03 mbar O_2 pressure.

Despite near-band-edge emission, the nanostructures deposited for higher deposition time (beyond 15 minutes) shows emissions at a broad range (415 nm – 424 nm). Comparison of the width of the Gaussian fitted near-band-edge PL peaks shows that the width decreases with the increase in deposition time (upto 30 minutes), then increases slightly for 45 minutes and again decreases for 60 minutes (as shown in figure 6.16). This is in agreement with the variation of FWHM of the (002) XRD peak discussed in previous section.

Table 6.7: Gaussian fitted PL peaks of the nanostructures grown for 5, 15, 30, 45 and 60 minutes at 0.03 mbar O_2 pressure.

Deposition time (minutes)	Peak location (nm)
5	386, 417, 460, 604
15	391, 421, 454, 604
30	386, 415, 460, 605
45	393, 421, 468, 602
60	394, 420, 470, 601

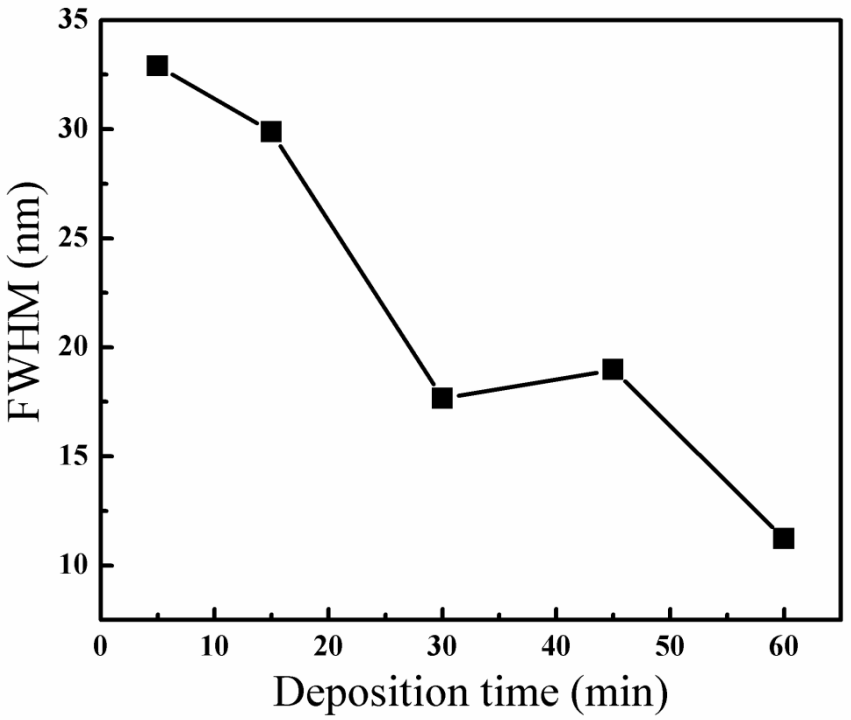

Figure 6.16: FWHM of Gaussian fitted PL near band edge peak of the nanostructures grown for 5, 15, 30, 45 and 60 minutes.

6.4 Conclusions

ZnO pores along with the crater-like structures and nanoparticles were deposited using PLD technique without any catalyst. The XRD data revealed single crystalline structure

along with strong *c*-axis orientation and the contribution is from the walls of the crater-like structures. FE-SEM results showed that with the increase in O_2 pressure, the structures changed abruptly from pores bounded by craters to particles. AFM analysis of the nanostructures showed more roughness and the presence of pores. It is observed that the ambient pressure and deposition time affects the formation of pores, its size and also the density. The pore formation surrounded by craters was discussed in terms of Stranski-Krastanov growth model. PL spectra showed that the pores have less defects at 0.05 mbar. It also showed strong UV emission along with defect related emission at around 420 and 600 nm. The PL width was found to decrease with deposition time indicating better crystallinity of the pore structures.

Bibliography

1. S. C. Su, Y. M. Lu, Z. Z. Zhang, B. H. Li, D. Z. Shen, B. Yao, J. Y. Zhang, D. X. Zhao, X. W. Fan, Physica B, 403 (2008) 2590.
2. M. M. Brewster, M. Y. Lu, S. K. Lim, M. J. Smith, X. Zhou, S. Gradecak, J. Phys. Chem. Lett. 2 (2011) 1940.
3. S. W. Kim, H. K. Park, M. S. Yi, N. M. Park, J. H. Park, S. H. Kim, S. L. Maeng, C. J. Choi, S. E. Moon, Appl. Phys. Lett. 90 (2007) 033107.
4. B. El. Zein, S. Boulfrad, G. E. Jabbour, E. Dogheche, Appl. Surf. Sci. 292 (2014) 598.
5. T. P. Chen, S. P. Chang, F. Y. Hung, S. J. Chang, Z. S. Hu, K. J. Chen, Sensors, 13 (2013) 3941.
6. X. H. Zhang, Y. C. Liu, X. H. Wang, S. J. Chen, G. R. Wang, J. Y. Zhang, Y. M. Lu, D. Z. Shen, X. W. Fan, J. Physics: Condens. Mater. 17 (2005) 3035.
7. Z. Liang, R. Gao, J. L. Lan, O. Wiranwetchayan, Q. Zhang, C. Li, G. Cao, Solar Energy Materials & Solar Cells, 117 (2013) 34.

8. J. X. Wang, C. M. L. Wu, W. S. Cheung, L. B. Luo, Z. B. He, G. D. Yuan, W. J. Zhang, C. S. Lee, S. T. Lee, J. Phys. Chem. C, 114 (2010) 13157.
9. B. Kilic, E. Gur, S. Tuzemen, J. Nanomaterials, 2012, Article ID. 474656.
10. X. Wang, Y. Ding, Z. Li, J. Song, Z. L. Wang, J. Phys. Chem. C. 113 (2009) 1791.
11. J. Maeng, G. Jo, M. Choe, W. Park, M. K. Kwon, S. J. Park, T. Lee, Thin Solid Films, 518 (2009) 865.
12. L. M. Yu, X. H. Fan, J. Y. Shui, L. Cao, W. Yen, Mat. Lett. 68 (2012) 423.
13. C. Li, G. Fang, Q. Fu, F. Su, G. Li, X. Wu, X. Zhao, J. Cryst. Growth, 292 (2006) 19.
14. C-X. Cun, Z-J. Ping, W-H. Yang, X-P. Shou, P-G. Qiang, Chin. Phys. B, 20 (2011) 096102.
15. J. H. Jo, T. B. Hur, J. S. Kwak, D. Y. Kwon, Y. H. Hwang, H. K. Kim, J. Phys. Kor. Soc. 47 (2005) s300.
16. J. Zhao, L. Hu, Z. Wang, J. Sun, Z. Wang, Appl. Surf. Sci. 253 (2006) 841.
17. V. Gupta and A. Mansingh, J. Appl. Phys., 80 (1996) 1063.
18. D. B. Chrisey, G. K. Hubler, Pulsed Laser Deposition of Thin Films, John Wiley & Sons, INC. 1994.
19. C. Nan, G. Fan, J. Fan, F. Li, Material Letters 106 (2013) 5.
20. B. J. Jin, S. Im, S. Y. Lee, Thin Solid Films, 366 (2000) 107.
21. X. L. Xu, S. P. Lau, J. S. Chen, G. Y. Chen, B. K. Tay, J. Cryst. Growth 223 (2001) 201.
22. G. Patwari, B. J. Bodo, R. Singha, P. K. Kalita, Research Journal of Chemical Sciences, 3 (2013) 45.
23. A. Saaedi, M. Cheraghizade, A. G. Aghaji, A. Saedi, J. Basic. Appl. Sci. Res. 3(1s) (2013) 226.
24. P. Mishra, R. S. Yadav, A. C. Pandey, Struct. Chem. 22 (2011) 1281.

25. M. Scepanovic, T. Sreckovic, K. Vojisavljevic, M. M. Ristic, Science of Sintering 38 (2006) 169.

26. G. Kenanakis, M. Androulidaki, E. Koudoumas, C. Savvakis, N. Katsarakis, Superlattices and Microstructures, 42 (2007) 473.

Chapter 7

Two- photon induced photoluminescence and lasing in pulsed laser deposited ZnO nanostructures pumped by CW laser

7.1 Introduction

ZnO is a very good material for optoelectronic devices such as light emitting devices, laser diodes etc. in UV-blue region because of its wide band gap (3.37 eV at RT), as an optical device based on excitonic emissions (such as lasers) because of its high excitonic binding energy (60 meV at RT), and also as a nonlinear device because of its second and third order optical behavior [1]. Simultaneous absorption of two- and more photons at the sub-band gap energy through virtual states is due to the nonlinear interaction of excitation light with the material [2]. The number of photons (n) involved in nonlinear processes can be calculated by using the relation $I = CP^n$, where I is the intensity, C is the constant, P is the power of excitation [3, 4]. Multiphoton induced absorption occurs when the energy corresponding to excitation laser wavelength is less than the half of energy band gap. The PL emission wavelength depends on the excitation wavelength. If the excitation laser with photon energy is less than half of the band gap value, emission occurs at 3.15 eV and is due to bound excitons whereas the incident laser energy is greater than the half of band gap, emission occurs due to free excitons at 3.30 eV [5]. Absorption due to both one- and two-photon is reported for excitation wavelength of 530 nm, and two- and three-photon absorption for excitation wavelength of 800 nm [6]. Anti-stokes PL occurs when the photon energy of incident radiation is less than the energy corresponding to emission wavelength. This PL occurs due to two reasons: one is due to two-step two photon absorption (TS-TPA)

for which a virtual energy level is needed and other is due to Auger process which involves energy transfer between two or more excited electron-hole pairs [7]. As this process requires higher excitation powers, so these PL emissions are considered as nonlinear processes. Lasing emission in ZnO has been observed due to formation of random cavity [8-10], Fabry-Perot (FP) cavity [11, 12] and whispering gallery mode (WGM) [13, 14] cavity. In random lasing, lights get scattered due to the random scatterers present in the system and light gets amplified along the closed loop feedback paths caused by the scattering from the scatterers. In FP cavity mode, lasing comes from single one-dimensional nanostructures where two smooth end-facets act as Fabry-Perot mirrors. In WGM, six boundaries of the hexagonal cavity (as in ZnO) restrict the light waves and light propagates inside the cavity due to multiple total internal reflections from the end facets of hexagonal cavity. Lasing emission due to the formation of both the FP cavity as well as WGM cavity has been observed in a single nanocolumn structure [15]. WGM has been observed mainly in the micrometer order range structures [14, 16]. There are few reports where this mode has been observed in a few nanometer order structures as well [15, 17].

In this chapter, two- photon induced absorption in ZnO nanostructures by using a continuous wave He-Ne laser operated at 632 nm wavelength at the maximum power of around 31.2 mW is reported. These emissions also exhibited modulations that seem to be due to the formation of whispering gallery modes in these structures.

7.2 Experimental details

For studying the two-photon induced PL of bulk as well as nanostructured ZnO, a simple set-up (figure 2.3) has been used. A He-Ne laser (λ = 632 nm) with maximum power of 31.2 mW was used as the excitation source. The laser spot size after focusing the beam was 80 μm. The neutral density filters were placed in front of the nanostructures to vary the

excitation power down to 1.5 mW (a variation in the range of around 1.55×10^2 W cm^{-2} to 7.5 W cm^{-2}). The emission spectra were recorded at various excitation powers to study the number of photons involved in absorption process. The growth and characterization of the nanostructures used in the present study is discussed in chapter 3 and 4.

7.3 Results and discussions

Figure 7.1 shows the emission spectra from ZnO pellet after exciting it with 632 nm continuous wave He- Ne laser. The PL emission is observed at around 355 nm.

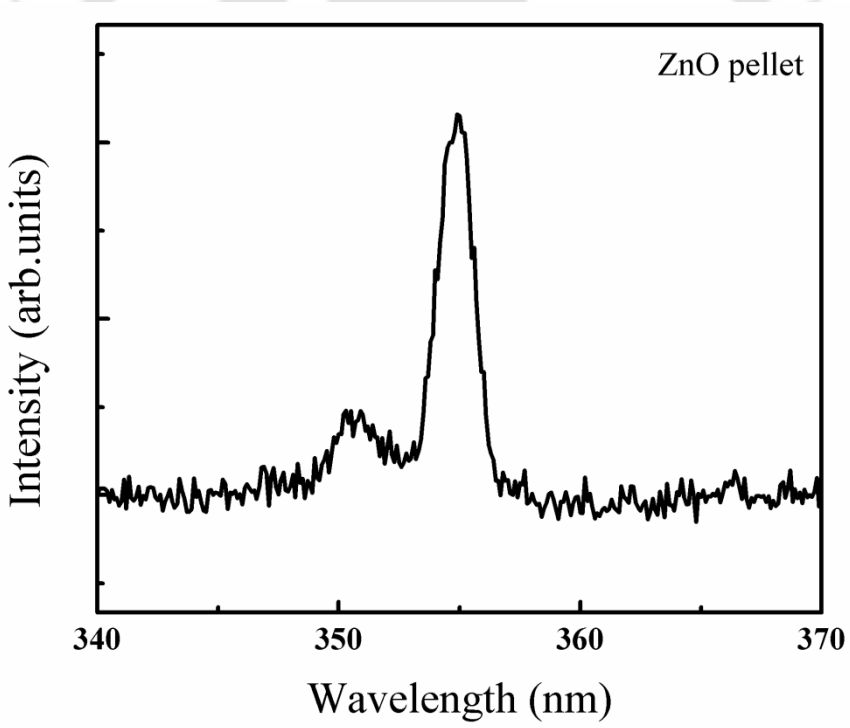

Figure 7.1: PL emission of ZnO pellet.

The emission spectra of the nanostructures grown at 450^0C substrate temperature for 20, 40 and 60 minutes are shown in figure 7.2 (a-c). The corresponding surface morphology of the nanostructures is shown in the inset. The emission of ZnO nanostructures is observed

in the range of 356-365 nm. The emission peak at around 360 nm in ZnO thin films grown on sapphire substrate is reported in the literature at low substrate temperature (100 ^{0}C) and is attributed to the band-band transition due to free electrons [18]. A similar PL emission at 360 nm is also reported and is due to excitonic recombination leading to near band-edge emission [19].

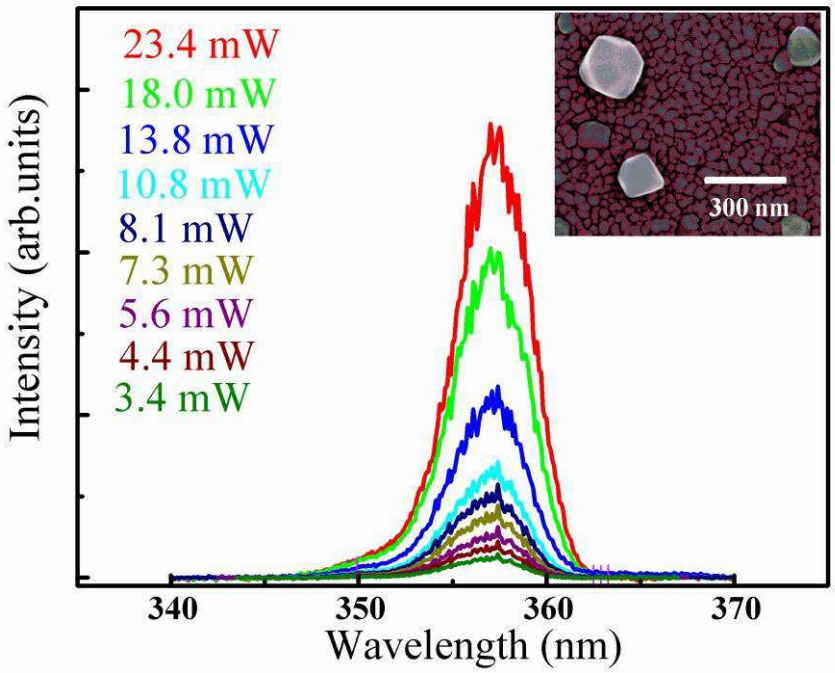

(a) 20 min

ZnO has several defects related to interstitial zinc and oxygen, zinc and oxygen vacancy, antisite oxygen etc as already discussed in the previous chapters. In order to understand the origin of PL emission in the range of 356-365 nm therefore it is important to understand possibilities of the absorption mechanism using CW laser at 632.8 nm wavelength (around 1.96 eV). Consider Figure 7.3 which shows the energy band diagram along with the transitions reported in the literature as well as that observed in the present work against the grown ZnO nanostructures.

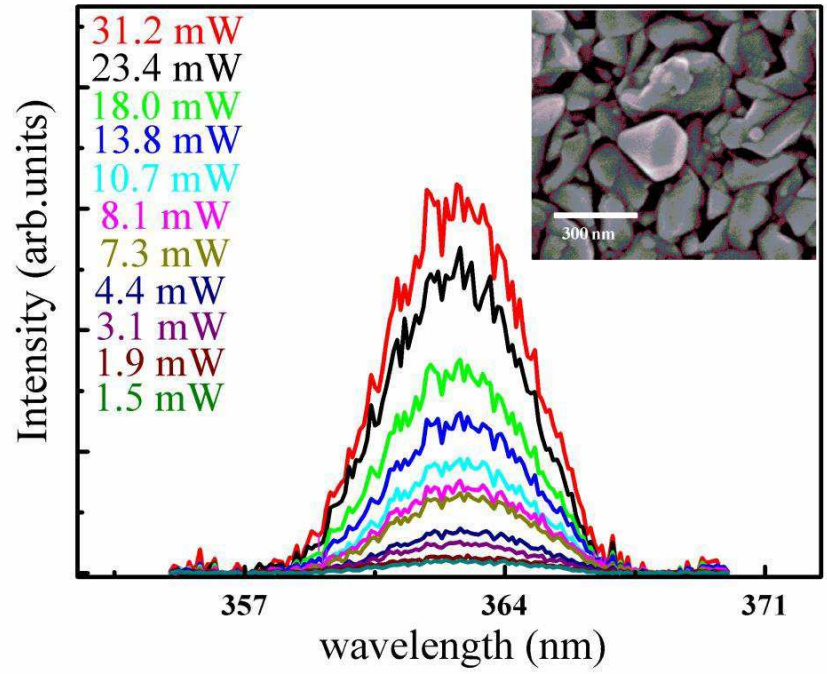

(b) 40 min

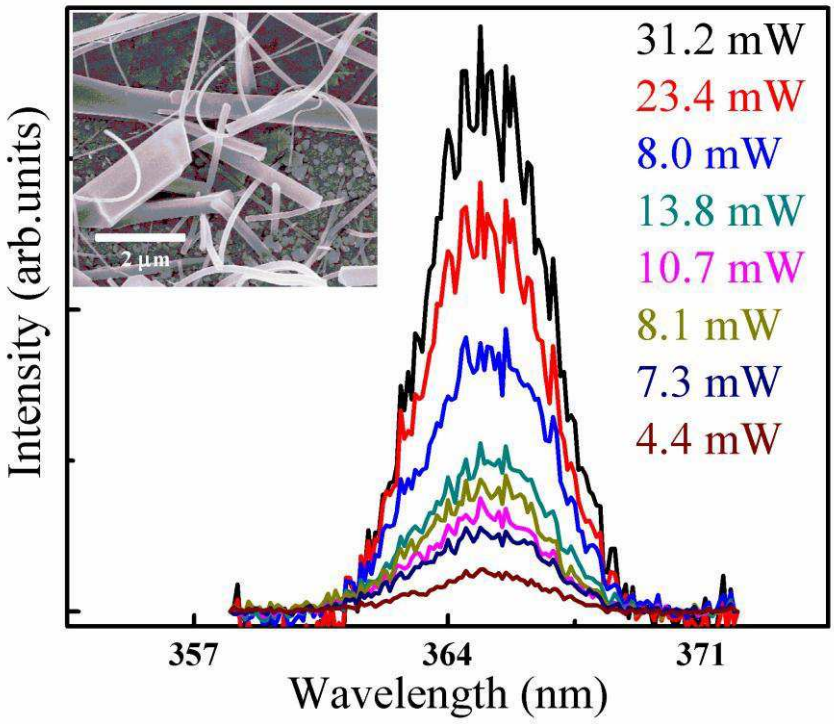

(c) 60 min

Figure 7.2(a-c): Variation of PL intensity with laser power for the nanostructures grown for 20, 40 and 60 minutes at 450^{0}C. The inset shows FE-SEM images of the respective nanostructures.

The emission is possible only if the absorption is via two-photon absorption (TPA). The various possibilities that exist for TPA are: (a) band-to-band transition via virtual state and (b) transition via defect state/interstitial within the band gap which could be due to (i) valence band to the oxygen vacancy and then to the conduction band (CB) , (ii) Zn vacancy to Zn interstitial and then to CB, (iii) oxygen interstitial to Zn interstitial zinc and then to CB, and (iv) antisite oxygen to Zn interstitial and then to CB. The absorption via a virtual state by simultaneous absorption of two photons from valence band to conduction band requires high intensity. In a more recent work, Bharti et al. measured the TPA coefficient for the $Zn_{1-x}Al_xO$ films at around 3.4 cm/W for $x = 0$ using *Z*-scan technique [20]. The excitation source used was a He-Ne laser with the laser intensity of around 1.2 kW cm^{-2}. The reported films have thickness of around a few microns. The laser intensity and the film thickness in the present work are comparable to this reported study and therefore the possibility (a) also cannot be ruled out. Vivas et al. and Zhang et al. have reported studies on the upconversion of PL via TPA [6, 21]. Chen et al. [22] used both pulsed lasers (wavelength in the range of 370 – 450 nm and 710 – 800 nm) and CW diode lasers at 514 and 661 nm with PL measurements at low temperature, ~ 5 K and showed TPA via virtual states as well as via defect states. To initiate the TPA mechanism another possibility is (ii) which is due to the oxygen vacancy (located at 1.62 eV [23] below CB). An electron in the valence band (VB) will absorb a photon of 1.96 eV (this state in the VB is located at around 210 meV below the edge of VB) to reach the oxygen vacancy and from there it will further absorb another photon of 1.96 eV to reach CB. The other possibilities (ii - iv) cannot be ruled out for TPA. A transition from conduction band to these defect states will allow to populate these states which may act as some kind of reservoir. Since the focused region is always in the sea of photons therefore further TPA may occur from these states to CB.

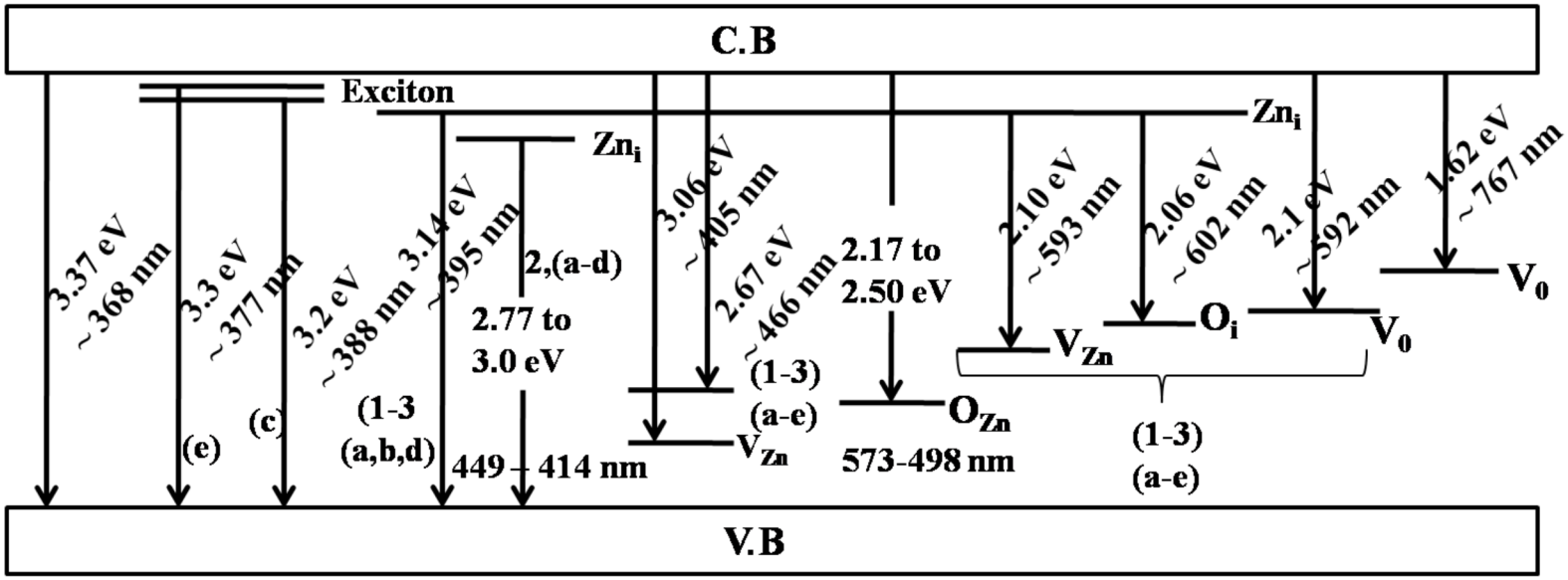

Figure 7.3: Energy band diagram for ZnO. PL emission of nanostructures grown at 450^{0}C substrate temperature for deposition time of (1) 20 minutes, (2) 40 minutes and (3) 60 minutes and for nanostructures deposited for 60 minutes at substrate temperatures (a) RT, (b) 150^{0}C, (c) 300^{0}C, (d) 450^{0}C and (e) 600^{0}C.
[Zn_i – interstitial Zinc, Oi - interstitial Oxygen, V_{Zn} – zinc vacancy, V_O - oxygen vacancy, O_{Zn} – antisite Oxygen]

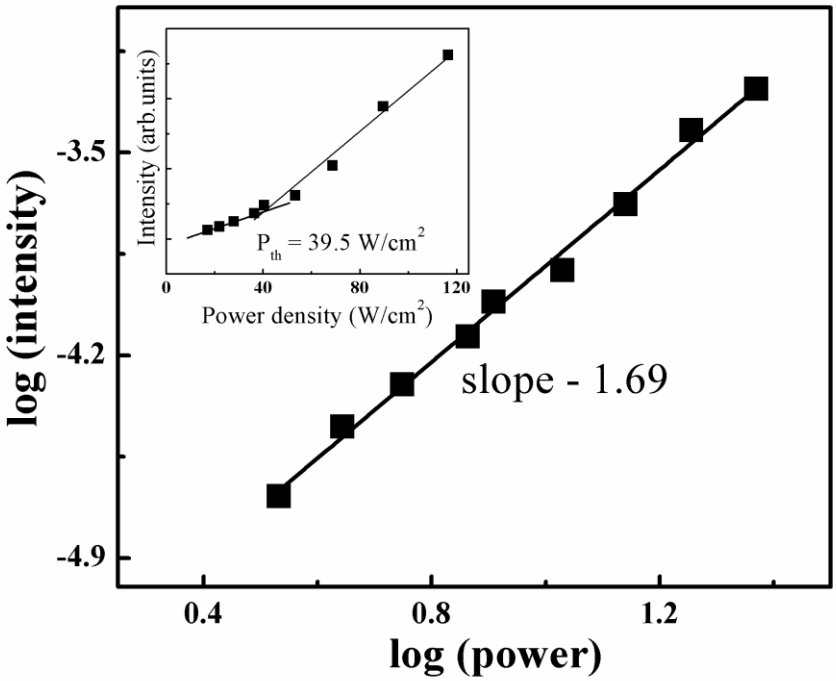

(a) 20 min

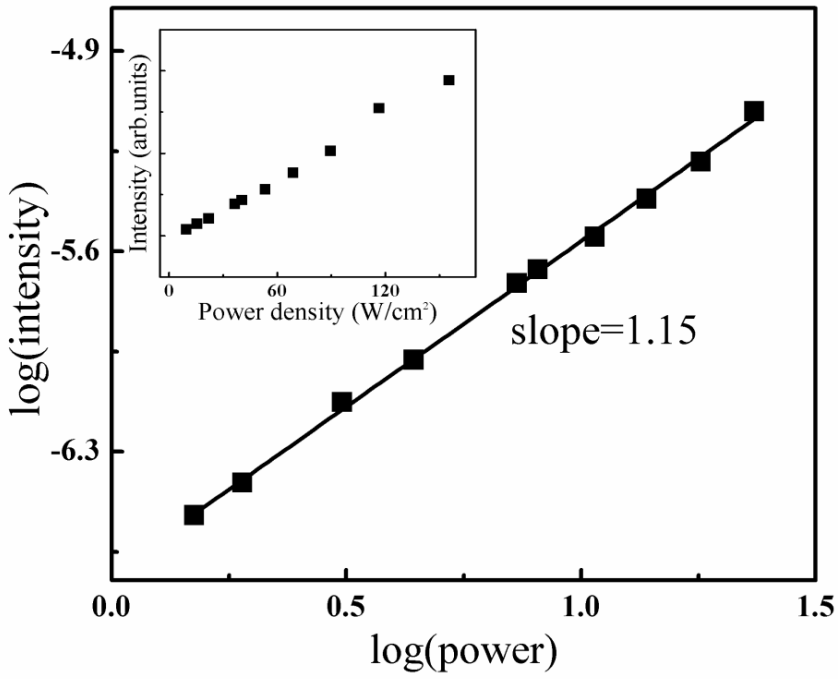

(b) 40 min

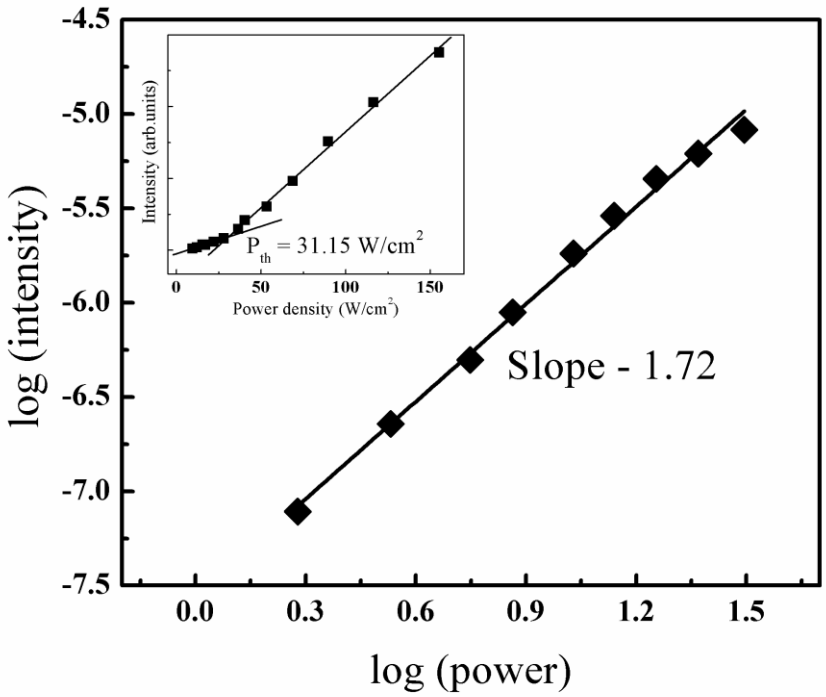

(c) 60 min

Figure 7.4(a-c): Plot of log (intensity) vs. log (power) for the nanostructures grown for 20, 40 and 60 minutes at 450^{0}C. Inset shows variation of peak emission intensity vs. power density for the respective nanostructures.

The PL peak position shift to longer wavelength at 450^{0}C with respect to the deposition time. With the variation in substrate temperature a similar behavior except at 300 ^{0}C where PL peak position shifted towards the shorter wavelength is observed. The relation between emission peak intensity and excitation power [3] is given by $I = CP^n$. The value n = 1 represents 1PA (linear process), n = 2 represents a TPA [3, 6] and n = 3 represents a three photon absorption [6, 24] mechanism. Chen et al. [22] have reported that in 2PA induced emission if the excitation wavelength is in between 400 - 532 nm, power factor becomes 1.3 - 1.6 and absorption occurs via defect states and if excitation wavelength is around or above 661 nm, power factor becomes 2.1 - 2.2 and absorption occurs via virtual states. Figure 7.4(a-c) shows the plot of integrated intensity vs. excitation power on logarithmic scale.

The experimental values of n in the present work are 1.69, 1.15 and 1.72 for UV emission for the nanostructures grown at 20, 40 and 60 minutes, respectively. Experimentally, therefore there is an indication of 2PA for nanostructure grown for 20 and 60 minutes in UV emission range.

For the nanostructures grown for 20, 40 and 60 minutes (inset of figure 7.2), the emission spectra consists of broad emission peak at low power density whereas with the increase in power density, spectra consists of narrow emission peaks (smallest spacing between two successive narrow emission peaks being ~ 0.3 - 0.4 nm) in broad emission background. The narrow emission peaks riding over the broad background grow consistently as the power density of the laser is increased and become more distinct. Gradual increase in the intensity of any of these narrow peaks is not observed and attribute it the low power density of the excitation laser. However, spacing between all narrow peaks is the same and grow gradually indicating as if the spectral structure is due to laser emission. Inset of figure 7.4 (a-c) shows the plot of integrated intensity as a function of excitation power density. The plot shows that the emission intensity increases slowly till a threshold value and beyond it increases rapidly. This behavior can be attributed to the transition from the spontaneous to the stimulated emission. The lasing threshold therefore is 39.5 W/cm^2 and 31.15 W/cm^2 for the nanostructures grown for 20 and 60 minutes, but for 40 minutes, no threshold for lasing action is observed. Lee et al. have reported lasing threshold for ZnO nanorods as 2.6 mJ [25], Dai et al. have reported lasing threshold value of 255 KW/cm^2 for ZnO microrods that formed whispering gallery cavity modes [16], Zalamai et al. have reported lasing threshold value of around 0.3 MW/cm^2 for ZnO nanowires [26], Zhang et al. have reported low threshold lasing with a value of 160 mJ/cm^2 induced by 2PA in ZnO nanowires [27], and Zhang et al. have reported the lasing threshold value of around 55-100 mJ/cm^2 for ZnO

microtubes [11]. These results also indicate that various structures give rise to different lasing thresholds as also observed in our measurements.

Due to hexagonal structure of ZnO, the laser cavity will not have any preferred orientation. Even if the cavity formation is due to scattering from the nanostructures, again the emission can be in any direction. Hence, lasing can occur due to the random scattering from the scatters, formation of FP cavity, or WGM [10, 13, 28].

The Q factor and the mode spacing for the FP cavity is given by the relation $Q = \frac{2\pi\eta L}{\lambda(1-R)}$, where λ is the emission wavelength, η is the refractive index (~ 2.3), and R is the reflectivity at the boundary between the ZnO and air (~ 15.5 %) [29]. As an estimate consider $\delta\lambda \approx 0.15$ nm and at $\lambda = 360$ nm, Q (= $\lambda/\delta\lambda$) [29] is around 2400. Using Q in above relation, calculated $L \approx 50$ μm. Also, using $\Delta\lambda = \lambda^2/2\eta L$ [28], L ≈ 90 μm. However, for the grown diamond-shaped structures, the cavity size could be of the order of ~ 200 nm. The length of the nanorods/nanowires is also ~ 10 μm. Hence the possibility of formation of FP cavity is ruled out.

The possibility that exist for the observation of lasing modes in the recorded spectra could be due to WGM formation. The WGMs have been observed and reported in nanometer sized ZnO nanostructures [17, 30]. In WGM resonator, light circulates due to total internal reflection at the boundary of the resonator and because of this, it leads high Q-factor, high efficiency, low threshold power and low loss [17, 30]. It is observed that the decrease in size (few hundreds of nm range) WGM extends out of the resonator. Thus, it is important to have high crystallinity and as low defect density as possible in such nanostructured materials so as to have high optical gain. Also, it has been reported [17] that quality factor reduces due to the leakage from the resonators as leakage increases with the decrease in the size of resonator. Lasing threshold increases with the decrease in resonator size and beyond a certain dimension

of resonator cavity, lasing doesn't occur [17]. It is reported that WGM lasing has been observed for the resonator size of 491 nm at RT [17].

Figure 7.5 (a-e) shows the recorded PL emission spectra of the nanostructures grown for 60 minutes at RT, 150, 300, 450 and 600^{0}C substrate temperature, respectively. In order to study the number of photons required for up conversion mechanism in the grown nanostructures, the excitation laser power was varied from 31.2 mW to 1.9 mW. The plot of log (intensity) vs. log (power) for the nanostructures grown is shown in figure 7.6(a-e) and the plot of emission intensity as a function of power density is shown in the inset of figure 7.6 (a-e). The value of *n* from these plots is 1.50, 1.75, 1.01, 1.72 and 1.78, respectively. Experimentally, it has been observed that the up-conversion is done by two- photon absorption for the nanostructures grown at RT, 150, 450 and 600^{0}C, Theoretically, the up-conversion of photons occurs due to the absorption of two-photons if the value of E_{photon}/E_{gap} is in between 0.5 to 0.71 [6]. In the present work, the value of E_{photon}/E_{gap} is 0.58. From the inset of figure 7.6 (a-e), it is been observed that the lasing action occurs for the nanostructures grown for RT, 150, 450 and 600 ^{0}C, whereas it is not been observed for the nanostructures grown for 300 ^{0}C. The lasing threshold is nearly at 31 W/cm^2 for RT, 150 and 450 ^{0}C and at 76.8 W/cm^2 for 600 ^{0}C. This can be explained by the surface morphology of the grown nanostructures. For RT, 150 and 450 ^{0}C, both the rods and wires like structures are observed whereas for 300 and 600 ^{0}C, only wires like structures are observed.

It is reported that lasing threshold value increases with the decrease in the dimension of the nanostructures [17]. As the dimension of the nanowires is less than the nanorods, lasing threshold decreases. Though the diameter of nanowires grown at 300^{0}C is more than that of 600^{0}C, no lasing threshold could be obtained at 300^{0}C. This could be due to the presence of interstitial defects at 300^{0}C whereas it is absent for 600^{0}C. Defects results in more scattering and that's why lasing threshold is not observed at 300^{0}C.

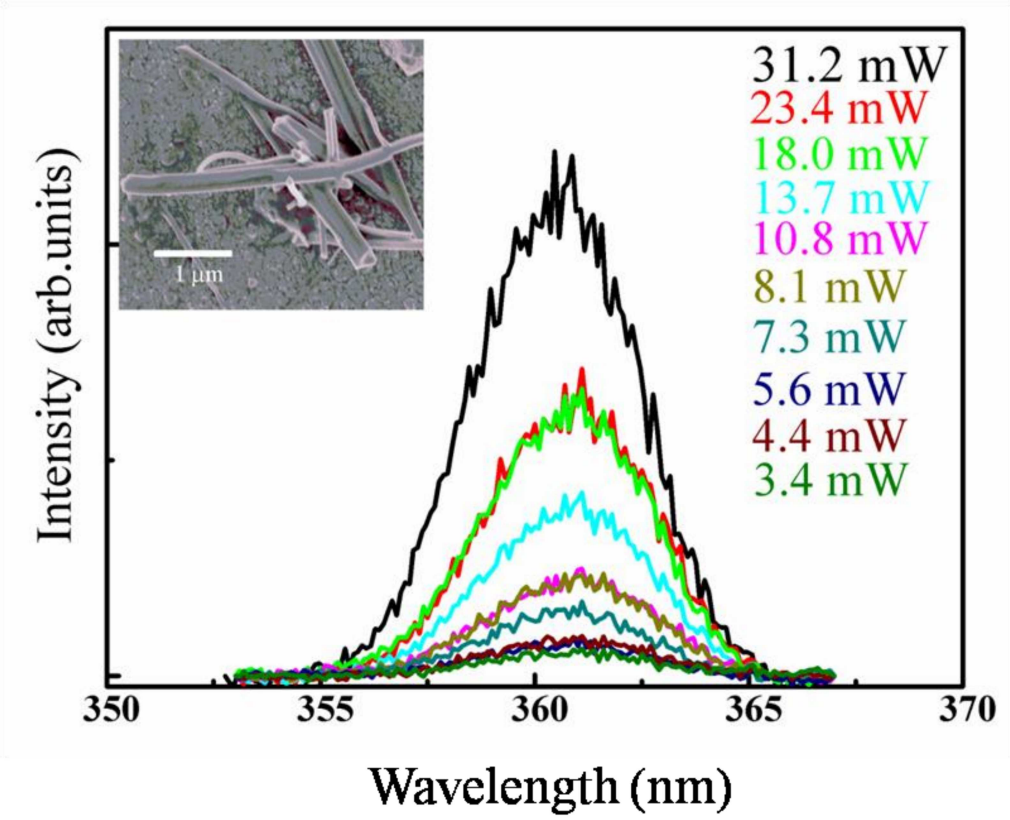

(a) RT

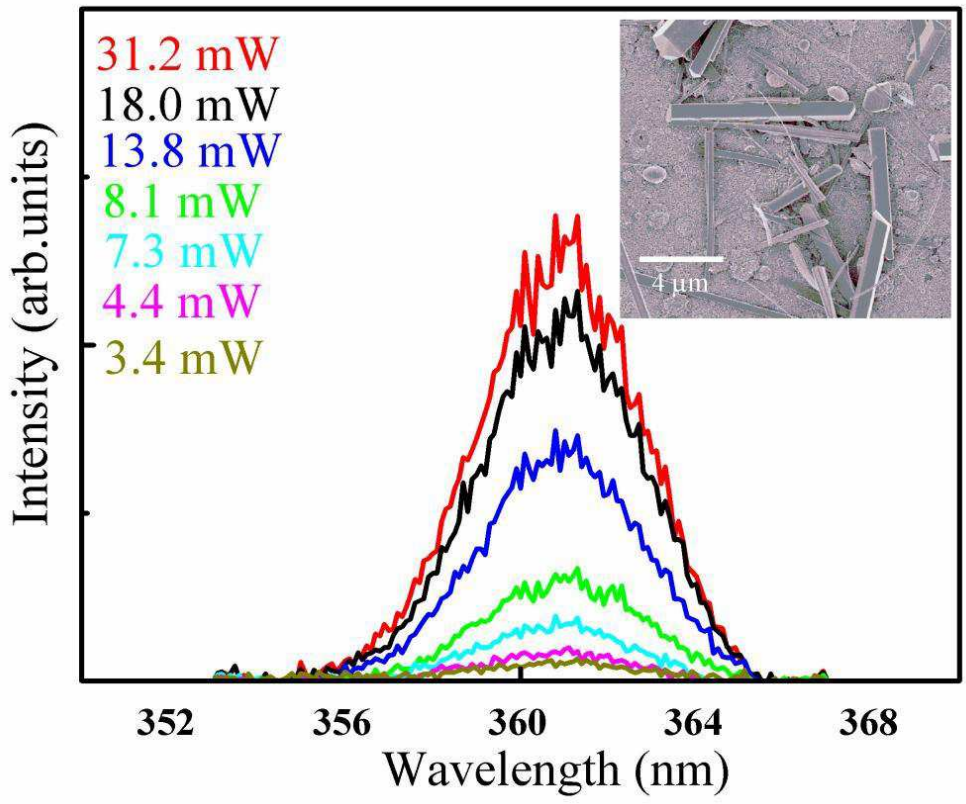

(b) 150^{0}C

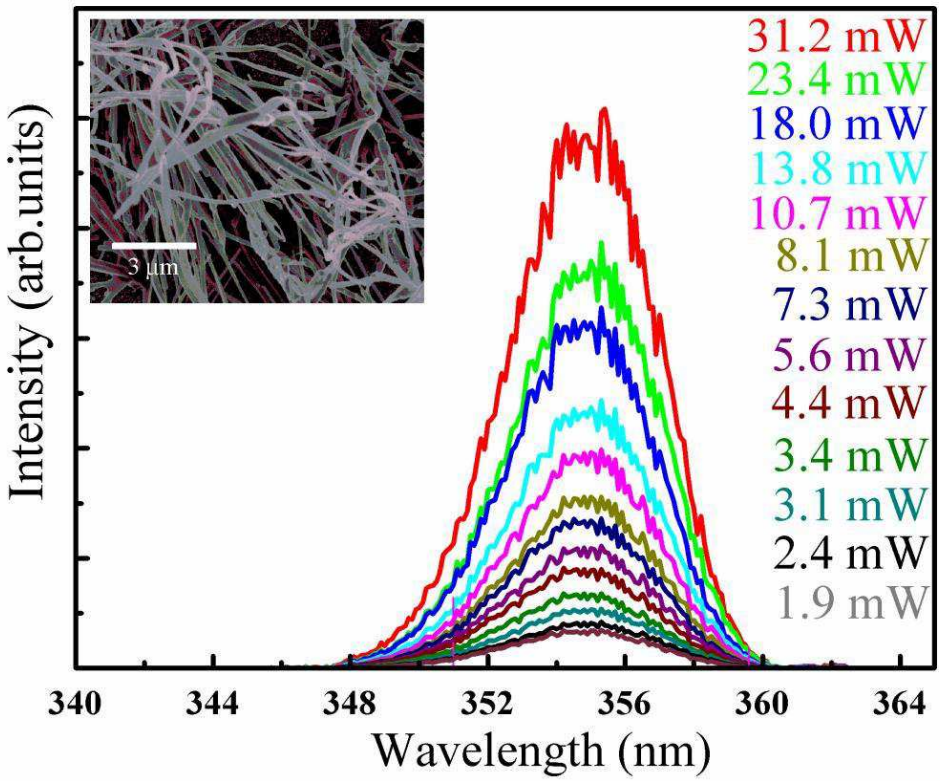

(c) 300^{0}C

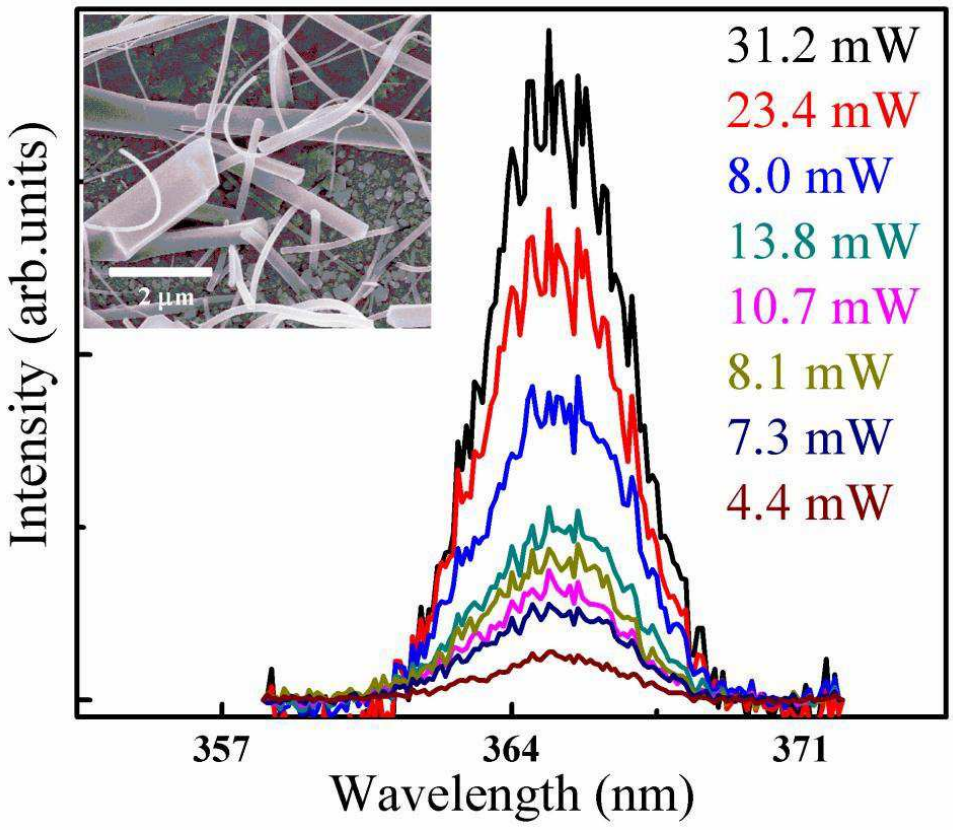

(d) 450^{0}C

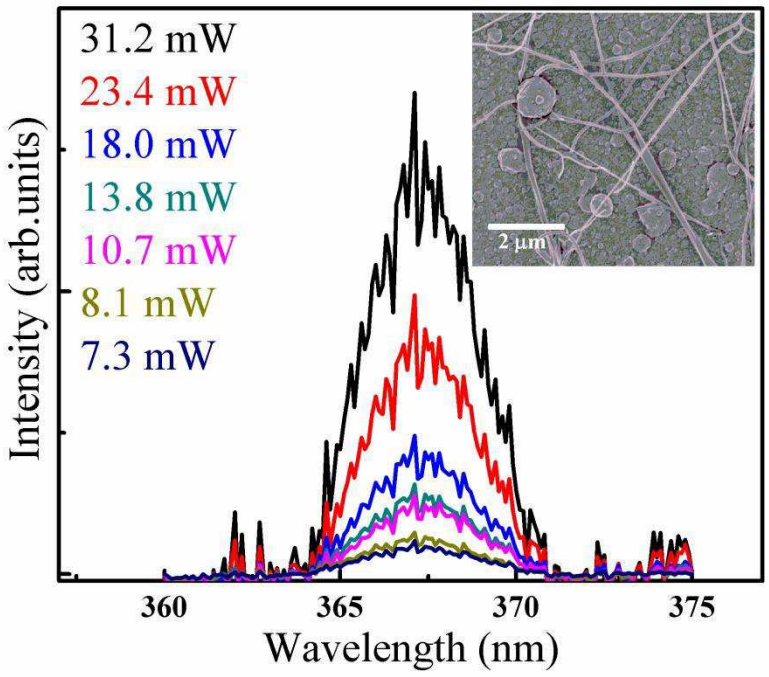

(e) 600^{0}C

Figure 7.5(a-e): Variation of PL intensity with laser power for the nanostructures grown for 60 minutes at RT, 150^{0}C, 300^{0}C, 450^{0}C and 600^{0}C. Inset of the figure shows the surface morphology of the nanostructures.

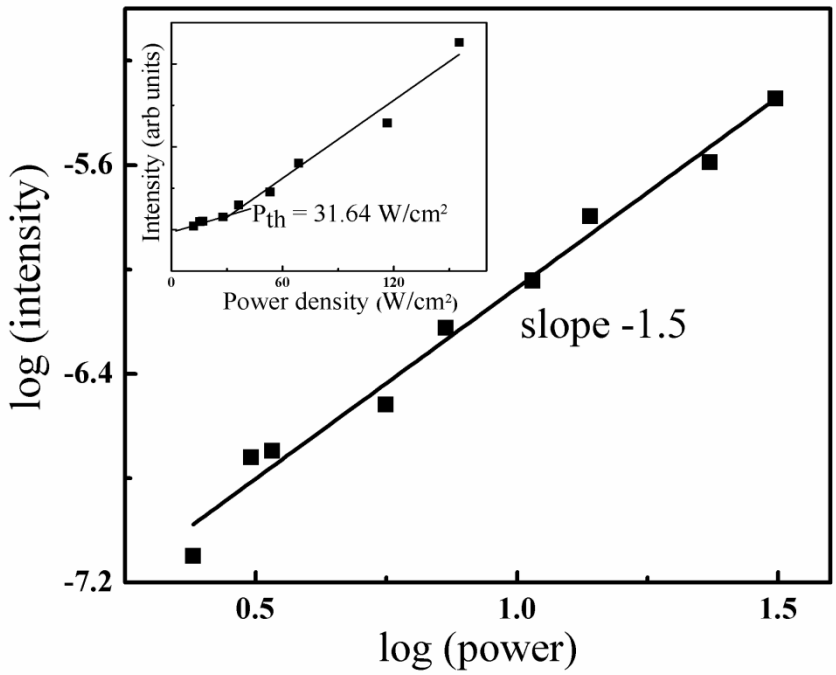

(a) RT

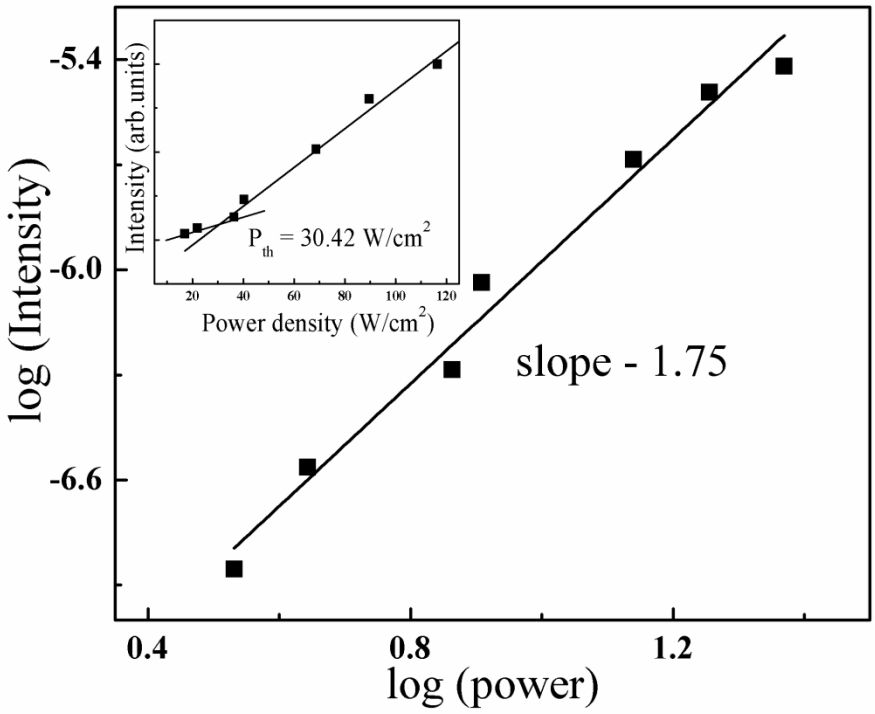

(b) 150^{0}C

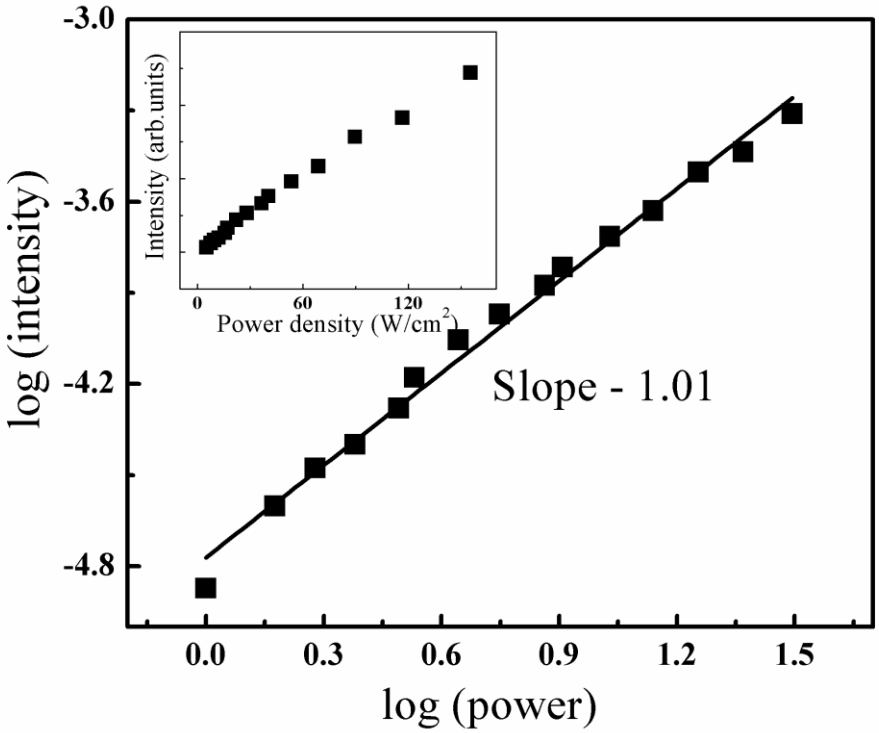

(c) 300^{0}C

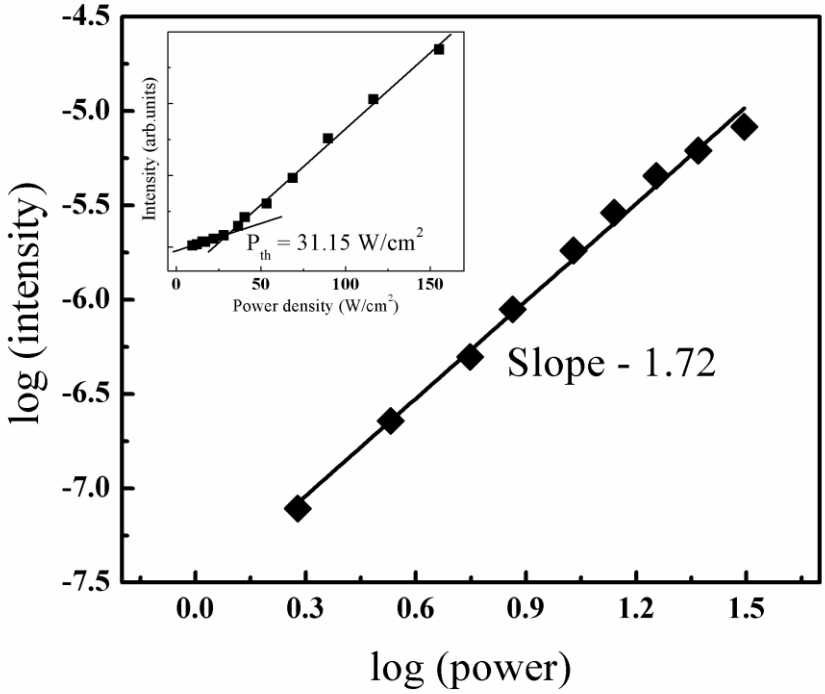

(d) 450^{0}C

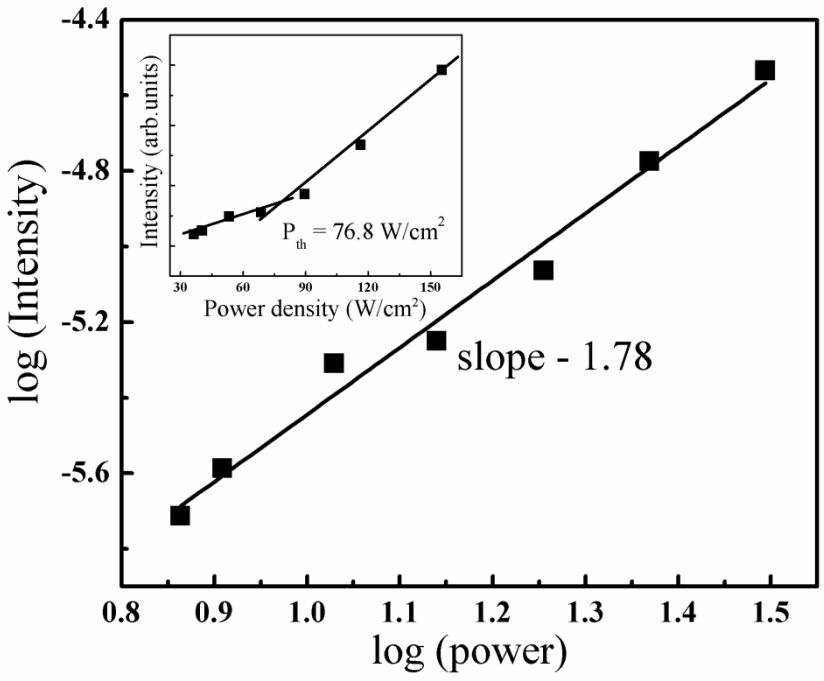

(e) 600^{0}C

Figure 7.6(a-e): Plot of log (intensity) vs. log (power) for the nanostructures grown for 60 minutes at RT, 150^{0}C, 300^{0}C, 450^{0}C and 600^{0}C. Inset shows variation of peak intensity vs. power density for the respective nanostructures.

7.4 Conclusions

Two-photon induced PL emissions and lasing behavior was studied in ZnO nanostructures grown at different substrate temperatures and at different deposition time. Th possibilities explored for two-photon induced PL are attributed to both the transition via virtual level as well as due to the defect states, respectively. These PL emissions also showed lasing behavior seems to be due to the formation of WGM. The lasing thresholds obtained are low and depends upon the morphology of the nanostructures.

Bibliography

1. A. Janotti, Chris G Van de Walle, Reports on progress in Physics 72 (2009) 126501.
2. R. K. Jamal, M. T. Hussein, A. M. Suhail, Journal of Modern Physics 3 (2012) 856.
3. H.S. Shim, N.S. Han, J.H. Seo, S.M. Park, J.K. Song, Bull. Korean Chem. Soc. 31 (2010) 2675.
4. S. K. Das, M. Biswas, D. Byrne, M. Bock, E. McGlynn, M. Breusing, R. Grunwald, J. Appl. Phys. 108 (2010) 043107.
5. P. Xiong, T. Jia, X. Jia, D. Feng, S. Zhang, L. Ding, Z. Sun, J. Qiu, Z. Xu, New Journal of Physics, 13 (2011) 023004.
6. M. G. Vivas, T. Shih, T. Voss, E. Mazur, C.R. Mendonca, Opt. Exp. 18 (2010) 9628.
7. W. Cao, W. Du, F. Su, G. Li, Appl. Phys. Lett. 89 (2006) 031902.
8. H. Cao, Y.G. Zhao, S. T. Ho, E. W. Seelig, Q. H. Wang, R. P. H. Chang, Phys. Rev. Lett. 82 (1999) 2278.
9. S. F. Yu, C. Yuen, S. P. Lau, H. W. Lee, Appl. Phys. Lett. 84 (2004) 3244.
10. R. K. Thareja, A. Mitra, Appl. Phys. B 71 (2000) 181.

11. C. F. Zhang, Z. W. Dong, K. J. Liu, Y. L. Yan, S. X. Qian, H. Deng, Appl. Phys. Lett. 91 (2007) 142109.

12. Z. K. Tang, G. K. L. Wong, P. Yu, M. Kawasaki, A. Ohtomo, H. Koinuma, Y. Segawa, Appl. Phys. Lett. 72 (1998) 3270.

13. D. Yu, Y. Chen, B. Li, X. Chen, M. Zhang, F. Zhao, S. Ren, Appl. Phys. Lett. 91 (2007) 091116.

14. G. P. Zhu, C. X. Xu, J. Zhu, C. G. Lv, Y. P. Cui, Appl. Phys. Lett. 94 (2009) 051106.

15. N. W. Wang, Y. H. Yang, G. W. Yang, Appl. Phys. Lett. 97 (2010) 041917-1.

16. J. Dai, C, X. Xu, K. Zheng, C. G. Lv, Y. P. Cui, Appl. Phys. Lett. 95 (2009) 241110-1.

17. D. J. Gargas, M. C. Moore, A. Ni, S-W. Chang, Z. Zhang, S-L. Chuang, P. Yang, ACS Nano 4 (2010) 3270.

18. G.H. Lee, Y. Tamamoto, M. Kourogi, M. Ohtsu, Thin Solid Films 386 (2001) 117.

19. A. K. Srivastava, M. Deepa, K. N. Sood, E. Erdem, R. A. Eichel, Adv. Mat. Lett. 2 (2011) 142.

20. Proc. National Laser Symposium (NLS-23), S. V. Univrsity, Tirupati, 3-6 December, 2014.

21. C. F. Zhang, Z. W. Dong, G. J. You, S. X. Qian, H. Deng, H. Gao, L. P. Yang, Y. Li, Appl. Phys. Lett. 87 (2005) 051920.

22. S. L. Chen, J. Stehr, N. K. Reddy, C. W. Tu, W. M. Chen, I. A. Buyanova, Appl. Phys. B, 108 (2012) 919.

23. R. Sreeja, Jobina John, P.M. Aneesh, M.K. Jayaraj, Optics Communications 283 (2010) 2908.

24. J. Dai, C.X. Xu, Z.L. Shi, R. Ding, J.Y. Guo, Z.H. Li, B.X. Gu and P.Wu, Opt. Mater. 33 (2011) 288.

25. G. J. Lee, Y. P. Lee, H. H. Lim, M. Cha, S. S. Kim, H. Cheong, S. K. Min, S. H. Han, J. Kor. Phys. Soc. 57 (2010) 1624.

26. V. V. Zalamai, V. V. Ursaki, C. Klingshirn, H. Kalt, G. A. Emelchenko, A. N. Redkin, Appl. Phys. B 97 (2009) 817.

27. C. Zhang, F. Zhang, T. Xia, N. Kumar, J. I. Hahm, J. Liu, Z. L. Wang, J. Xu, Opt. Exp. 17 (2009) 7893.

28. Y. Chen, Y. F. Chen, Opt. Exp. 19 (2011) 8728.

29. M. Ding, D. Zhao, B. Yao, Shulin. E, Z. Guo, L. Zhang, D. Shen, Opt. Exp. 20 (2012) 13657.

30. T. Nobis, E. M. Kaidashev, A. Rahm, M. Lorenz, M. Grundmann, Phys. Rev. Lett. 93 (2004) 103903.

Chapter 8

Conclusions and future scope

In the present thesis, studies on the growth and characterization of various morphologies of ZnO by using PLD technique are reported. ZnO nanostructures of various morphologies, namely, diamond-shaped, combination of nanorods and nanowires, flower-shaped, and pores bounded by craters were deposited on *n*-type Si substrate. ZnO pellets were prepared and sintered to be used as targets for the deposition. A *Q*-switched Nd:YAG laser at a wavelength of 532 nm, repetition rate of 10 Hz and a pulse width of 10 ns was used for creating the ZnO plasma. In order to obtain various morphologies, the substrate temperature was varied in the range of RT to 750 ^{0}C, the ambient pressure of the O_2 gas was varied in the range of 0.01 to 0.1 mbar, and the deposition time was varied in the range of 10 to 60 minutes, respectively. Deposited nanostructures were analyzed by XRD, FE-SEM and AFM, PL and Micro-Raman spectroscopy for studying the crystal structure, surface morphology and roughness, and optical properties, respectively.

In order to deposit the diamond-shaped nanostructures, the deposition time was fixed at 20 minutes whereas the substrate temperature was varied from RT to 600 ^{0}C. It was observed that the nanostructures deposited at RT were almost amorphous in nature. With the increase in substrate temperature nanostructures the intensity of the XRD peak corresponding to (002) plane increased. With the increase in substrate temperature, FWHM of (002) peak decreased indicating better crystallinity at high substrate temperatures. This is because with the increase in substrate temperature, deposited atoms get enough surface mobility to look for a lowest energy sites. But, at 450^{0}C substrate temperature, crystallinity degraded as observed

from XRD as well as with the measurement of FWHM of (002) peak. FE-SEM images of the deposited structures showed the formation of diamond-shaped nanostructures predominantly at 450^0C and a few at 150^0C. The growth of diamond-shaped structure was attributed to the different growth rates of various planes of hexagonal structure. The ratio of the two opposite faces of diamond-shaped structure was calculated to be 3:1 indicating the rate at which the lower and the upper portion of the observed morphology developed. Near band-edge PL emission was intense for the diamond-shaped nanostructures as compared to others and was due to the multiple reflections occurring from the end-facets of diamond-shaped structures. Raman spectra showed the presence of E_2(high) mode which indicated wurtzite nature of the nanostructures. In order to understand the role of deposition time on the growth of diamond-shaped nanostructures, the deposition time was varied at fixed substrate temperature of 450^0C. The analysis of FE-SEM images deposited for different time duration showed that the diamond-shaped structures were more for 20 minutes duration. However, for 60 minute deposition images showed the formation of nanorods/wires.

Since the formation of nanorods/wires was observed for the 60 minutes deposition time, more depositions were done for this duration at all substrate temperatures. Nanostructures deposited at RT were amorphous in nature. Increase in substrate temperature showed the strong (002) peak indicating high crytallinity. Other peaks were also observed but were less intense in nature. The FE-SEM images showed ZnO wire- and rod-like structures at RT, 150 and 450^0C substrate temperatures whereas only wire-like structures at 300 and 600^0C. This growth is attributed to the wide range of size distribution of nanoparticles that acted as the nucleation site for the further growth indicating the importance of the deposition time in the initial growth of these structures. Comparison of the XRD and PL results showed that the nanostructures deposited at 300^0C were crystalline and with less defects indicating better optical properties. Raman analysis confirmed the wurtzite nature of the nanostructures.

Also XRD, PL and Raman analysis, showed that the origin of A_1(LO) mode was due to the presence of interstitial defects in the nanostructures.

Change in deposition time showed that it has an important role in changing the morphology from particles to nanowires/rods/belts. Ambient pressure is also known to affect the morphology of the nanostructures. Studies were now carried out at 0.05 mbar O_2 pressure (reducing from 0.1 mbar) and keeping the deposition time as 60 minutes. Nanostructures deposited were highly crystalline along (002) direction and crystallinity increased with the increase in substrate temperature. Only a slight deviation in crystallinity was noticed at 150^0C. FE-SEM images showed that with the increase in substrate temperature, small size particles started to sinter with each other and formed larger particles (agglomeration). This transformation resulted in the formation of flower-shaped nanostructures. Note that the mean free path of the ablated particles depends on the ambient pressure. When oxygen pressure was changed from 0.1 mbar to 0.05 mbar, the mean free path also changed from 1.3 to 2.7 mm which was very less than the target-substrate distance of 4 cm.

With 45 deposition time, more nanostructures were grown at 0.01, 0.03 and 0.05 mbar ambient oxygen pressure. XRD showed that the nanostructures were single crystalline in nature. FE-SEM images showed that the surface morphology of the nanostructures was very sensitive to O_2 pressure. With the variation of O_2 pressure from 0.01 to 0.05 mbar, nanostructures changed from craters bounded by pores to particles kind of structures. This is attributed to the change in kinetic energy at various pressures resulting in less surface mobility on the substrate. Nanostructures were grown at 5, 15, 30 and 60 minutes at 0.03 mbar O_2 pressure in order to understand the growth evolution of pores bounded by craters. Changing the deposition time also changed the wall thickness which was less at low pressure as compared to that at high pressure. It also resulted in the reduction in the pore density. Reported growth is discussed in accordance with the Stranski-Krastinov growth model.

Nanostructures deposited at different deposition time were found to be single crystal in nature and showed less defects as observed from PL spectra.

The studies carried out above also showed that some of the structures had less defects and stress and strain. It was also mentioned that these nanostructures exhibit better optical properties. In order to confirm these observations, two-photon induced PL studies were carried out on these nanostructures. A continuous wave He-Ne laser at 632 nm wavelength was used for excitation. It was observed that only the nanostructures having less defects showed two-photon induced PL. The PL emission was observed at around 360 nm with modulations. These modulations were well spaced and not random when the excitation power of the laser was changed. This indicated that the emission could be due to the lasing in these nanostructures. Calculations ruled out the possibility of the formation of FP cavity, however, comparison with earlier reported studies showed that the formation of WGM could be one of the possibilities for such modulations. The lasing threshold of the nanostructures also depended on the dimensions of the nanostructures and it increased with the decrease in the dimension of nanostructures.

Future scope

In the present thesis, only a few deposition parameters (substrate temperature, deposition time and O_2 pressure) were varied. These variations indeed showed that the formation was quite sensitive to these parameters. So the thesis was more concentrated on the deposition and characterization of these various nanostructures. The unchanged parameters in the study include laser wavelength, target-substrate distance, and laser fluence. PLD is a versatile technique and involves optimization of various parameters. The formation of particles in the vapor plasma depends on the wavelength. Once the plasma characteristics are fixed by the wavelength, then the role of other parameters can be looked at. Whether similar

structures can be formed at other wavelengths along with the variation in other external parameters needs to be looked at. As pores kind of structures have affinity to adsorb other molecules of either gases or liquids, so some more studies need to be carried out to look at other possible sensor-based applications of these structures. The two-photon induced absorption and lasing were studied using CW laser only. Some more studies can also be carried out using pulsed laser. Simulations will also help in better understanding of the underlying mechanism in the lasing. As defect free nanostructures will only result in higher gain in the nanometer sized structures, the optimization will certainly help in reducing these defects and help in improving the lasing mechanism reported in the present study.

List of Publications

Journals

1. **Poulami Ghosh** and A. K. Sharma, "*Optical Characterization and Growth Mechanism of Combination of Zinc Oxide Nanowires and Nanorods at Various Substrate Temperatures*" **Journal of Nanomaterials**, Vol. 2013 (2013), Article ID. 480164.
2. **Poulami Ghosh** and A. K. Sharma, "*Growth of ZnO nanopores by pulsed laser ablation*", **GSTF Int. J. of Phys. Appl**., Vol. 1, No. 1, pp. 10-13, 2013.
3. **Poulami Ghosh** and A. K. Sharma, "*Growth and optical characterization of diamond-shaped zinc oxide nanostructures deposited by pulsed laser ablation*", **Appl. Phys. A,** Vol. 115, pp. 235-244, 2014.
4. **Poulami Ghosh** and A. K. Sharma, "*Growth and characterization of combination of ZnO nanorods, nanowires on ZnO seed layers by pulsed laser deposition*". **Adv. Sci. Med. Eng.** Vol. 6, No. 4, pp. 393-398, 2014.
5. **Poulami Ghosh** and A. K. Sharma, "*Effect of substrate temperature on the growth of pulsed laser deposited ZnO nanostructures*". **Appl. Phys. A,** Vol. 116, pp. 1877-1884, 2014.
6.
7. **Poulami Ghosh** and A. K. Sharma, "*Structural and optical characterization of pulsed laser deposited ZnO pores surrounded by ZnO-walled craters*" (Communicated)
8. **Poulami Ghosh** and A. K. Sharma, "*One- and two- photon induced photoluminescence and lasing in pulsed laser deposited ZnO nanostructures pumped by continuous wave laser*" (Communicated).

Proceedings

1. **Poulami Ghosh** and A.K. Sharma, *Effect of deposition Time on the Growth of Diamond-like Zinc Oxide Nanostructures*, **AIP Conf. Proc.** 1536, 95-96 (2013).
2. **Poulami Ghosh** and A.K. Sharma, *Spectroscopic Study of Laser Induced ZnO Plasma at 1 mbar Oxygen Pressure*, **AIP Conf. Proc.** 1536, 1195-1196 (2013).
3. **Poulami Ghosh** and A. K. Sharma, *Effect of Substrate Temperature on the pulsed laser deposited ZnO nanostructures*, **E-proceedings:** ISBN 978-81-903321-3-2 (2013).

Conferences attended

1. **Poulami Ghosh** and A. K. Sharma, *Growth of diamond-like zinc oxide nanostructures by pulsed laser ablation*, 2nd International Conference on Advanced Nanomaterials & Nanotechnology (**ICANN-2011**), IIT Guwahati, December 8-10, (2011).
2. **Poulami Ghosh**, A. K. Sharma and Alika Khare, *Two-photon absorption induced photoluminescence in diamond-like zinc oxide nanostructures*, 1st International OSA Network of Students Conference (**IONS-1**), IIT Delhi, December 1-2, (2011).
3. **Poulami Ghosh** and A. K. Sharma, *Growth of ZnO nanorods/wires on ZnO seed layers by pulsed laser deposition*, Twenty-first International Symposium on Processing And Fabrication of Advanced Materials (**PFAM XXI**), IIT Guwahati, December 10-13, (2012).
4. **Poulami Ghosh** and A. K. Sharma, *Two-photon induced photoluminescence from zinc oxide nanostructures pumped by continuous wave He-Ne laser,* **XXXVII National Symposium of Optical Society of India**, Pondicherry University, January 23-25, (2013).
5. **Poulami Ghosh** and A. K. Sharma, *Effect of Deposition Time on the Growth of Diamond-like Zinc Oxide Nanostructures,* International Conference on Recent Trends in Applied Physics and Material Science (**RAM 2013**), Govt. College of Engineering and Technology, Bikaner, February 01-02, (2013).
6. **Poulami Ghosh** and A. K. Sharma, *Spectroscopic Study of laser induced ZnO Plasma,* International Conference on Recent Trends in Applied Physics and Material Science (**RAM 2013**), Govt. College of Engineering and Technology, Bikaner, February 01-02, (2013).
7. **Poulami Ghosh** and A. K. Sharma, *Effect of Substrate Temperature on the pulsed laser deposited ZnO nanostructures,* **DAE-BRNS National Laser Symposium**, BARC, Mumbai, February 06-09, (2013).
8. **Poulami Ghosh** and A. K. Sharma, *Growth of ZnO Nanostructures in Ambient Oxygen*, 6th **India-Singapore Joint Symposium On Physics Of Advanced Materials**, IIT Kharagpur, February 25-27, 2013.
9. **Poulami Ghosh** and A. K. Sharma, *Effect of Oxygen Pressure on the Growth of ZnO Nanopores*, 7th International Conference on Materials for Advanced Technologies (**ICMAT 2013**), Singapore, June
10. **Poulami Ghosh** and A. K. Sharma, *Effect of Deposition Time on Pulsed Laser Deposited ZnO Nanopores*, International Conference on Nanotechnology (**ICNT 2013**), October 25 -26, (2013).
11. **Poulami Ghosh** and A. K. Sharma, *Growth and characterization of Zinc Oxide nanostructures on ZnO seed layer at two different Oxygen pressures,* (**AMAN 2014**), May 17-19, (2014).

Schools attended

1. DST Sponsored *"SERC Preparatory School on Modern Optics"* held at IIT Guwahati during November 10 - November 23, 2010.
2. Winter School on *"Recent Trends in Physics of Atoms, Molecules and Lasers"* held at Banaras Hindu University during January 09 - January 31, 2011.